

Universität Stuttgart



Max-Planck-Institut für Festkörperforschung

Physikalische Festkörperchemie



Von der Fakultät Chemie der Universität Stuttgart zur Erlangung der Würde eines
Doktors der Naturwissenschaften (Dr. rer. nat.) genehmigte Abhandlung

**Selective ion transport
through ion exchange membranes –
effects of chemical interactions and morphology**

Hauptberichter:

Prof. Dr. Joachim MAIER

Mitberichter:

Prof. Dr. Frank GIEßELMANN

Prüfungsvorsitzende:

Prof. Dr. Sabine LUDWIGS

Vorgelegt von:

Andreas MÜNCHINGER

aus Stuttgart

Einreichung: 12.04.2021

Prüfung: 18.05.2021

daily supervision by

Dr. habil. Klaus-Dieter KREUER

Declaration of authorship

The work described in this thesis entitled *Selective ion transport through ion exchange membranes - effects of chemical interactions and morphology* was carried out by the author in the department of Prof. Maier at the Max Planck Institute for Solid State Research from February 2016 to April 2021. The contents are the original work of the author except where otherwise indicated. Passages may show similarities to the following publications:

- Andreas Münchinger and Klaus-Dieter Kreuer. Selective ion transport through hydrated cation and anion exchange membranes I. The effect of specific interactions. *Journal of Membrane Science*, 592: 117372, 2019.
- Andreas Münchinger, Tongshuai Wang, Torben Saatkamp, Giorgi Titvinidze, Alain Farchi, Sangil Kim and Klaus-Dieter Kreuer. Selective ion transport through hydrated cation and anion exchange membranes II. The effect of morphology. *Journal of Membrane Science*, in preparation.
- Klaus-Dieter Kreuer and Andreas Münchinger. Fast and Selective Ionic Transport: From Ion Conducting Channels to Ion Exchange Membranes for Flow Batteries. *Annual Reviews of Materials Research*, 51(1):21-46, 2021.
- Tongshuai Wang, Junyoung Han, Kihyun Kim, Andreas Münchinger, Yuechen Gao, Alain Farchi, Yoong-Kee Choe, Klaus-Dieter Kreuer, Chulsung Bae and Sangil Kim. Suppressing vanadium crossover using sulfonated aromatic ion exchange membranes for high performance flow batteries. *Materials Advances*, 2020.

Stuttgart, 12th April 2021

Andreas Münchinger

Acknowledgement

This work would not have been possible without the support and assistance of many people.

I would first like to thank Prof. Maier for giving me the opportunity to join his outstanding research team as a PhD student despite my "second class degree". There cannot be enough appreciation for creating such an amazing work group, where the profound scientific advice always comes along with cordial friendliness.

Especially I am very grateful for the collaboration with my supervisor Klaus-Dieter Kreuer. The trust he laid in me constantly pushed me to reach out for the next higher bar. His unlimited willingness to share his in-depth knowledge about physical chemistry and matters beyond science have left lasting impressions which I will always cherish.

Prof. Dr. Frank Gießelmann and Prof. Dr. Sabine Ludwigs have my thanks for honoring me as co-corrector and exam chairman for my PhD exam.

Thanks to Jan Melchior who introduced me as a newcomer to the PFG NMR spectroscopy and taught me all the fundamentals. I appreciate all discussions about NMR and the experimental help I experienced from Igor Moudrakovski and Günter Majer.

A big thank you goes for all the technical support I enjoyed from Florian Kaiser, Armin Sorg, Uwe Traub, and Udo Klock, who ensured along with the help of the mechanical workshop and the glassblowing workshop smooth experimentation.

In particular, I want to thank Annette Fuchs for being a helping hand in the laboratory in uncountable situations.

Thanks to Samir Hammoud for helping with the elemental analysis by atomic spectroscopy.

I want to thank Dr. Alain Farchi for preparing the technical set-up and helping me with the SAXS measurements at the CEA Grenoble.

For providing polymer materials whose access was indispensable for this work, I thank Dr. Michael Schuster from fumatech GmbH, Prof. Chulsung Bae and his group from the Rensselaer Polytechnic Institute (BP-ArF4), and last but not least Dr. Giorgi Titvinidze from the Agricultural University of Georgia (sPSO2 materials), who provided not only chemicals but always encouraging advice during his memorable, joyful visits and common conference attendances.

Thanks to Tongshuai Wang from the department of chemical engineering of the University of Illinois led by Prof. Dr. Sangil Kim for performing the VRFB tests.

Furthermore, I want to thank Sofia Weiglein and Madeleine Burkhardt for always reliable advice around organizational matters and bureaucracy, which was a great relief.

I want to express my gratitude for the entire Maier department. I appreciate the company and conversations of all colleagues and fellow PhD students, in particular Markus Joos, Simon Lorger, Maximilian Hödl and Torben Saatkamp, who became close friends. I especially thank Torben for sharing sorrow and joy during our joint adventure and hope our brotherly bond will never dissolve.

Thanks to my dear friend Fabian who started the journey in chemistry together with me. For all the "Schwabi-Runden" I want to thank my friends Dominic and Moritz who always had time for me when I needed a break.

Finally, I want to thank my family, my parents Brigitte and Jürgen, and my sister Franziska, who had to put up with my whims and still supported me throughout my whole life.

I especially thank Sanna Tyralla for all the love and empathy she bestowed upon me. She is the motivation of my life.

Contents

List of abbreviations	III
List of figures	V
List of tables	VII
Abstract	1
Zusammenfassung	3
1 Introduction	5
1.1 Challenges of electrochemical devices	7
1.2 Insights from biological systems	10
2 Methodology	13
2.1 Model ions	14
2.2 Model ion exchange membranes	15
2.3 Elemental analysis	19
2.4 Impedance spectroscopy	20
2.5 Nuclear magnetic resonance (NMR) spectroscopy	21
2.5.1 Spin relaxation	22
2.5.2 Pulsed field gradient NMR	23
2.6 Small angle x-ray scattering	25
2.7 Hittorf method	27
2.8 Vanadium redox flow battery testing	27
3 Theoretical background	30
3.1 Donnan equilibrium	31

3.2	Activity coefficients	35
3.3	Morphology of IEMs	36
4	Results and discussion	39
4.1	Specific interactions	40
4.1.1	Selective ion transport in dissolved ionomers	40
4.1.2	Ion partitioning in membranes: validating the role of acidity . . .	46
4.1.3	Ion partitioning in Nafion: ion association	50
4.1.4	Donnan exclusion: extended Donnan equation	55
4.1.5	Transference experiments	59
4.1.6	Concluding remarks	61
4.2	Electroselectivity	65
4.2.1	Setting	65
4.2.2	Mono- vs. divalent co- and counter-ions	66
4.2.3	Concluding remarks and outlook	71
4.3	Impact of morphology	72
4.3.1	Setting	72
4.3.2	Sieving effect in an IEM	73
4.3.3	Ionic transport of VRFB electrolyte in IEMs (VO^{2+} vs. H^+)	76
4.3.4	Aqueous domain width of membranes in VRFB environment . . .	80
4.3.5	Review of VRFB performances of several membranes	83
5	Summary	89
	Bibliography	91
A	Experimental details	101

List of abbreviations

AEM	anion exchange membrane
CE	coulombic efficiency
CEM	cation exchange membrane
EE	energy efficiency
FID	free induction decay
ICP	inductively coupled plasma
IEC	ion exchange capacity
IEM	ion exchange membrane
MWCO	molecular weight cut-off
NMR	nuclear magnetic resonance
OES	optical emission spectroscopy
PAA	poly(acrylic acid)
PFG	pulsed field gradient
PFSA	perfluorosulfonic acid
PGSE	pulsed gradient spin echo
PSS	sulfonated polystyrene
RF	radio frequency
RFB	redox flow battery
SAXS	small angle x-ray scattering
sPEEK	sulfonated poly(ether ether ketone)

List of abbreviations

sPSO2 sulfonated poly(phenylene sulfone)

VE voltage efficiency

VRFB vanadium redox flow battery

List of Figures

1.1	Scheme of a chloralkali electrolysis cell	8
1.2	Schematics of ion transport in biological systems	11
2.1	Schematic of hydrated radii of Li^+ and Cs^+	15
2.2	Chemical structure of PFSA	16
2.3	Chemical structure of hydrocarbons	17
2.4	Chemical structure of BP-ArF4	18
2.5	Typical chemical structure of AEMs	18
2.6	Schematic diagram of the PGSE pulse sequence	24
2.7	Attenuation of an ^1H spectrum in a PGSE experiment as a function of the gradient strength g	25
2.8	Schematic of a SAXS setup	26
2.9	Scheme of a vanadium redox flow battery	28
3.1	Mole fraction of counter-ions in an ion exchange membrane (IEM) as a function of the molality of an adjacent 1,1 electrolyte for different fixed- ion concentrations.	34
3.2	Illustration of the locally flat morphology of Nafion	37
3.3	Schematics of the microstructure of Nafion and hydrocarbon membranes	38
4.1	Experimental setup for measuring ion partitioning of dissolved ionomers	41
4.2	Average Li^+ and Cs^+ diffusion coefficients in dissolved ionomers	44
4.3	Literature and own data of Li^+/Cs^+ partitioning in Nafion	47
4.4	Li^+/Cs^+ partitioning of several CEMs of different acidity	48
4.5	Li^+/Cs^+ partitioning of different CEMs with the same acidity	49

4.6	NMR data on counter-ion association of Li^+ and Cs^+	51
4.7	Calculated Li^+/Cs^+ partitioning in Nafion	53
4.8	Ion partitioning fits with a partitioning coefficient	54
4.9	Fractions of Li^+ and Cs^+ bound to the fixed ionic group of Nafion	55
4.10	Co-ion uptake of Nafion in a CsCl solution	56
4.11	Co-ion uptake of Nafion in a LiCl solution	58
4.12	Hittorf experiment for CEMs in LiCl/CsCl solutions	60
4.13	Hittorf experiment for an AEM in HCl solution	62
4.14	Schematic of a CEM with a AEM layer for selective monovalent cation transport.	66
4.15	Calculated mono- and divalent counter-ion (cation) uptake in a CEM . . .	68
4.16	Fraction of monovalent cation uptake	69
4.17	Chemical structure of tetrakis(hydroxymethyl)phosphonium	73
4.18	^1H PFG NMR data of Nafion with phosphonium counter-ions	74
4.19	Diffusion coefficients of water and tetrakis(hydroxymethyl)phosphonium in Nafion	75
4.20	Ratio of the diffusion coefficients of water and tetrakis(hydroxymethyl)- phosphonium in Nafion	76
4.21	H^+ and VO^{2+} molar conductivities in Nafion and sPSO2-360	78
4.22	H^+ and VO^{2+} conductivity ratios in Nafion and sPSO2-360	79
4.23	Schematic illustration of a morphological bottleneck at the onset of se- lectivity increase	80
4.24	SAXS patterns of Nafion and BP-ArF4 in H^+ form in water and in VRFB electrolyte	81
4.25	Chemical structure of the polybenzimidazole PBI-O	81
4.26	SAXS pattern of PBI-O in VRFB electrolyte	82
4.27	CE and VE of a VRFB with Nafion and BP-ArF4	83
4.28	$CE(J)$ of a VRFB with sPSO2-360 and Nafion membranes of various thickness	85
4.29	Theoretical energy efficiencies of VRFBs with different membranes	87

List of Tables

2.1	Hydration enthalpies, molar conductivities, diffusion coefficients, and hydrated radii of alkali metal ions	14
4.1	Partitioning data of dissolved ionomers sorted by acid strength	42
4.2	Estimated transference numbers of Li^+ and Cs^+ in dissolved ionomers . .	46
4.3	Li^+ and Cs^+ transference numbers of different cation exchange membranes (CEMs)	61
4.4	Width of aqueous ionic domain d_{aq} of Nafion and BP-ArF4	82
4.5	Specific vanadium crossover current density j_{D} and membrane specific conductivity σ of different membrane materials for vanadium redox flow batteries (VRFBs)	86

Abstract

This thesis investigates chemical and morphological effects on ion partitioning and mobility in ion exchange membranes (IEM) in thermodynamic equilibrium with aqueous environments and discusses consequences for ionic transport including its selectivity (transference number).

Most experiments are done with Nafion membranes, but also other cation and anion exchange membranes with chemically different fixed-ionic groups are included in this work. Typically, such membranes show a hydrophobic / hydrophilic phase separated morphology with aqueous ionic domains enabling transport of ionic and aqueous species. Membranes of this study are chosen such that their average separation of fixed-ions is well above the Bjerrum length of water as to minimize polyelectrolyte effects such as Manning's counter-ion condensation. Nevertheless, electrostatic effects are included into the discussion of the data.

Electrochemical methods, NMR spectroscopy, and chemical analysis are used for studying chemical interaction of model ions with fixed-ionic groups and its effect on ion partitioning. Data from small-angle-x-ray-scattering (SAXS) and pulsed field gradient NMR reveal relations between the mobility of ionic species of different size and morphological features of IEMs.

For cation exchange membranes, the binding interaction between cation (counter-ion) and the acidic anion (fixed-ion) increases with increasing electro-positivity of the cation and increasing Brønsted acidity of the fixed-ionic group. Extending the Donnan-equation by terms describing the corresponding ion-association equilibria and the effect ion hydration has on ion activity coefficients allows for a quantitative description of ion partitioning. This comprises both the uptake of co-ions and the

selectivity of counter-ion uptake. Selective counter-ion uptake is shown to decrease total ionic conductivity leaving ionic transference numbers (ion transport selectivity) virtually unchanged.

Key for obtaining high selectivity of ion conductivity (high transference number) is “ion sieving”, i.e. the sharp decrease of ion mobility for widths of aqueous ionic domains below the extension of a particular type of mobile ion including its hydration shell.

Finally, insights obtained on model systems are applied to the more complex situation of vanadium redox flow batteries (VRFB). Coulomb and voltage efficiencies recorded for VRFBs with different membranes are explained, and membrane design strategies for this particular application are provided.

Zusammenfassung

In dieser Arbeit werden die Auswirkungen von chemischen Wechselwirkungen und morphologische Gegebenheiten auf die Ionenverteilung und Ionenbeweglichkeit in Ionenaustauschermembranen (IEM) im thermodynamischen Gleichgewicht mit ihrer Umgebung untersucht. Die Folgen auf ionischen Transport und dessen Selektivität im Sinne von Überföhrungszahlen werden erläutert.

Die meisten Experimente wurden an Nafion-Membranen durchgeführt, aber es wurde auch der Zugang zu weiteren, teils nicht im Handel erhältlichen, Kationen- und Anionenaustauschermembranen mit chemisch unterschiedlichen Festionen genutzt. Typischerweise weisen diese Membranen eine hydrophob / hydrophil phasenseparierte Morphologie auf, wobei der ionische Transport über die wässrige ionische Domäne stattfindet. Die untersuchten Membranen wurden möglichst so gewählt, dass die durchschnittlichen Abstände der Festionen über der Bjerrum-Länge liegen, um Polyelektrolyteffekte wie Mannings Gegenionen Kondensation zu minimieren. Dennoch werden auch elektrostatische Effekte in die Auswertung der Daten einbezogen.

Elektrochemische Methoden, NMR Spektroskopie und chemische Analyse werden verwendet, um die chemische Wechselwirkung von Gegenionen und Festionen und die Auswirkungen auf die Ionenverteilung zu untersuchen. Daten aus der Kleinwinkelstreuung und der Feldgradienten NMR offenbaren Beziehungen zwischen der Beweglichkeit von ionischen Spezies verschiedener Größe und morphologischen Gegebenheiten von Ionenaustauschern.

Für Kationenaustauscher steigt die bindende Wechselwirkung zwischen Kation (Gegenion) und der Säuregruppe (Festion) mit steigender Elektropositivität des Kations

und mit steigender Brønsted Säurestärke des Festions. Das Erweitern der Donnan-Gleichung durch Einbeziehung des entsprechenden Ionen-Assoziationsgleichgewichts und der Ionenhydratisierung ermöglicht eine quantitative Beschreibung der Ionenverteilung. Es wird gezeigt, dass die selektive Aufnahme bestimmter Gegenionen bei gleichzeitig sinkender Leitfähigkeit die Überföhrungszahl, also die Transportselektivität, kaum beeinflusst.

Der Schlüssel zu einer hohen Selektivität bei der Ionenleitung ist das "Ionen-Sieben", also der starke Abfall der Beweglichkeit von Ionen, wenn die Breite der wässrigen ionischen Domäne unterhalb der Ausdehnung des entsprechenden Ions mit seiner Hydrathölle sinkt.

Schließölich werden die Einsichten aus den Modellsystemen in der komplexen Situation einer Vanadium-Redox-Flow-Batterie (VRFB) angewandt. Die an verschiedenen Membranen gemessenen Coulomb- und Spannungseffizienzen werden erklärt und Designstrategien für Membranen hinsichtlich dieser Anwendung dargestellt.

Chapter 1

Introduction

Fast and selective transport of a particular type of ion across membranes separating aqueous media of different composition is key to essential biological and technical processes such as transmission of electrochemical signals and electrochemical energy conversion. Nature already achieved the goal of fast, selective transport with semi-permeable cell membranes, while separators in electrochemical devices are still the core subject of investigations when it comes to developing more efficient energy conversion or desalination processes at high rates. Fast transport which is exclusive for a particular species seems to be a very rare phenomenon. Aqueous electrolytes provide fast ionic transport but lack selectivity, since the dynamics of the species in these systems is highly coupled. On the other hand, solid state ionic conductors enable selective ionic transport by exchanging only one type of mobile ion with its environment and decoupling the ion's long range dynamics from the rest of the immobile structure. Unfortunately, at ambient conditions, the conductivity of such materials usually remains well below the conductivity of aqueous electrolytes.

Ion exchange membranes (IEMs) have the chance to combine the best of both worlds. Having a charged immobile polymeric backbone, they exchange and conduct predominantly ions of opposite charge (counter-ions) with their aqueous environment. They are called cation exchange membranes (CEMs) if the fixed-ionic groups are charged negatively (e.g. $-\text{SO}_3^-$ or $-\text{COO}^-$) and anion exchange membranes (AEMs) if they are charged positively (e.g. $-\text{N}(\text{CH}_3)_3^+$). Such ionomers hydrate in the presence of

water due to their hygroscopic ionic groups and they phase-separate on the nanometer scale, because of their hydrophobic polymer backbone. The polymeric phase may even present some crystallinity, i.e. an ordered structure like a crystalline solid, while the aqueous phase containing the mobile counter-ions provides an environment almost identical to an aqueous electrolyte. Still, the decoupling of the counter-ions from the dynamics of the fixed-ions at simultaneously high mobility comes with restrictions. Firstly, the exclusive transport of counter-ions is only valid for an infinite dilute electrolyte as adjacent solution, because at higher concentrations ions of the same charge as the fixed-ions (co-ions) may enter the membrane and also diffuse fast. Secondly, there is not necessarily a selectivity between different types of counter-ions. The latter, however, is of major importance for both biological systems and certain electrochemical applications. Ultimately, the selectivity of ion transport comes down to the partitioning and the mobility of the individual species in the membrane. This thesis approaches the investigation of the origin and relation of these two quantities by discussing respective data of systematically chosen model ions and ionomers and thereby identifying controlling parameters. As motivation, electrochemical devices using IEMs are presented in chapter 1.1 and the importance of selective separators is explained. Ideas and insights from semi-permeable cell membranes, which can help understanding the underlying phenomena, are summarized in the chapter 1.2.

1.1 Challenges of electrochemical devices

Electrochemical devices which use IEMs either actively separate different ionic species or gain energy from the potential difference of separated species. In each case the IEM needs to conduct a specific ion while preventing other species (this may be ions or neutral species) from crossing the membrane. Conceptually there are several different ways to classify the type of selectivity of a membrane: i) towards neutral species, i.e. molecules or ion pairs ii) between oppositely charged ions and iii) between ions that carry charges of the same sign.

The membrane's ability to retain neutral molecules (e.g. gas separation in fuel cells) is a property dominated (among others) by the porosity and the pore geometry of the membrane. In many electrochemical devices ions are present in high concentrations and possibly form neutral ion pairs. Hence, the transport selectivity of neutral species may superimpose the other two selectivities.

Selectivity between oppositely charged ions is based on the fact that the fixed-ions in IEMs are compensated by (more or less) mobile, oppositely charged ions, whereas same charged ions are mostly rejected. Applications like the chloralkali process (see figure 1.1), diffusion dialysis [1] or (reverse) electrodialysis make use of this property of IEMs.

In the case of a chloralkali electrolysis cell, a CEM is used as separator between the sodium chloride feed solution on the anode side and the initially pure water on the cathode side, where sodium hydroxide solution is produced. Chloride anions on the anode side are consumed and leave as neutral chlorine gas. As a consequence, the remaining sodium cations pass the CEM to keep the electroneutrality. By hydrogen evolution from water reduction, hydroxide ions are produced at the cathode. As they are anions, they are rejected from the CEM and cannot balance the charges instead of the sodium ions. Also, chloride anions are prevented from moving along the concentration gradient which leads to sodium hydroxide as product on the cathode side. However, with increasing concentrations the CEM property of selective cation transport over anion transport fades, causing severe losses in purity and efficiency. The challenge of IEMs lies in the ability to keep their characteristic permselectivity up to

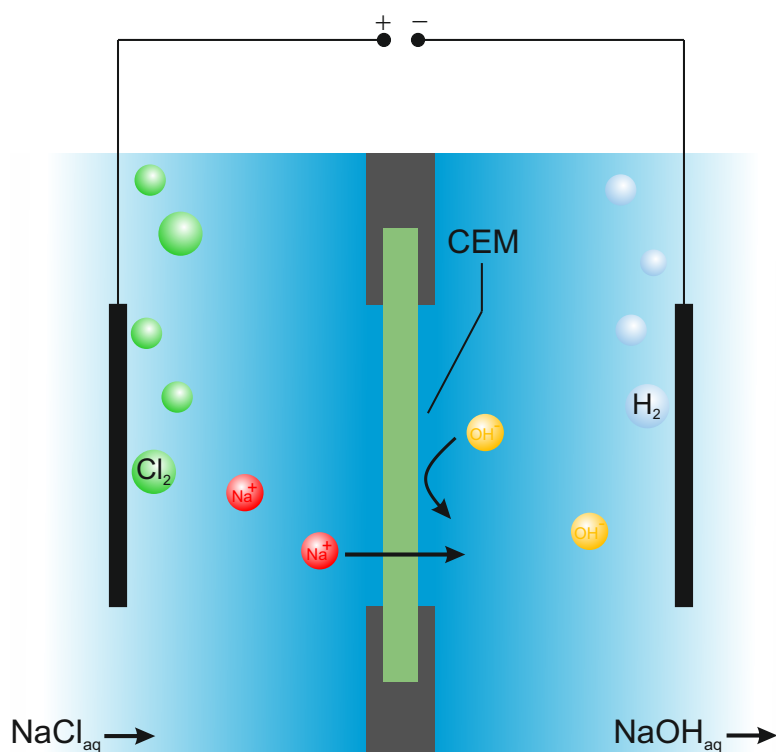


Figure 1.1: Scheme of a chloralkali electrolysis cell. At the anode side NaCl solution is fed and chloride anions are oxidized to chlorine gas while at the cathode hydrogen evolves. The CEM separating the two compartments is transporting sodium ions from the anode to the cathode side for balancing the charges, while it rejects the forming hydroxide ions on the cathode side.

high concentrations of the adjacent solutions. An interesting question is, whether such an ability depends on the chemical nature of the membrane's functional group and the corresponding counter-ions or whether it is simply dominated by the fixed-ion concentration.

The third kind of selectivity is the discrimination among ions with charges of the same sign, like ion channels in biology are capable of. This selectivity is relevant for redox flow batteries (RFBs), a rising application for energy storage. RFBs consist of two compartments containing media with different redox active species (e.g. $\text{Fe}^{2+}, \text{Fe}^{3+} | \text{Cr}^{3+}, \text{Cr}^{2+}$ or $\text{Zn}, \text{Zn}^{2+} | \text{Br}_2, \text{Br}^-$ or $\text{Mn}^{2+}, \text{Mn}^{3+} | \text{V}^{3+}, \text{V}^{2+}$), which can scale

in volume (capacity) independently from the separator area (power density). The most common representative is the vanadium redox flow battery (VRFB):



Both redox pairs are dissolved in sulfuric acid adding the ions H^+ , HSO_4^- , and SO_4^{2-} to the electrolyte. Obviously all involved redox active ions are cations. In order to keep the charges in the two compartments balanced, either sulfate anions (SO_4^{2-}) and bisulfate anions (HSO_4^-) or protons (H^+) need to cross the membrane while the redox active species must remain separated, because every crossing vanadium species is directly reducing the capacity of the battery. Due to the high mobility of protons compared to the available anions, transport of protons is superior for the battery's efficiency. Therefore, the challenge lies in finding a membrane providing this selective preference of protons over other cations as mobile charge carrier.

1.2 Insights from biological systems

The selectivity of ion transport across biological membranes is mostly the consequence of the selective uptake of a particular type of ion. For example the selective coordination of a specific kind of ion by so-called ionophores is key for obtaining selective ionic trans-membrane transport. This type of ion transport comprises the flux of charged ion-ionophore complexes with the usually more numerous neutral ionophores drifting in the opposite direction (see figure 1.2). The most prominent ionophore is valinomycin, a cyclodecadepsipeptide which is produced by numerous kinds of streptomycetes. Valinomycin is a natural antibiotic forming stable complexes with potassium ions. The lipophilic character of the ionophore allows such complexes to enter and cross the lipid membrane of bacteria. In this way, they can transport K^+ out of the cell depolarizing the resting potential across the cell membrane which causes the cell to die. The specificity for this process is orders of magnitude higher for K^+ than for Na^+ . On the other hand, the conduction mechanism of transmembrane ion conducting channels is fundamentally different, although the channels are chemically related to ionophores. The structure was first revealed by the MacKinnon group in 1998 by an x-ray diffraction study on crystallized potassium channels [2]. As illustrated in figure 1.2 (right), these channels are formed by proteins spanning the entire phospholipid membrane with a width of approximately 3.4 nm, but the part providing the channel with its selectivity, the so-called selectivity filter, is only 1.2 nm long. As in valinomycin, the potassium ion coordinates to carbonyl groups of the proteins' backbone pointing toward the center of the channel. The authors actually state that the binding to carbonyl groups mimics the stabilizing effect of K^+ hydration and that structural constraints keep the selectivity filter open to coordinate K^+ ions but not smaller Na^+ ions. As a common explanation in literature, the preference of K^+ over Na^+ in of both ionophores and ion selective channels is attributed to the structurally precise fit between the K^+ ion and carbonyl groups lining the rigid and narrow pore [3]. On the other hand it should be noted, that proteins are relatively flexible structures that undergo rapid thermal atomic fluctuations larger than the small difference in ionic radius between Na^+ and K^+ [4,5] making steric reasons less likely. Interestingly, valinomycin and the mentioned ion

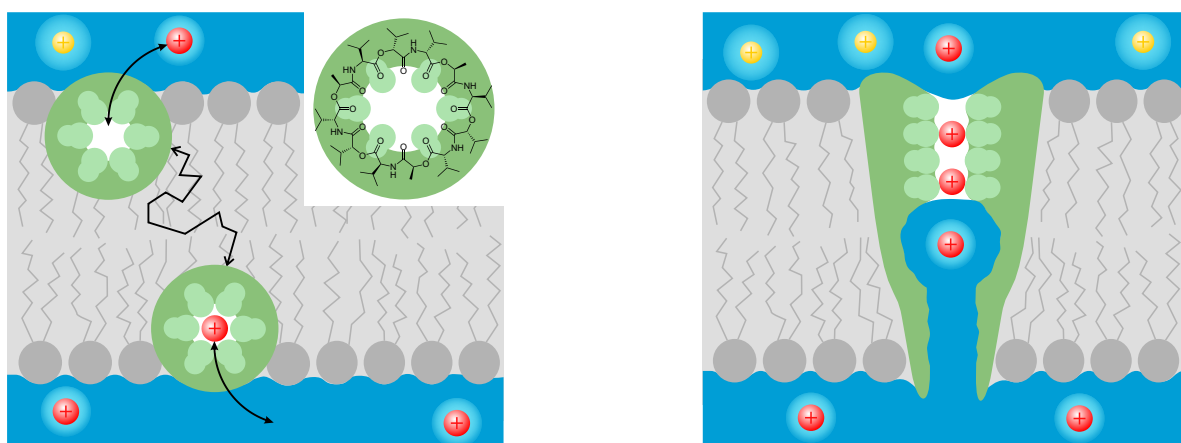
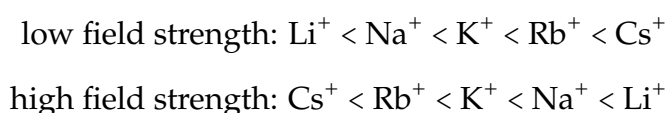


Figure 1.2: Schematics of ion transport in biological systems. Left: Valinomycin dissolved in the lipophilic interior of a phospholipid membrane where it acts as a mobile carrier for cross-membrane transport of exclusively potassium ions K^+ (red) while being in presence of sodium ions Na^+ (yellow). Also the molecular structure of the ionophore valinomycin with its 6 carbonyl groups coordinating K^+ is given. Right: Illustration of the structure of a K^+ conducting channel as revealed by the MacKinnon group [2]. Note, that the narrow hydrophobic selectivity filter at the top has four sites where K^+ can localize by coordinating to 8 carbonyl groups. Both ends of the selectivity filter are in contact with bulk water.

channel may separate Na^+ and K^+ , but they are also sensitive for other (not common in biological systems) alkali ions of higher atomic number like Rb^+ or Cs^+ [6,7]. The higher selectivity though comes with less efficient conduction, hinting to a stronger binding with the carbonyl groups, while e.g. Na^+ interacts more strongly with water molecules. Then, it is not the ion size per se, but the related electrostatic and electronic properties that make the difference. Along this line, the electrostatic model of Eisenman [8,9] describes the preference of alkali-metal ions binding to ligands of different field strength (“Eisenman sequences”):



As for high field strength ligands ion affinity is determined primarily by electrostatic forces, the ion with the smallest radius (highest charge density) will be preferred. For

low field strengths the sequence is inverted, as the hydration energies become dominating. Long before the first structural analysis, these sequences were used for explaining ion selectivity of biological channels, and also for different ionophores. The importance of specific interactions compared to steric effects is underlined by the chemically different nature of the respective ionophore. For example for Li^+ selective ionophores their selectivity is attributed to the aliphatic substituents, which are electron donating, attached next to the carbonyl group [10]. Various ionophores were discovered and prospects of their selectivities explored by the group around Simon at the ETH Zürich (consequently, most ionophores are named after the institute) [11]. They invented the first ion selective electrodes by introducing ionophores into a PVC matrix. The ionophores as selective carriers enable the formation of stable Nernst potentials across the membrane corresponding to different concentrations of the respective ion. At the same time the conductivity of such membranes is rather low, typically in the $\mu\text{S cm}^{-1}$ range [12]. The reason for the relatively high conductivities in biological systems lies in the short range ions need to overcome, as the phospholipid membranes and especially the selectivity filter are very thin. When it comes to the separator function in electrochemical devices, membranes need to withstand pressure and mechanical stress. To ensure the mechanical robustness, a certain thickness is required, that makes the selective transport mechanisms of biological systems not applicable. Still, their concepts are valuable for considerations in the field of ion exchange membranes.

Chapter 2

Methodology

This work draws its conclusions from observations of model systems consisting of distinct ions and polymers, whose choice is presented in chapter 2.1 and 2.2. The measurement techniques used in this work are elemental analysis for characterizing ion uptake and partitioning in IEMs (chapter 2.3), impedance spectroscopy for conductivity measurements (chapter 2.4), nuclear magnetic resonance (NMR) for obtaining data about specific interaction and diffusivity of ions (chapter 2.5), small angle x-ray scattering (SAXS) for information about the morphology of IEMs (chapter 2.6), the Hittorf method for obtaining transference numbers (chapter 2.7) and Vanadium redox flow battery testing for measuring the device's efficiency as a result from selective transport (chapter 2.8).

2.1 Model ions

In this work the two ions with the most extreme properties of the alkali metal series, the end members Li^+ and Cs^+ , are investigated. Li^+ is the smallest, hardest ion in the series, while Cs^+ is the largest and softest, which is why they have different properties in solution (see therefore table 2.1, where some properties are listed). Ignoring the

Table 2.1: Hydration enthalpies ΔH_{hydr}^0 [13], molar conductivities Λ_{m}^0 [14], diffusion coefficients D , and hydrated radii R_{H} of alkali metal ions at infinite dilution (referring to 25 °C).

	$\Delta H_{\text{hydr}}^0 / \text{kJ mol}^{-1}$	$\Lambda_{\text{m}}^0 / \text{cm}^2 \text{S mol}^{-1}$	$D / 10^{-5} \text{cm}^2 \text{s}^{-1}$	$R_{\text{H}}/\text{\AA}$
Li^+	-519	38.6	1.03	2.38
Na^+	-409	50.0	1.33	1.84
K^+	-322	73.5	1.96	1.25
Rb^+	-293	77.8	2.07	1.18
Cs^+	-264	77.2	2.06	1.19

entropy change associated with ion coordination in an aqueous solution, the relevant measure is the heat of hydration ΔH_{hydr}^0 . Water is a medium with high static dielectric constant stemming from the large oscillator strength of the Debye relaxation, which is a collective process comprising reorientation of water dipoles and translational degrees of freedom such as the polarizability of protons within hydrogen bonds. The interaction of water with ions is therefore governed by electrostatics which naturally explains the strongly increasing hydration enthalpy with increasing ion charge and decreasing ion size, both increasing the electric field strength around the ion. For monovalent alkali metal ions, the hydration enthalpy is largest for Li^+ which is twice the heat of hydration of the least hydrophilic Cs^+ . The hydration process involves the formation of a stable hydration shell, which is largest for the small Li^+ (see the scheme in figure 2.1). This is why the smallest alkali ion has the largest hydrodynamic radius R_{H} and the smallest diffusion coefficient D in water. The hydrodynamic radius is the radius of a hypothetical solid sphere that has the same diffusion properties in a solvent as the

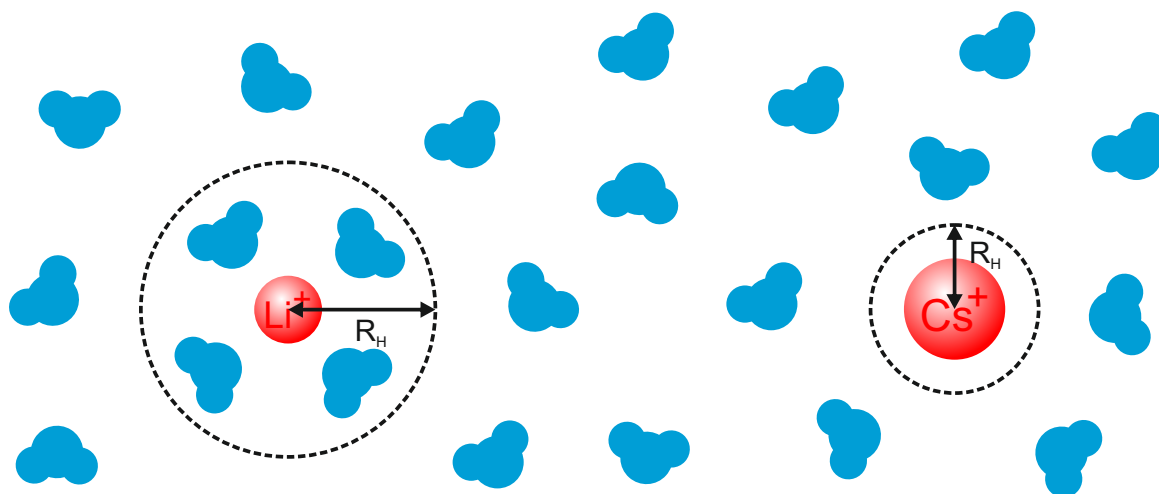


Figure 2.1: Schematic of hydrated radii of Li^+ and Cs^+ comprised of their own radius and their hydration shell. The large hydrodynamic radius of Li^+ results in a lower diffusion coefficient compared to the less strongly coordinated Cs^+ .

particle described. It is related with the diffusion coefficient via the Stokes-Einstein equation:

$$R_H = \frac{k_B T}{6\pi\eta D} \quad (2.1)$$

where D is the particle's diffusion coefficient and η the solvent's viscosity (for water at 25 °C the viscosity is $\eta = 0.891$ mPa s).

Compared to Li^+ , Cs^+ not only has a lower field strength and therefore a lower hydration enthalpy, it is also electronically much more polarizable (3.34 \AA^3 for Cs^+ compared to 0.03 \AA^3 for Li^+ [15]) and has a lower electronegativity. Thus, they fundamentally differ in the way they chemically interact with their corresponding oppositely charged species. In this work, this specific interaction between the model ions, Li^+ and Cs^+ , and the functional groups of model IEMs, introduced in the following section, is investigated.

2.2 Model ion exchange membranes

In general there are two overarching types of ion exchange membranes (IEMs): perfluorinated polymers and hydrocarbons. The former, perfluorosulfonic acids (PFSAs),

are the most common in industry due to their good chemical stability and high conductivity. Its most famous representative is Nafion, whose chemical structure is given in figure 2.2. Nafion is a long side chain PFSA, while Aquivion is categorized as short

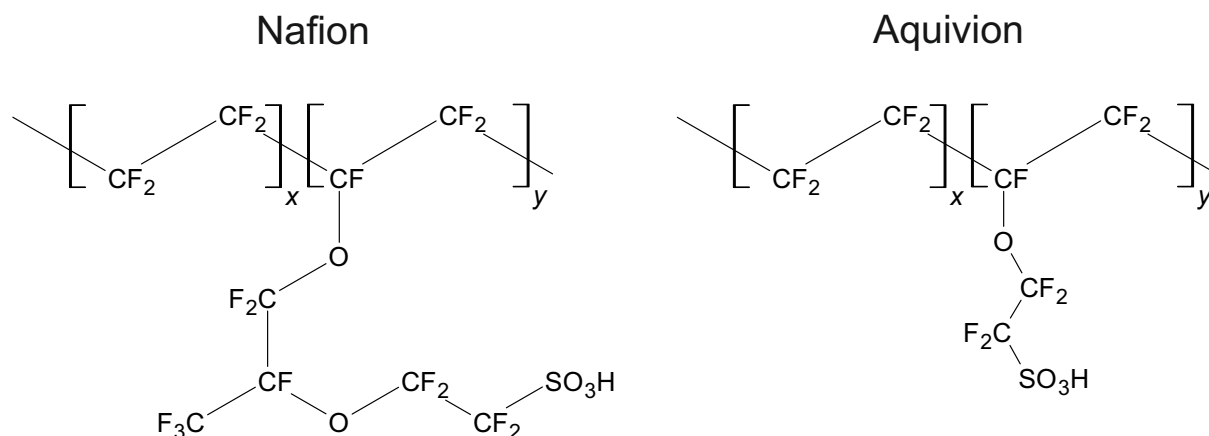


Figure 2.2: Chemical structure of perfluorosulfonic acids (PFSAs). Left Nafion, right: Aquivion.

side chain PFSA, allowing for higher ion exchange capacities (IECs), which is the equivalent of functional groups per mass of dry polymer. The fluorine atoms in the side chain next to the terminating sulfonic acid group withdraw electrons due to their high electronegativity ($-I$ effect). Thereby they increase the acidity of the functional group to the level of a super acid with a pK_a of around -6 [16]. The hydrophobic backbone on the one hand and the hydrophilic acid group on the other give rise to a distinct phase separation on the nanometer scale (see chapter 3.3).

Unless otherwise indicated, measurements with Nafion carried out in this work were done with the version N117, which has a thickness of 7 mils = $178\ \mu\text{m}$ and an equivalent weight $\text{EW}=1100\ \text{g mol}^{-1}$. The equivalent weight refers to the $\text{IEC} = \frac{1}{\text{EW}} = 0.91\ \text{meq g}^{-1}$. Hydrocarbons used in this work are sulfonated poly(ether ether ketone) (sPEEK) and sulfonated poly(phenylene sulfone) (sPSO2). Their structure is given in figure 2.3. As sPEEK representative a blend membrane from fumatech GmbH is used: fumasep FKE-50. The exact composition is not known, but the membrane thickness is $50\ \mu\text{m}$ and the $\text{IEC} = 1.5\ \text{meq g}^{-1}$. Poly(phenylene sulfone)s are used either as fully sulfonated sPSO2-220 ($\text{EW} = 220\ \text{g mol}^{-1}$; $\text{IEC} = 4.54\ \text{meq g}^{-1}$) or half sulfonated sPSO2-360 ($\text{EW} = 360\ \text{g mol}^{-1}$; $\text{IEC} = 2.78\ \text{meq g}^{-1}$). The polymers synthesized according to

references [17,18] were provided by the working group. Membranes are cast in variable thicknesses from dimethylacetamide solution. Compared to sPEEK, sPSO2 has a more polar backbone. The ether groups in sPEEKs have an electron donating effect towards the phenyl ring (+M effect), while the sulfone groups linking the phenyl rings in sPSO2s withdraw electrons, not only improving the chemical stability, but increasing the acidity of the sulfonic acid group. The morphology of these hydrocarbon membranes shows less nano phase separation when compared to PFSA. An interesting

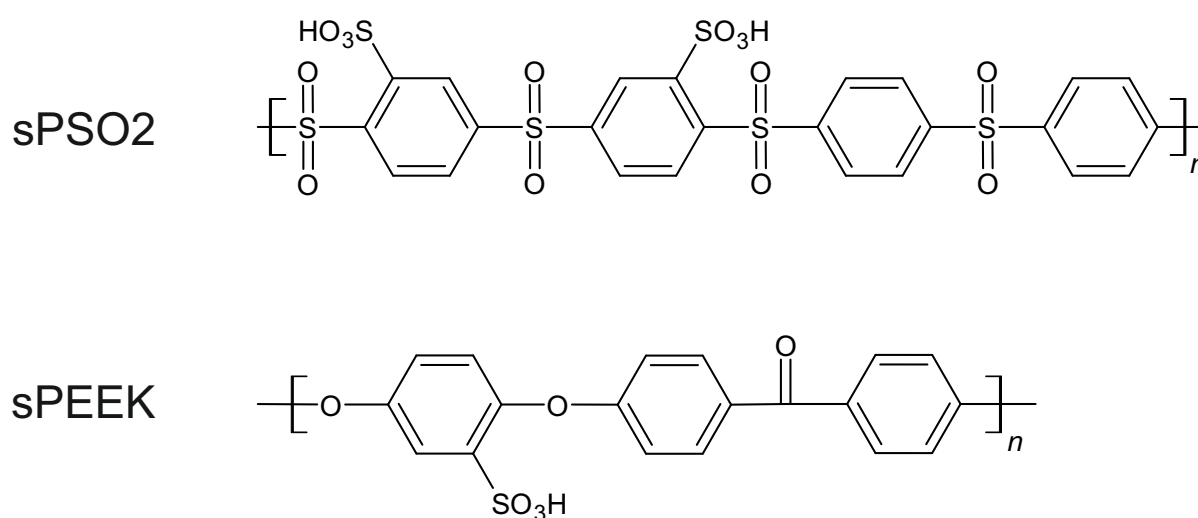


Figure 2.3: Chemical structure of hydrocarbons. Top: sPSO2-360, bottom: sPEEK.

hybrid membrane is the BP-ArF4 provided by the group around Chulsung Bae from the Rensselaer Polytechnic Institute (Troy, New York). Providing a hydrocarbon backbone, the functional group in the side chain is fluorinated as it's the case for PFSA (see figure 2.4). As a consequence of its chemical structure, the morphology on the nm scale is hydrocarbon like, i.e. poor hydrophobic / hydrophilic phase separation, while providing the same chemical nature of the sulfonic acid group (super acidity) as Nafion. The hydrocarbon like structure is proven in chapter 4.3 by measuring the correlation length.

Previous presented IEMs are all cation exchange membranes (CEMs), on which attention is focused in this work. On the other hand, a few experiments on anion exchange membranes (AEMs) are performed, too. The chosen representative is the fumasep

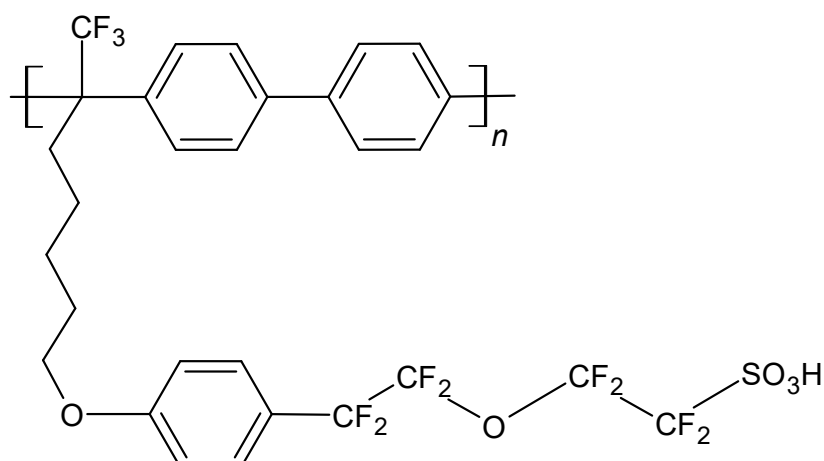


Figure 2.4: Chemical structure of BP-ArF4, a hybrid of PFSA and hydrocarbon.

FAA-3 from fumatech GmbH, but the exact chemical structure is unknown to the author. A typical chemical structure is given in figure 2.5.

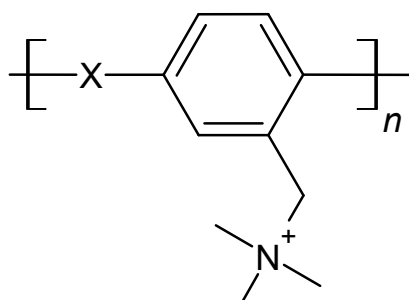
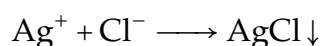


Figure 2.5: Chemical structure of a benzyl group with a trimethylamine group and various polymer linking group (X) encountered in typical AEMs.

2.3 Elemental analysis

Atomic emission spectroscopy is an analytical technique used for the detection of chemical elements. In this work inductively coupled plasma (ICP) optical emission spectroscopy (OES) is employed for quantitative analysis of metal cations. The plasma is first generated in an argon gas stream by a high-frequency electromagnetic field, in which a sample aerosol can be heated up to to 10 000 K. The atoms excited this way emit electromagnetic radiation at wavelengths characteristic of a particular element. The intensity of the emissions from various wavelengths of light are proportional to the concentrations of the elements within the sample. ICP-OES typically allows the detection of trace elements at very low concentrations. However, it is not suitable for all elements as some may have spectral lines outside the detectable wavelength range of the charge-coupled device (light-sensitive sensor).

A technique to quantitatively determine halide ions is potentiometric titration with a silver electrode and a silver nitrate solution. The indicator electrode forms an electrochemical half cell with the test solution (containing e.g. Cl^-). When the titrant (AgNO_3) is added, the initial change of the potential difference to the reference electrode is small as the silver cations precipitate:



At the equivalence point, where the added amount of Ag^+ is the same as the Cl^- amount to be analyzed, the variation of the potential is the steepest. Further halide ions may also be measured in the same experiment as they differ in their solubility product.

2.4 Impedance spectroscopy

In alternating current impedance spectroscopy the frequency dependent potential difference induced by an alternating current I_ω is measured for different frequencies ω (from the mHz to the MHz range). In contrast to direct current measurements which only reveal an overall effective resistance and require reversible electrodes to allow continuous ion transfer with the electrolyte, blocking electrodes suffice for alternating current impedance spectroscopy. As transport of ionic charge carriers is not instant, the phase of the induced voltage U_ω is shifted by φ_ω with respect to the applied current. The resulting frequency dependent complex impedance, which is a measure for the frequency dependent voltage response of an investigated system on the current stimulus, is given by

$$Z(\omega) = \frac{U_\omega}{I_\omega} = Z'(\omega) + iZ''(\omega) \quad (2.2)$$

with the phase shift

$$\varphi(\omega) = \frac{Z''}{Z'} \quad (2.3)$$

Z' is the dispersive real part and Z'' the absorptive imaginary part of the complex impedance.

Measured membrane samples are stacked as round disks of the same area A as the electrodes and a total thickness l resulting in a cell factor of $G = \frac{A}{l}$. The specific ionic conductivity σ can be obtained from the measured ionic resistance R :

$$\sigma = \frac{1}{R \cdot G} \quad (2.4)$$

The ionic conductivity contribution from a single type of charge carrier is related to its ionic drift mobility which is a function of the diffusion coefficient. According to the Nernst-Einstein relation for the Diffusion coefficient D of the charge carrier results:

$$D_\sigma = \frac{k_B \cdot T}{c(z \cdot e)^2} \cdot \sigma \quad (2.5)$$

where z is the number of charges e per charge carrier and c its concentration.

2.5 Nuclear magnetic resonance (NMR) spectroscopy

Nuclear magnetic resonance (NMR) spectroscopy is a spectroscopic method to study the electronic environment of atoms and the interactions with neighbouring atoms and enables thereby the elucidation of the structure and dynamics of molecules. The method allows for electrochemically unchanged samples during the measurement, i.e. the derived quantities are unaffected by the measurement itself and represent actual material properties.

NMR makes use of the fact, that nuclei with a spin of $I \neq 0$ have a spin magnetic moment μ with $m = 2 \cdot I + 1$ degenerated energy states E_m , which split in an external magnetic field in z-direction B_0 (Zeeman effect). The energy splitting is dependent on the gyromagnetic ratio γ of the nucleus and B_0 :

$$E_m = -\gamma B_0 \hbar m \quad (2.6)$$

with the reduced Planck constant \hbar . The magnetic moments precess around the z-axis with a Larmor frequency ω_0 of

$$\omega_0 = \gamma B_0 \quad (2.7)$$

The local field felt by the magnetic moments of the nuclei may differ from the applied field B_0 because the latter induces an orbital angular momentum, which generates a small additional magnetic field at the nuclei. The strength of this additional local field depends on the electronic structure of the molecule in the vicinity of the nucleus. Therefore, the Larmor frequency is slightly different for nuclei in different chemical environments. The difference for a nucleus between its own absolute resonance frequency ν_{sample} and the absolute frequency for a reference nucleus ν_{ref} is called chemical shift δ^{shift} :

$$\delta^{\text{shift}} = \frac{\nu_{\text{sample}} - \nu_{\text{ref}}}{\nu_{\text{ref}}} \cdot 10^6 \quad (2.8)$$

A simple NMR experiment consists of a single 90° radio frequency (RF) pulse which rotates the magnetization into the x,y-plane (transverse direction). The resulting signal, the free induction decay (FID) of the transverse magnetization, is recorded through an RF coil.

2.5.1 Spin relaxation

After an RF pulse the magnetization returns to its equilibrium state M_0 with the components that are in parallel (longitudinal) and perpendicular (transverse) to the B_0 field determined by the relaxation time T_1 and T_2 respectively.

After an inversion of the magnetization by a 180° pulse, the magnetization in z -direction M_z is equilibrating towards M_0 with the longitudinal decay constant T_1 :

$$M_z(t) - M_0 \propto e^{-\frac{t}{T_1}} \quad (2.9)$$

During this relaxation process, energy is released to the environment (the "lattice"), which gives T_1 the name spin-lattice relaxation time. The spin-lattice relaxation is caused by local magnetic field fluctuations created by the movement of the molecules. Relaxation of magnetization in the x,y -plane $M_{x,y}$ (after a 90° pulse) is following the relation:

$$M_{x,y}(t) \propto e^{-\frac{t}{T_2}} \quad (2.10)$$

The transversal relaxation time T_2 is called spin-spin relaxation time, because for this process only reorientations of spins among themselves are involved. Local magnetic moments also influence spin-spin relaxation. If the fluctuations are slow, a molecule remains in its specific magnetic environment for a relatively long time and the spin orientations rapidly move towards their random equilibrium distribution. However, if the molecules change very quickly between different magnetic environments, the differences between the different environments average to zero: the different spins then precess at very similar speeds, thus staying in their pack a bit longer and the spin-spin relaxation is slowed down. In other words, slower molecule motions correspond to small relaxation times T_2 and fast molecule motions correspond to large relaxation times. If the component of magnetization in the x,y -plane decreases with a time constant T_2 , this leads to a broadening of the spectral line, whose full width at half maximum is given by¹:

$$\Delta\nu_{1/2} = \frac{1}{\pi T_2} \quad (2.11)$$

¹Typically, inhomogeneities of the magnetic field lead to further line broadening

This work makes use of the phenomenon of spin-spin relaxation as just described for discriminating between fast, mobile ions, and immobilized species in IEMs (see chapter 4.1).

2.5.2 Pulsed field gradient NMR

Pulsed field gradient (PFG) NMR provides a direct and non-destructive method to obtain the tracer diffusion coefficient of a nucleus [19]. Like other NMR techniques it does not require the information of ion concentration, sample dimension or weight. In comparison to the investigation of molecular dynamics by relaxation time measurements, this method is model free and no presumption about the mechanism of diffusion must be accounted.

Tracer diffusion or self diffusion is the consequence of a thermally induced motion of one particle. In the case of a random walk the probability P of finding a molecule at position r (referenced to its starting position) after a time t is [20]:

$$P(r, t) = (4\pi Dt)^{-\frac{3}{2}} e^{-\frac{r^2}{4Dt}} \quad (2.12)$$

The Gaussian $P(r, t)$, which depends on the net displacement, expands with time and is characterized by the self diffusion coefficient D as a material property. In PFG NMR the displacement associated with diffusion of a nuclei during the diffusion time Δ is measured in an pulsed gradient spin echo (PGSE) experiment (see figure 2.6). When such an echo experiment with an initial 90° RF pulse and a refocusing 180° RF pulse is conducted in a magnetic field gradient g along the z-axis, the nuclei in the sample are spatially labeled through different Larmor frequencies according to their position in the gradient. During the first gradient pulse (with duration δ) the spins dephase along the z-axis and they refocus during the second gradient pulse of same amplitude and length if all nuclei stuck to their position throughout the experiment. After the spins are refocussed the signal can be measured as spin echo. If the nuclei diffuse during the experiment and change their position, spins do not refocus fully and the signal of the

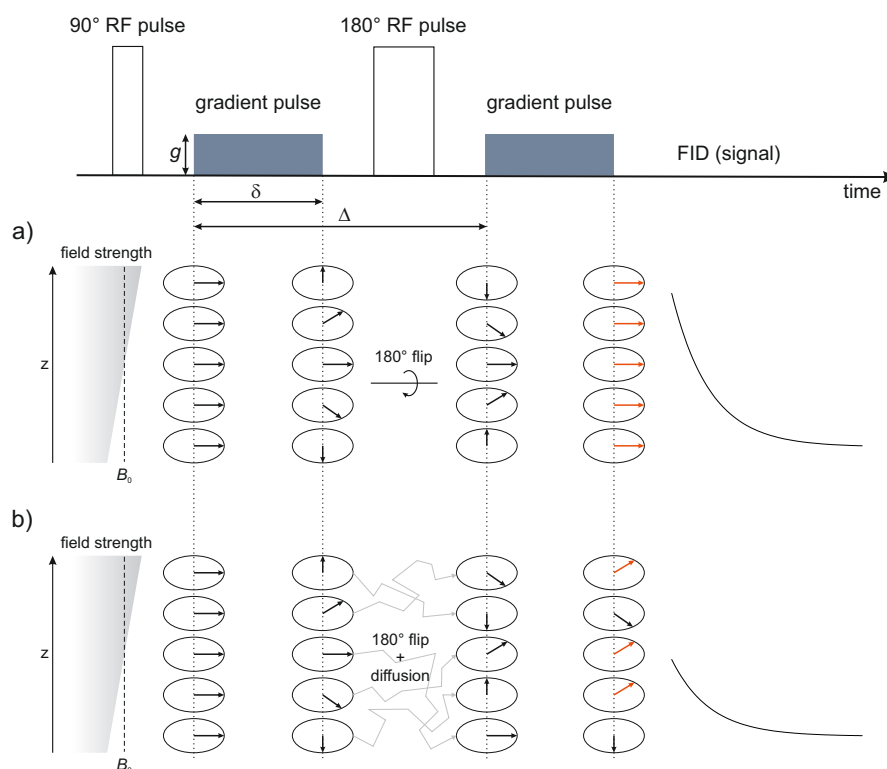


Figure 2.6: Schematic diagram of the PGSE pulse sequence (top). a) The phase evolution of the spins at different locations along the gradient direction in absence of diffusion. The second gradient pulse, which is identical to the first one, completely refocuses (orange) the phase wrap imposed by the first gradient pulse. b) The phase evolution including diffusion within the sample. Less spins are refocused (orange) after the second gradient pulse, resulting in an attenuated signal.

echo is attenuated. This attenuation, the ratio of the echo intensity with and without applied gradient $\frac{I}{I_0}$, is described by the Stejskal-Tanner equation [19]:

$$\frac{I}{I_0} = e^{-\gamma^2 \delta^2 g^2 \left(\Delta - \frac{\delta}{3}\right) D} \quad (2.13)$$

By varying the gradient strength g the diffusion coefficient D can be obtained by fitting the attenuation (see figure 2.7) with equation (2.13).

After the first 90° pulse in a PGSE experiment, spins are precessing in the x,y -plane and decaying with T_2 . Hence, the spin-spin relaxation limits the the maximum applicable diffusion time Δ . As in general $T_1 \geq T_2$, Tanner suggested splitting the 180° RF pulse into two 90° pulses for storing the magnetization in z -direction, where relaxation occurs with T_1 [21]. This sequence is called pulsed gradient stimulated echo (PGSTE) and

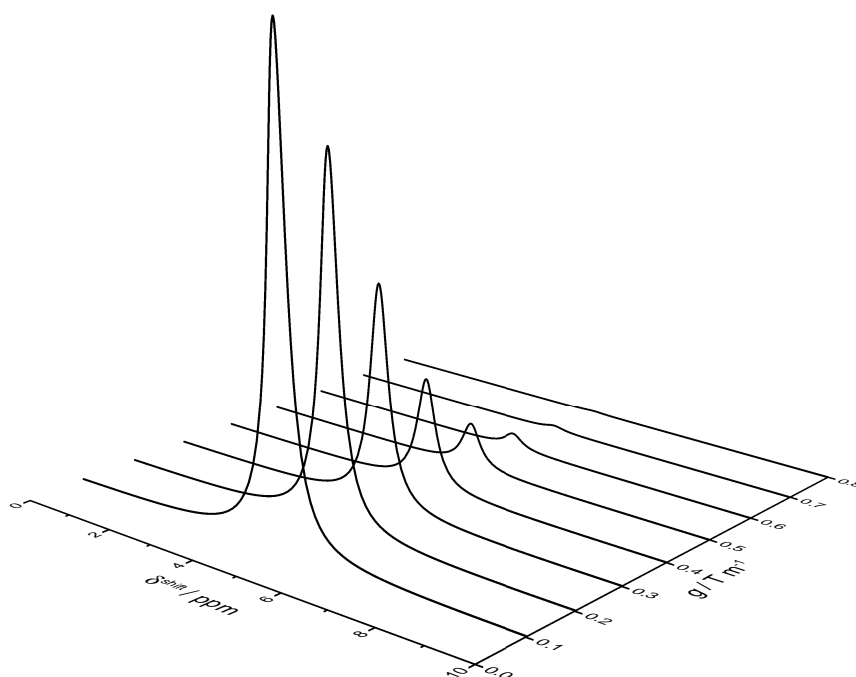


Figure 2.7: Attenuation of an ^1H spectrum in a PGSE experiment as a function of the gradient strength g .

enables measurement of samples with fast spin-spin relaxation or with low diffusion coefficient.

If two species of the same nucleus but different chemical environment are exchanging very fast, the observed diffusion coefficient is the mean average. Is the exchange slow enough, different diffusion coefficients can be attributed to the different species [22,23].

2.6 Small angle x-ray scattering

The nanometer scale structure of IEMs can be investigated by small angle x-ray scattering (SAXS). The elastic scattering of the x-ray beam occurs at boundaries with contrasting electron densities in the sample, which is different for the polymer and the aqueous phase [24]. The evaluation of the local maxima of SAXS patterns is fundamentally based on the Bragg equation [25]:

$$n\lambda_{\text{beam}} = 2d \sin \theta \quad (2.14)$$

with the order of diffraction n , the wavelength of the beam λ_{beam} , the correlation length d , and the scattering angle θ . A typical SAXS setup with its resulting diffraction pattern is depicted in figure 2.8. The intensity of the SAXS patterns is usually plotted as

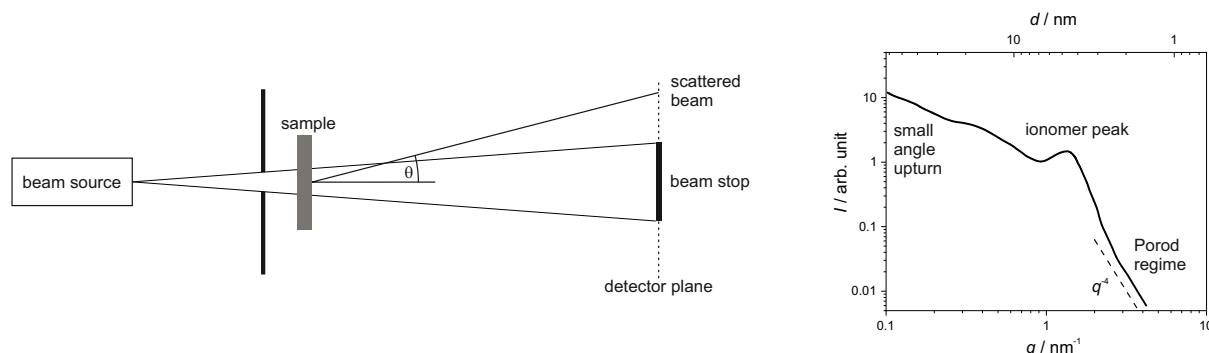


Figure 2.8: Schematic of a SAXS setup (left) and a typical SAXS diffraction pattern (right).

function of the angle dependent scattering vector q described by

$$q = \frac{4\pi}{\lambda_{\text{beam}}} \cdot \sin \theta \quad (2.15)$$

In comparison to crystalline compounds, the scattering maxima in IEMs are relatively broad due to the disorder corresponding to variations of the separation length. The correlation length d at the local maximum of the intensity q_{max} , often referred to as the ionomer peak, can be determined by using equations (2.14) and (2.15) with $n = 1$:

$$d = \frac{2\pi}{q_{\text{max}}} \quad (2.16)$$

For IEMs, the correlation length d is the sum of the aqueous and polymer layer thickness. The intensity of the Porod regime (q^{-4} behaviour) at higher q contains information about the inner water/polymer interface [26]. The small angle upturn is an often discussed feature at low q , which is supposed to bear information on larger scales, but the time dependant change in intensity makes interpretations questionable. From a single SAXS pattern, it's not possible to distinguish between different models of the morphology of an IEM (such as spheres, cylinders, ribbons, ...), because they all result in similar patterns. Water content dependent measurements, on the other hand, elucidate the situation and allow at least for falsification of some models implying distinct scaling behavior of the correlation length (see also chapter 3.3).

2.7 Hittorf method

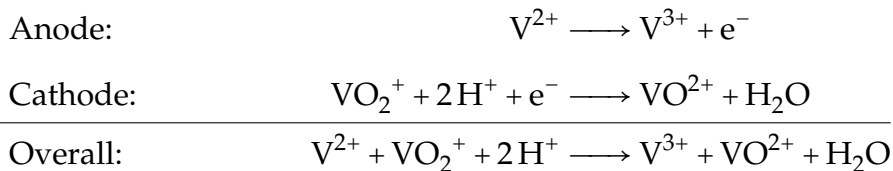
The ion transport number or transference number t_i is the fraction I_i of the total electrical current I_{total} carried in an electrolyte by a given ionic species i :

$$t_i \equiv \frac{I_i}{I_{\text{total}}} \quad (2.17)$$

Differences in transport number of ions arise from differences in their electrical mobility, i.e. diffusion coefficient. A technique for the determination of transport numbers is the Hittorf method which is based on measurements of ion concentration changes near the electrodes. Therefore, electrolysis is carried out in a cell with two compartments, anode and cathode, separated by a central part. Measurement of the concentration changes (e.g. by elemental analysis, see chapter 2.3) in the anode and cathode compartments yield the transport numbers.

2.8 Vanadium redox flow battery testing

An all vanadium redox flow battery (VRFB) is a device where its efficiency is directly linked to the property of the employed membrane governing the exclusive transport of a ionic species which is not part of the redox active couples. A schematic of the setup of a VRFB is illustrated in figure 2.9. In a VRFB different vanadium species (the anolyte consists of the pair V^{2+}, V^{3+} and the catholyte of VO^{2+}, VO_2^+) are dissolved in 4 M H_2SO_4 in order to stabilize vanadium concentrations up to 1.6 M. The electrode reactions for such a VRFB during discharge are:



When neither SO_4^{2-} , HSO_4^- , or H^+ cross the membrane for charge balance, but a redox active species, the resulting side reactions (e.g. $V^{3+} + VO_2^+ \longrightarrow 2VO^{2+}$) decrease the capacity of the battery. Thus, the coulombic efficiency (CE) is directly reduced. It represents the ratio of the charge that is retrieved from the battery during discharging to

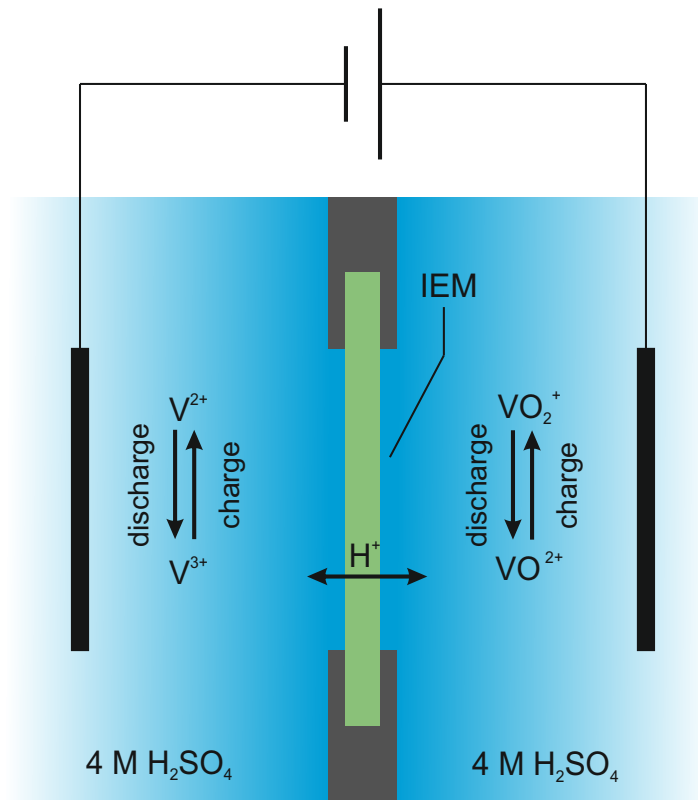


Figure 2.9: Scheme of a vanadium redox flow battery. The IEM as separator needs to transport protons (alternatively HSO_4^- or SO_4^{2-}) for the charge balance while keeping the redox active vanadium species in their respective compartment.

the charge that enters the battery during charging. A common practice to measure the CE is to charge and discharge the VRFBs to designated cutoff voltages and record the corresponding charging and discharging times t_c and t_d for each cycle. The charging and discharging times are then used to determine CE with

$$CE = \frac{\int_0^{t_d} I_d dt}{\int_0^{t_c} I_c dt} \quad (2.18)$$

where I_d is the discharging current and I_c is the charging current. Usually the currents are held constant and identical for both charging and discharging, i.e. $I_d = I_c$. In this specific case, it is:

$$CE = \frac{t_d}{t_c} \quad (2.19)$$

Additional to the self discharge losses by vanadium species crossing the membrane, electrical resistance losses occur, too. This phenomenon is described by the voltage

efficiency (VE), determined by the ratio of the average discharge voltage V_d to the average charge voltage V_c :

$$VE = \frac{t_d^{-1} \cdot \int_0^{t_d} V_d dt}{t_c^{-1} \cdot \int_0^{t_c} V_c dt} \quad (2.20)$$

The resulting energy efficiency (EE) is:

$$EE = CE \cdot VE \quad (2.21)$$

Chapter 3

Theoretical background

This work is focusing on ion partitioning and mobility as key parameters for selective transport of ionic species through membranes. Ion partitioning, is determined by the Donnan equilibrium, which in turn depends on the activity coefficients of the involved ions. Therefore, both theories, the Donnan equilibrium and the concept of activity coefficients are briefly introduced in chapter 3.1 and 3.2. Ion mobility on the other hand is predominantly affected by the membrane's morphology (besides immobilization by site binding). The current understanding of the morphology of IEMs, especially of the most prominent representative Nafion, is discussed in chapter 3.3.

3.1 Donnan equilibrium

An ion exchange membrane consists of an organic or inorganic framework (this work is limited to organic polymer backbones) bearing fixed ionic groups. The charge of these immobile fixed-ions is compensated by mobile counter-ions. CEMs have fixed anionic groups (e.g. sulfonic acid) and conduct cations, while AEMs have fixed cationic groups (e.g. quaternized ammonium) and conduct anions. When brought in contact with an electrolyte, the mobile counter-ions of the IEM can exchange with the ions from the electrolyte. In 1911, Donnan [27] was the first to describe the applicability of thermodynamic relations to systems of restrictedly exchanging ions of two separated phases, precisising it several years later [28]. In consequence it is called Donnan-equilibrium and the resulting potential between the aqueous phase in the IEM and the adjacent solution is referred to as Donnan potential ϕ_{Donnan} . The electrochemical potential of component i in a system η_i is defined as:

$$\eta_i = \mu_i^0 + RT \ln a_i + (p - p^0)v_i + z_i F \phi \quad (3.1)$$

where μ_i^0 is the standard chemical potential, R the gas constant, T the temperature, a_i the activity, p the pressure, p^0 the standard pressure, v_i the partial molar volume, z_i the charge number, F the Faraday constant, and ϕ the electric potential. For an electrolyte, consisting of the same ions as the membrane's mobile ions (referred to by the subscript counter) and of ions of the opposite charge, i.e. the same charge as the membrane's fixed ionic group (referred to by the subscript co) dissolved in a solvent (here water; referred to by the subscript w), the relevant electrochemical potentials are according to equation (3.1):

$$\eta_{\text{counter}} = \mu_{\text{counter}}^0 + RT \ln a_{\text{counter}} + (p - p^0)v_{\text{counter}} + z_{\text{counter}} F \phi \quad (3.2a)$$

$$\eta_{\text{co}} = \mu_{\text{co}}^0 + RT \ln a_{\text{co}} + (p - p^0)v_{\text{co}} + z_{\text{co}} F \phi \quad (3.2b)$$

$$\eta_{\text{w}} = \mu_{\text{w}}^0 + RT \ln a_{\text{w}} + (p - p^0)v_{\text{w}} + 0 \quad (3.2c)$$

These equations are valid for both the solution phase (referred to by the superscript sol) and the membrane phase (referred to by the superscript mem). In equilibrium, it holds:

$$\eta_i^{\text{sol}} = \eta_i^{\text{mem}} \quad (3.3)$$

Equation (3.3) represents the concept of the Donnan equilibrium and together with equation (3.2c) for the the pressure difference between both phases Π (osmotic pressure or swelling pressure) results:

$$\Pi = p^{\text{mem}} - p^{\text{sol}} = \frac{RT}{v_w} \ln \frac{a_w^{\text{sol}}}{a_w^{\text{mem}}} \quad (3.4)$$

In general, the influence of the swelling pressure on the chemical potential of the ions is rather small compared to the concentration effects and will be neglected from now on ($\Pi = 0$). For an intuitive example calculation see [29]. From equation (3.3) and equation (3.2a), respectively (3.2b), the Donnan potential difference between both phases ϕ_{Donnan} can be derived:

$$\phi_{\text{Donnan}} = \phi_i^{\text{mem}} - \phi_i^{\text{sol}} = \frac{1}{z_i F} \left(RT \ln \frac{a_i^{\text{sol}}}{a_i^{\text{mem}}} \right) \quad (3.5)$$

For an 1,1 electrolyte, from equation (3.5), which is valid for co- and counter-ions, the result is:

$$a_{\text{counter}}^{\text{sol}} \cdot a_{\text{co}}^{\text{sol}} = a_{\text{counter}}^{\text{mem}} \cdot a_{\text{co}}^{\text{mem}} \quad (3.6a)$$

which can be written as

$$\left(\gamma_{\pm}^{\text{sol}} \right)^2 \cdot b_{\text{counter}}^{\text{sol}} \cdot b_{\text{co}}^{\text{sol}} = \left(\gamma_{\pm}^{\text{mem}} \right)^2 \cdot b_{\text{counter}}^{\text{mem}} \cdot b_{\text{co}}^{\text{mem}} \quad (3.6b)$$

with γ_{\pm} being the mean activity coefficient and b the molality. To make predictive statements about the ion uptake of a IEM in equilibrium, also the condition of electroneutrality needs to be included:

$$b_{\text{fixed}} + b_{\text{co}}^{\text{mem}} = b_{\text{counter}}^{\text{mem}} \quad (3.7)$$

with b_{fixed} being the molality of fixed-ions in the membrane. Solving the equation system of equation (3.6a) and (3.7) leads to equations for the counter- and co-ion uptake of the IEM:

$$b_{\text{counter}}^{\text{mem}} = \frac{1}{2} \left(\sqrt{b_{\text{fixed}}^2 + 4 \cdot \left(\frac{\gamma_{\pm}^{\text{sol}}}{\gamma_{\pm}^{\text{mem}}} b^{\text{sol}} \right)^2} + b_{\text{fixed}} \right) \quad (3.8a)$$

$$b_{\text{co}}^{\text{mem}} = \frac{1}{2} \left(\sqrt{b_{\text{fixed}}^2 + 4 \cdot \left(\frac{\gamma_{\pm}^{\text{sol}}}{\gamma_{\pm}^{\text{mem}}} b^{\text{sol}} \right)^2} - b_{\text{fixed}} \right) \quad (3.8b)$$

with $b^{\text{sol}} = b_{\text{counter}}^{\text{sol}} = b_{\text{co}}^{\text{sol}}$ being the molality of the 1,1 electrolyte adjacent to the membrane. For a quantitative prediction of the ion uptake the knowledge of the activity coefficients is required. In a first approximation the activity coefficients within the membrane can be assumed to be the same as in the external solution. Then, equations (3.8) simplify to the so called ideal Donnan equation:

$$b_{\text{counter}}^{\text{mem}} = \frac{1}{2} \left(\sqrt{b_{\text{fixed}}^2 + 4 \cdot (b^{\text{sol}})^2} + b_{\text{fixed}} \right) \quad (3.9a)$$

$$b_{\text{co}}^{\text{mem}} = \frac{1}{2} \left(\sqrt{b_{\text{fixed}}^2 + 4 \cdot (b^{\text{sol}})^2} - b_{\text{fixed}} \right) \quad (3.9b)$$

As long as the concentration of the external solution b^{sol} is low compared to the concentration of fixed-ions in the membrane b_{fixed} , co-ions are prevented from entering the membrane. When the ion concentration of the external solution approaches concentrations in the range of the fixed-ion concentration in the membrane, co-ions together with the equivalent amount of counter-ions enter the membrane (breakdown of the Donnan exclusion). A measure for the extent of the Donnan exclusion is the mole fraction x of mobile ions in the membrane. When perfect Donnan exclusion holds true, the mole fraction of counter-ions

$$x_{\text{counter}}^{\text{mem}} = \frac{b_{\text{counter}}^{\text{mem}}}{b_{\text{counter}}^{\text{mem}} + b_{\text{co}}^{\text{mem}}} \quad (3.10)$$

is virtually 1, diverging slowly towards 0.5 for increasing external electrolyte concentration (see fig. 3.1). Here, when the breakthrough of co-ions exceeds 10% of the mobile ions, it is considered as the breakdown of Donnan exclusion.¹ In Figure 3.1 the transition from Donnan exclusion regime to the breakdown regime as a function of external electrolyte concentration is shown for different fixed-ion concentrations. The mole fraction of counter-ions within all mobile ions in the membrane $x_{\text{counter}}^{\text{mem}}$ may serve as estimation for the transference number. Typically, for an IEM not the molality of the fixed-ions b_{fixed} is used, but the number of water molecules per fixed-ion:

$$\lambda = \frac{1000}{b_{\text{fixed}} \cdot 0.018 \text{ kg mol}^{-1}} \quad (3.11)$$

The Donnan equilibrium is the foundation of the theory of Teroell, Meyer and Sievers (TMS theory), which successfully described transport phenomena in IEMs for the first

¹Since no exact definition exists in literature, this limit is eventually chosen discretionary.

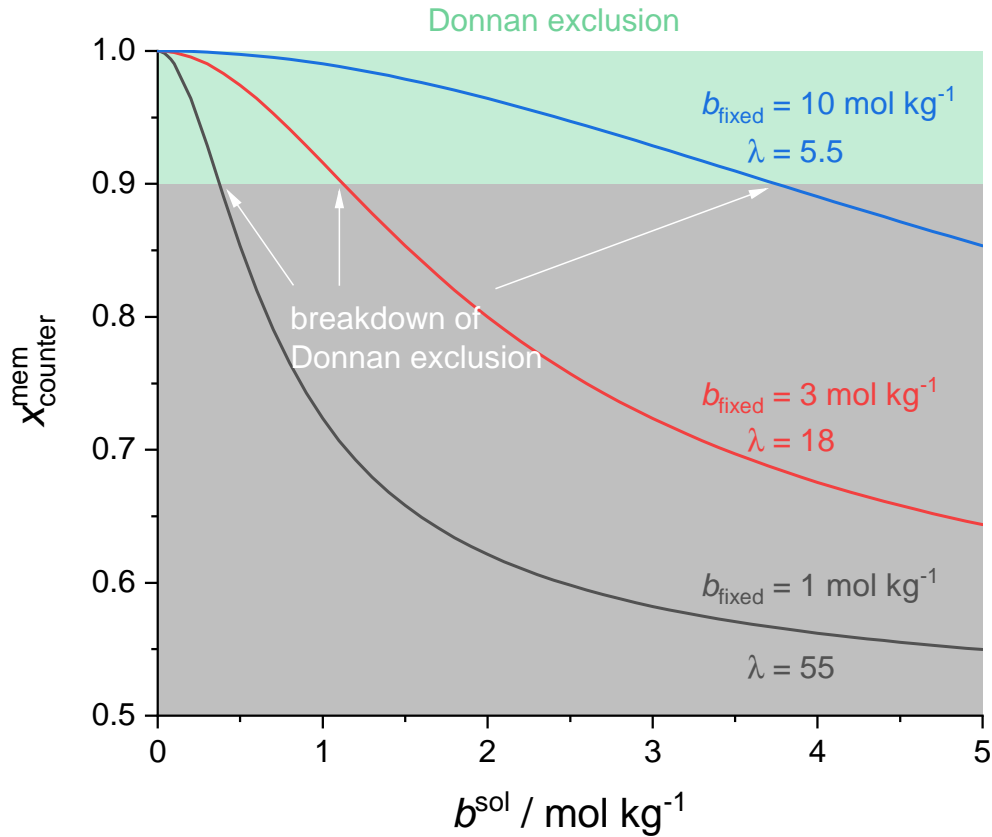


Figure 3.1: Mole fraction of counter-ions in an IEM as a function of the molality of an adjacent 1,1 electrolyte for different fixed-ion concentrations.

time [30,31]. The TMS theory extends the ion partitioning of the Donnan equilibrium by the Nernst-Planck equation

$$J = -D \cdot \left(\nabla c + \frac{zF}{RT} c \nabla \phi \right) \quad (3.12)$$

where J is the ionic flux density.

The TMS theory allows for making statements about transference numbers of ion transport through IEMs.

3.2 Activity coefficients

In general, the activity of an ion in a solution is not just its molality. The reason lies in the interactions of the ions with themselves, other ions and the solvent. In dilute solutions it is predominantly the Coulomb interactions which are responsible for the deviation of the activity from the molality. In 1923, Debye and Hückel [32] developed a theory describing this discrepancy. As oppositely charged ions attract each other, from a viewpoint of a given ion, ions are not distributed equally in a solution. The solution is electrically neutral overall, there is only an excess of oppositely charged ions in the local environment of a certain ion on average over time. This spherically symmetric volume element, which surrounds a central ion and in which there are more counter-ions than ions of the same charge on a time average, is called an ion cloud. The total charge of the ion cloud is on average opposite to the charge of the central ion and the chemical potential is determined by the electrostatic interaction with the ion cloud is reduced. From this model the Debye-Hückel limiting law (for molalities up to 0.01 mol kg^{-1}) follows:

$$\log_{10} \gamma_{\pm} = -A|z_+z_-|\sqrt{I} \quad (3.13)$$

where I is the ionic strength $I = \frac{1}{2} \sum_i z_i^2 b_i$ and $A = 0.509 \sqrt{\frac{\text{kg}}{\text{mol}}}$, derived from the Poisson equation and the Boltzmann distribution. For molalities up to 0.01 mol kg^{-1} , the extended Debye-Hückel theory is valid:

$$\log_{10} \gamma_{\pm} = -\frac{A|z_+z_-|\sqrt{I}}{1 + B\sqrt{I}} + CI \quad (3.14)$$

The parameters B and C should be treated as empirical parameters, where B may be physically interpreted as shortest distance between two ions. Deviations from these equations occur due to the model's oversimplifications, such that ions are not necessarily spherical and may be polarizable. Davies [33] extended the Debye-Hückel theory considering incomplete dissociation of weak electrolytes. Ion association is considered to take place when the ion-ion distance is below the Bjerrum length at which the electrostatic interaction between two ions is comparable in magnitude to kT [34]. Also, the role of solvent is not appreciably accounted for in the theory above. At higher molalities, not only the reduced dielectric constant ϵ affects the Debye length and thereby

the parameter A , solvent-ion interactions have a direct effect on activity coefficients. Stokes [35] suggested in 1948 that the ions may bind solvent molecules in their solvation shell, i.e. reduce the amount of solvent and increase the effective molality. This "hydration correction to the activity coefficient" [35] is used later in this work. However, most modern approaches use indirect methods to determine the activity coefficients using the Gibbs-Duhem equation:

$$\sum_i n_i d\mu_i = -SdT + Vdp \quad (3.15)$$

They first establish a theory for the dependence of the solvent activity coefficient on the solute concentration and then calculate the activity coefficient of the dissolved species with the equation above (3.15).

3.3 Morphology of IEMs

The morphology of IEMs has been subject of controversies for the last decades. The CEM Nafion in particular has attracted attention because of its wide use in electrochemical applications. The cluster model, where short narrow channels connect spherical aqueous domains [36], a fibrillar (bundle) model [37], and the parallel cylinder model [38] were developed from correlation lengths, obtained from the position of the ionomer peak of SAXS data. The most sophisticated evaluation of this data until 2008 [38], which is strongly in favor of the parallel cylinder model, unfortunately lacks correct data on the membrane's water content [39]. Later, in 2013, measurements of the correlation length of Nafion as a function of water content revealed a linear dependency of the correlation length and the water volume fraction [39]. This one-dimensional swelling supports the idea of locally flat water domains (see fig. 3.2). In flat structures the accumulation of positively charged ions is reduced compared to cylinders, lowering electrostatic energy and facilitating the formation of ionic cross-links, thereby driving the rearrangement of the morphology. Furthermore, the model allows for an easy calculation of the aqueous domain width d_{aq} from the correlation length d :

$$d_{\text{aq}} = d \cdot \frac{V_{\text{aq}}}{V_{\text{aq}} + V_{\text{poly}}} \quad (3.16)$$

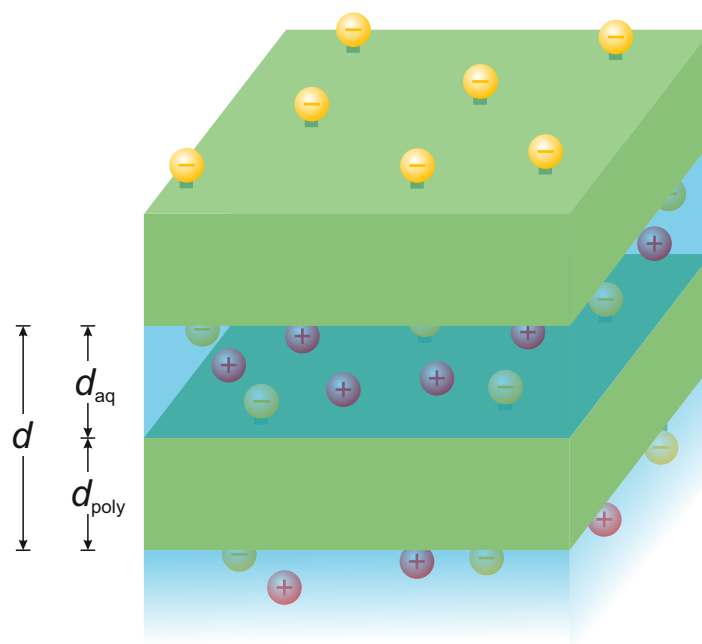


Figure 3.2: Illustrated model of the locally flat morphology of Nafion. The polymeric, hydrophobic part is green with attached fixed-ions (yellow) directing towards the aqueous domain (blue, transparent), containing the counter-ions (red). The correlation length d is marked, divided into the corresponding aqueous and polymeric phase, d_{aq} and d_{poly} .

where V_{aq} and V_{poly} are the volume fractions of the aqueous ionic domain and the polymeric domain, respectively. On larger scales these flat water films show high tortuosity, which could be shown in 2015 by cryogenic transmission electron microscopy tomography [40]. When compared to Nafion, hydrocarbon membranes, such as sPEEK, show a different microstructure. For a hydrocarbon membrane compared to Nafion the ionomer peak is broadened and shifted towards higher scattering angles [16]. Additionally, the intensity in the Porod regime of hydrocarbon membranes' SAXS patterns is higher, expressing the larger surface-to-volume ratio (see chapter 2.6). Together, this indicates a smaller characteristic separation length with a wider distribution and a larger internal interface between the hydrophobic and hydrophilic domain for the hydrocarbon membrane (see fig. 3.3). The difference stems from the fact, that the unpolar fluorinated backbone of Nafion as a PFSA is extremely hydrophobic and tends towards stronger aggregation. The polymer backbone of hydrocarbons, on the other hand, is less hydrophobic and less flexible, which leads to a less pronounced hydrophilic /

hydrophobic phase separation. The resulting high internal surface area between these domains for hydrocarbons implies a higher average distance of functional groups compared to Nafion.

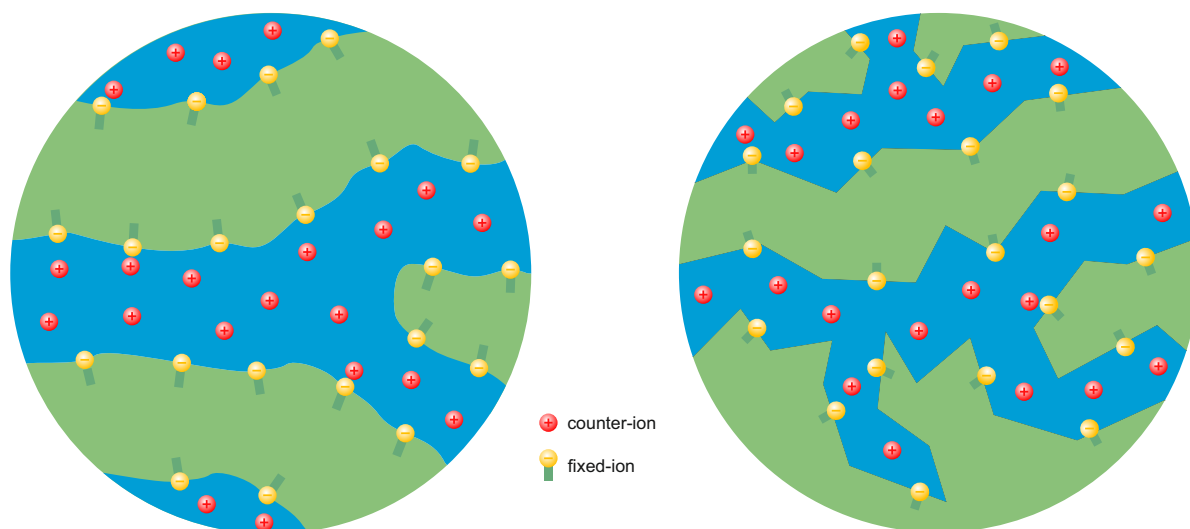


Figure 3.3: Schematic representation of the microstructures of Nafion (left) and a hydrocarbon membrane (right). The less pronounced hydrophobic (green) / hydrophilic (blue) separation of hydrocarbon membranes corresponds to narrower, less connected hydrophilic domains and to larger separations between sulfonic acid functional groups.

Chapter 4

Results and discussion

Data on selective ion transport are discussed in terms of ion partitioning and ion mobility within the different ion exchange membranes (IEMs).

In chapter 4.1, emphasis is laid on the specific interactions of ions with the fixed ionic groups of IEMs. Relatively small ions with valence +1 or -1 in well hydrated IEMs are used to exclude other effects as far as possible.

In chapter 4.2, the effect of the absolute value of an ion's valency on the ion partitioning between an IEM with its surrounding electrolyte solution is studied.

Finally, in chapter 4.3, morphological effects of IEMs on ion mobility are examined.

4.1 Specific interactions

In order to separate the effect of chemical interaction between fixed ionic groups and different counter-ions from other effects, results for the partitioning of counter-ions (Li^+ and Cs^+) between dissolved ionomers and their aqueous environment are discussed first (see chapter 4.1.1). Then, trends are verified for well swollen membranes (chapter 4.1.2) and quantitatively discussed for Nafion (chapter 4.1.3). Li^+ and Cs^+ have been chosen as extreme representatives of small, hard cations with high charge density and large, soft ions with delocalized charge respectively. In addition, their isotopes ^7Li and ^{133}Cs allow measuring their tracer diffusion coefficient by the pulsed magnetic field gradient NMR technique [41].

4.1.1 Selective ion transport in dissolved ionomers

For dissolved ionomers neither morphological effects nor counter-ion condensation apply. The latter phenomenon is described by Manning's theory [42], which assumes that counter-ions condense onto polyions if the distance between neighboring charges along a polyion chain is below a certain critical value. This value is the so-called Bjerrum length λ_B , the separation at which the electrostatic interaction between two elementary charges is comparable in magnitude to the thermal energy:

$$\lambda_B = \frac{e^2}{4\pi\epsilon_r\epsilon_0k_B T} \quad (4.1)$$

While the Bjerrum length in water is 0.7 nm (for $\epsilon_r = 78$), for example the average intrachain distance of functional groups in perfluorosulfonic acids as Nafion is around 2 nm [43].¹ Hence, no counter-ion condensation is expected for dissolved ionomers with "stretched" conformations, because the charge distance within the polymer is well above the the Bjerrum length.

In this work, different dissolved ionomers with fixed anionic groups are investigated in terms of selective ion uptake by keeping them in a dialysis tube only permeable for molecules with a lower molecular mass than 3.5 kDa (see figure 4.1). The fol-

¹For Nafion in membrane form, the average distance of charges reduces to 0.9 nm as the sulfonic acid groups aggregate on the surface of the polymeric phase [39].

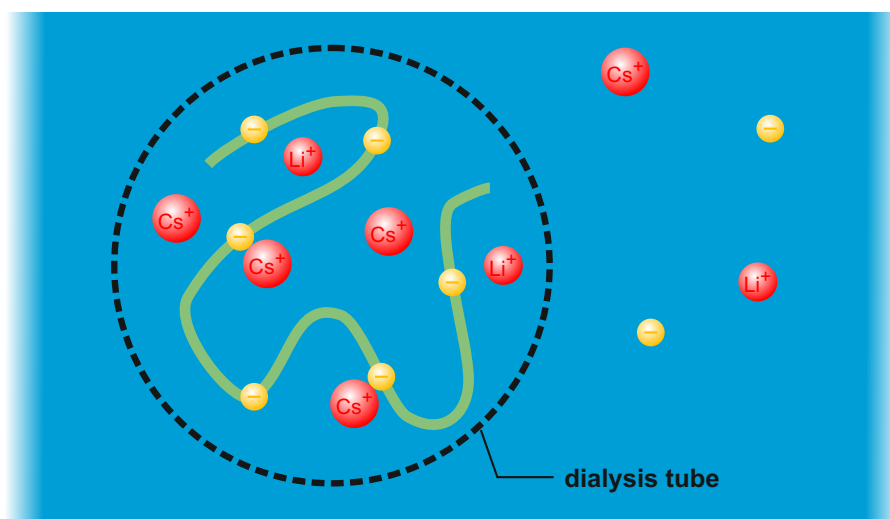


Figure 4.1: Scheme of the experimental setup for measuring ion partitioning of dissolved ionomers. The dashed line represents the dialysis tube hosting the dissolved ionomer (green line as polymer chain with the yellow fixed ionic groups). The counter-ions Li^+ and Cs^+ (depicted in red) are present in a 1:1 ratio in the external solution.

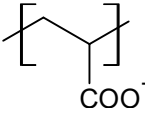
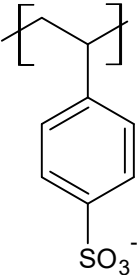
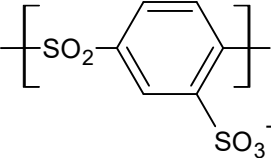
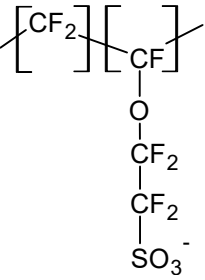
lowing ionomers in descending order of acidity were studied: Aquivion D72, sulfonated poly(phenylene sulfone) sPSO2-220, fully sulfonated polystyrene (PSS), and poly(acrylic acid) (PAA). While the latter exhibits weak carboxylic acid groups ($\text{pK}_a \approx 4$), the first three share the same functional group, the sulfonic acid group, which is attached to different electron withdrawing polymer backbones. The highly electronegative fluorine atoms of Aquivion for example cause a very low pK_a of the sulfonic acid group of about -6 [16] making it a "super acid". The electron withdrawing sulfonic group in sPSO2 is increasing the acid strength of the sulfonic acid group, too, even though to a smaller extent.

For the ion partitioning measurement, the ionomers were dissolved with a concentration of $\lambda \sim 100$ to 120 (which refers to $c \approx 0.5 \text{ M}$) and equilibrated in an aqueous solution of $\text{LiCl} / \text{CsCl}$ of the ratio 1:1. The concentration of the solution was subsequently diluted starting from an initial concentration of 0.1 M . The ionomer was kept within a dialysis membrane with a 3.5 kDa molecular weight cut-off (MWCO), i.e. only counter-ions (Li^+ and Cs^+) could be exchanged while the charged polymers remained inside the volume defined by the dialysis tube². Of course, water molecules may also

²all occurring average molecular weights M_w are well above the dialysis tube's MWCO: see table 4.1

enter the inner of the tube diluting the ionomer concentration, because of the osmotic pressure. However, the volume increase was estimated to be less than by a factor of 2. Due to the gradual dilution of the external solution electrolyte uptake (uptake of Li^+ or Cs^+ together with the co-ion Cl^-) can be neglected because of Donnan exclusion. The resulting counter-ion partitioning of Li^+ and Cs^+ within the phase of the dissolved ionomer was measured via elemental analysis. The data obtained from ICP OES are listed in table 4.1.

Table 4.1: Partitioning data of dissolved ionomers sorted by acid strength in a 1:1 $\text{Li}^+:\text{Cs}^+$ external solution. Additional information about the chemical structure and the polymer's average molecular weight M_w is provided.

	PAA	PSS	sPSO2-220	Aquivion
formula				
M_w	250 kDa	75 kDa	65 kDa	>100 kDa
acidity	low	high		"super acidic"
ratio Li:Cs	56 : 44	36 : 64	32 : 68	28 : 72

The parameter controlling ion partitioning appears to be the acidity pK_a of the fixed ionic group, i.e. increasing acidity leads to a relative stabilization of Cs^+ compared to Li^+ as a counter-ion compensating for the charge of the conjugated base ($-\text{SO}_3^-$ or $-\text{COO}^-$), which is expressed in the fact that the $\text{Li}^+ : \text{Cs}^+$ ratio decreases from 56 : 44 for the weak acidic PAA to 28 : 72 for the super acidic Aquivion. This actually might be expected considering the lower electronegativity of the large polarizable Cs^+ compared to the small hard Li^+ and the fact that the electronegativity of the conjugated base increases with the acidity of the corresponding acid. For PAA the partitioning is still slightly in favor of Li^+ , an ion similar to the hard ion H^+ which hardly dissociates in case of weak acids. However, with increasing acidity, the binding interaction of the

fixed ionic group to Cs^+ is expected to develop some covalency while with Li^+ the interactions remains essentially ionic. In terms of specific chemical interactions, this corresponds to the extreme case of a cation (here Cs^+) donating some electron density to the super acidic anion ($-\text{SO}_3^-$).

The resulting counter-ion binding to the fixed ionic group should not be confused with the commonly known Manning counter-ion condensation [42] which is a pure electrostatic effect expected to be identical for any monovalent cation provided dielectric constants of the solvent are identical. As mentioned above, for ruling this out, dissolved ionomers were used with an average charge distance larger than the Bjerrum length. The present observation that dissolved or highly swollen ionomers with an average charge distance larger than the Bjerrum length localize Li^+ and Cs^+ to a clearly different extent (see table 4.1) suggests that this is not controlled by electrostatics. It should also be mentioned that binding of the counter-ion to the fixed ionic group competes with ion hydration which is more exothermic for Li^+ compared to Cs^+ . The latter favors Li^+ over Cs^+ dissociation for all three ionomers. Especially, Pintauro et al. have modeled the effect fixed-ions have on the orientation of water and how this affects the solvation of the diverse counter-ions [44, 45]. These purely electrostatic considerations alone qualitatively yield the right trends with respect to ion partitioning (these authors have also picked Li^+ and Cs^+ as counter-ions), but such models miss the effects which the fixed ion's acidity has on counter-ion localization.

If ion association occurs, it will have an immediate effect on the ion mobility. In order to check the viability of this implication the diffusion coefficients of Li^+ and Cs^+ were measured by PFG NMR (see chapter 2.5.2). For better comparability all dissolved ionomers from above were adjusted to $\lambda = 120$ and a $\text{Li}^+ : \text{Cs}^+$ ratio of 1 : 1 by adding an equimolar amount of a 1 : 1 mixture of Li_2CO_3 and Cs_2CO_3 to the H^+ form of the respective ionomer (Li^+ and Cs^+ are replacing H^+ , which reacts to H_2O , and the produced CO_2 is removed). Under the conditions of the present experiment, i.e. very dilute ionomer concentration, ^7Li and ^{133}Cs NMR lines show a single component only. Obviously, there is sufficient exchange between bound co-ions and co-ions which are weakly localized within the diffuse space charge layer charge-compensating for the residual charge of the partially neutralized fixed-ions. NMR diffusimetry with these

signals then yield the space/time averaged tracer diffusion coefficients of Li^+ and Cs^+ . The measured data are shown in figure 4.2 together with ratio $D_{\text{Cs}^+}/D_{\text{Li}^+}$. For reference, this ratio for a dilute aqueous solution is also given. The corresponding values are accessible in equivalent conductivity tables in literature [14].

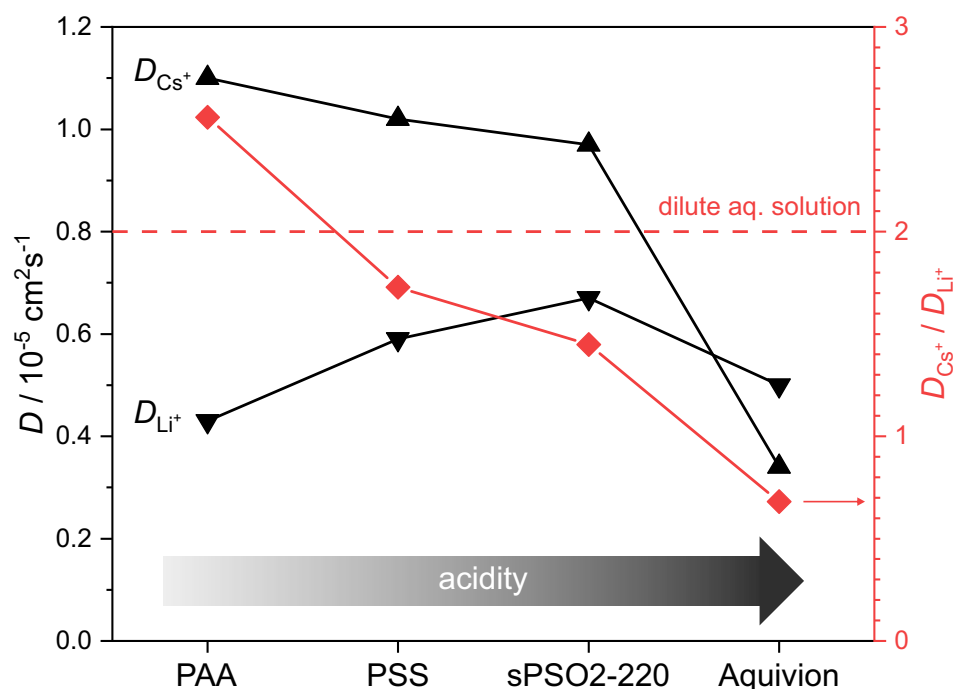


Figure 4.2: Average Li^+ and Cs^+ diffusion coefficients (black downward triangles, respectively upward) and their ratio (red diamonds), measured by ^7Li and ^{133}Cs PFG NMR, of dissolved ionomers at $\lambda = 120$ of different acidity with Li^+ and Cs^+ as counter-ions in the molar ratio 1 : 1. The ratio of diffusion coefficients in a infinite dilute aqueous solution is drawn as dashed red line. Note that D_{Cs^+} continuously decreases with increasing acidity of the fixed ionic group indicating increasing degree of counter-ion binding to the fixed ionic group. For Li^+ , however, the trend is reversed with an exception for Aquivion (therefore, see explanation in text).

With increasing acidity, Cs^+ diffusion is progressively retarded as a consequence of increasing specific (covalent) interaction with the fixed ionic group. For Li^+ , however, the diffusion coefficient increases with acidity from PAA over sulfonated polystyrene PSS to the very acidic sulfonated poly(phenylene sulfone) sPSO2-220, which simply indicates an increasing degree of dissociation with increasing acidity. In other words, the behavior of the small hard heavily hydrated Li^+ is closer to that of the proton (H^+) which cannot shift electron density to its conjugated base. For super acidic Aquivion,

however, the diffusion coefficient of Li^+ is slightly retarded against this trend indicating the onset of specific binding to the conjugated base ($-\text{SO}_3^-$) also for Li^+ . Another possible explanation is, that Aquivion with the alkali counter-ions is not a real solution anymore, as experimentally, a gelation-like behaviour was observed when the carbonates were added, i.e. all mobilities are retarded to some extent shifting the diffusion coefficients to lower values. Nevertheless, the trend of the decreasing $D_{\text{Cs}^+}/D_{\text{Li}^+}$ ratio with increasing acid strength is maintained. Considering this mobility ratio for Cs^+ and Li^+ the highest value (2.54) is measured for the weak acid PAA (see figure 4.2). This is almost 30 % higher than for the aqueous solution (2.00), essentially reflecting the slightly weaker dissociation of Li^+ compared to Cs^+ (ionic behavior). With increasing acidity the increasing association of the Cs^+ to the fixed ionic group through covalent interaction leads to a drastic decrease of this ratio to $D_{\text{Cs}^+}/D_{\text{Li}^+} = 0.68$ observed for Aquivion.

The measured diffusion coefficients can be used together with the partitioning data to determine the relative contribution to the total conductivity. This estimation for the transference number t_i is:

$$t_i = \frac{x_i D_i}{\sum x_i D_i} \quad (4.2)$$

which holds when all counter-ions i of the mole fraction x_i move independently within the ionomer solution. It has to be mentioned, that the mobility data was measured for a 1 : 1 ratio of Li^+ and Cs^+ counter-ions in the ionomer solution, while the composition in the equilibrated samples was different, i.e. the transference numbers in table 4.2 are just estimations.

Although the stronger acidic ionomers preferentially take up Cs^+ , the transference number t_{Cs^+} only slightly increases from 0.67 for an aqueous solution of LiCl/CsCl (1:1) to 0.75 for PSS and sPSO2-220. For Aquivion however, where the uptake of Cs^+ is pronounced the most, the calculated transference number is even reduced to 0.64, although not significantly. The severe difference of Li^+ and Cs^+ uptake appears to be compensated by the corresponding retardation of ion mobility leaving the transference numbers almost unchanged. This is in-line with the existing literature, that observes Nafion's distinct ion partitioning but is not able to demonstrate the same trend in terms of selective transport [45, 46]. Concerning the transport/selectivity relationships, the

Table 4.2: Estimated transference numbers of Li^+ and Cs^+ in dissolved ionomers equilibrated in a 1:1 solution of Li^+ and Cs^+ . For comparison the transference numbers in a infinite dilute aqueous solution is given. The data is a result of the combination of partitioning and mobility data (from table 4.1 and figure 4.2).

	PAA	PSS	sPSO2-220	Aquivion	aq. solution
x_{Li^+}	0.44	0.36	0.32	0.28	0.50
x_{Cs^+}	0.56	0.64	0.68	0.72	0.50
$D_{\text{Li}^+}/10^{-5}\text{cm}^2\text{s}^{-1}$	0.43	0.59	0.67	0.50	1.03
$D_{\text{Cs}^+}/10^{-5}\text{cm}^2\text{s}^{-1}$	1.09	1.02	0.97	0.34	2.06
$\sim t_{\text{Li}^+}$	0.33	0.25	0.25	0.36	0.33
$\sim t_{\text{Cs}^+}$	0.67	0.75	0.75	0.64	0.67

total value of the diffusion coefficients (i.e. ionic conductivity) even decreases against an aqueous solution without gaining any selectivity for ionic transport.

4.1.2 Ion partitioning in membranes: validating the role of acidity

As next complication, true membranes with a low enough IEC preventing them from exaggerated swelling or dissolution are considered. For the analysis, the following membranes are resorted to: the benchmark membrane Nafion (a PFSA as Aquivion), a low IEC sulfonated poly(phenylene sulfone) sPSO2-360, and FKE-50 from fumatech GmbH, a sulfonated polyether ketone (sPEEK).

In the case of Nafion, there already exists a data set in literature [46], which is consistent with the data of this work. In figure 4.3 the Li^+/Cs^+ partitioning data between dilute aqueous solutions containing LiCl/CsCl and Nafion is plotted as a function of the mole fraction in solution. The preference for the Cs^+ uptake is even more pronounced for Nafion, than it is the case for dissolved Aquivion. For a 1:1 ratio in the external solution, the Li^+/Cs^+ ratio in Nafion is 12 : 88, while it is only 28 : 72 for Aquivion (see table 4.1). The measurements were performed by equilibrating the membrane pieces in <0.1 M solutions of LiCl/CsCl of the respective molar ratio. After washing

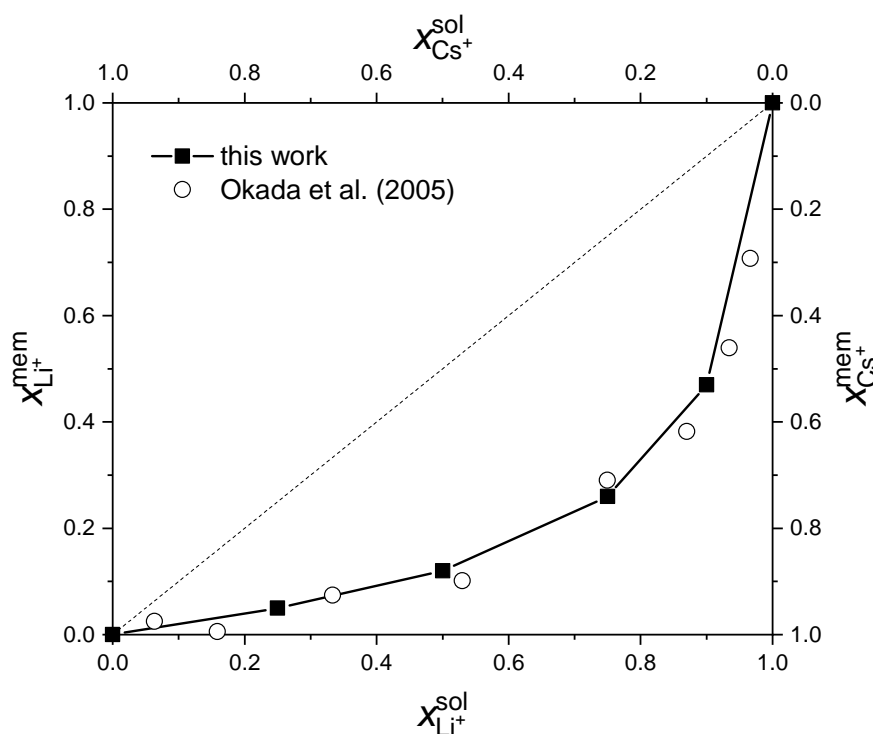


Figure 4.3: Li^+/Cs^+ partitioning between aqueous solutions containing LiCl and CsCl in different molar ratio (<0.1 M total) and Nafion. Data of this work is consistent with literature [46]. The statistical errors are below 3 %.

in demineralized water, the Li^+ and Cs^+ ions are retrieved from the membrane and measured with ICP OES (for more experimental details see appendix).

In order to verify the trend of partitioning depending on the acidity of the functional groups observed for the dissolved ionomers, above mentioned membranes with less acidic groups than Nafion are added to the data set from figure 4.3. With its electron withdrawing sulfone groups, sPSO2-360 is a little bit less acidic than the super acidic PFSA Nafion. The fumapem FKE-50 membrane as a representative of sPEEKs is bearing ether groups which cause a decreased acidity because of the mesomeric effect (here the electron releasing +M-effect) compared to sPSO2. In figure 4.4 the partitioning data of these membranes is shown together with the data of dissolved ionomers for a external solution with a 1 : 1 Li^+/Cs^+ ratio ($x_{\text{Li}^+}^{\text{sol}} = x_{\text{Cs}^+}^{\text{sol}} = 0.5$). As for the very dilute case, the selective uptake of Cs^+ vs. Li^+ increases with acidity of the fixed ionic group, and one may therefore wonder whether specific interactions between counter-ions and fixed-ionic groups suggested above for solutions are still the key parameter controlling ion

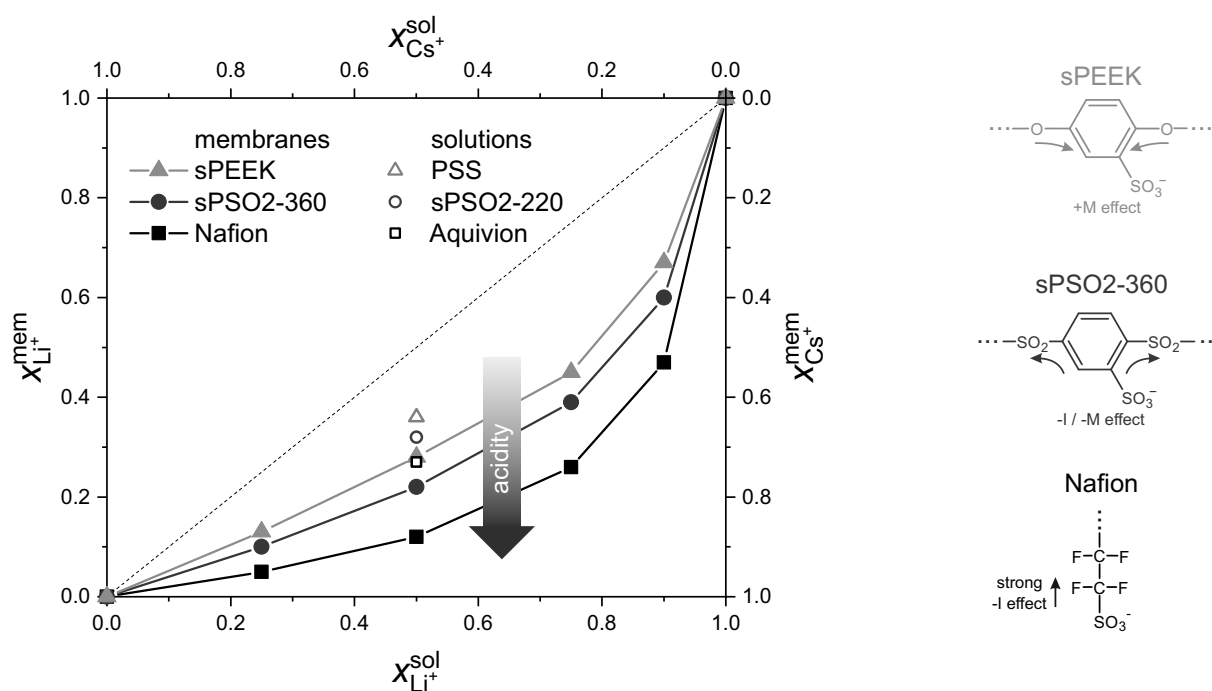


Figure 4.4: Li^+/Cs^+ partitioning between aqueous solutions containing LiCl and CsCl in different molar ratio ($<0.1\text{ M}$ total) and membranes of different acid strength. Data of dissolved ionomer from table 4.1 is included. The statistical errors are below 3 %.

partitioning for membranes. In general the partitioning is more pronounced for the membranes than for the dissolved ionomers. Nevertheless, the water content λ alone does not seem to be the dominating parameter: the water content of the membranes in proton form is

$$\text{sPEEK}(\lambda = 15) < \text{Nafion}(\lambda = 18) < \text{sPSO2-360}(\lambda = 28)$$

while the selectivity order follows the functional group's acidity $\text{sPEEK} < \text{sPSO2-360} < \text{Nafion}$. If electrostatics were responsible for the selectivity, the average distance between the fixed ionic groups would matter. This average distance depends on the IEC and the local morphology. Nafion, as a representative of PFSA, has a very distinct phase separation compared to hydrocarbon membranes like sPEEK or sPSO2. As described in chapter 3.3, a more pronounced separation results in larger internal surface area of the aqueous and the polymeric phase. The functional groups are distributed on this interface, i.e. the ion exchange capacity and the degree of separation both affect

the average distance of functional groups. In order to cover the two parameters, two membranes were chosen to be compared to Nafion:

- fumapem 1850: basically Nafion with a lower IEC
- BP-ArF4: a hydrocarbon membrane with the same volumetric IEC and super acidic functional groups as Nafion

The Li^+/Cs^+ partitioning of the membranes is shown in figure 4.5. The fumapem 1850

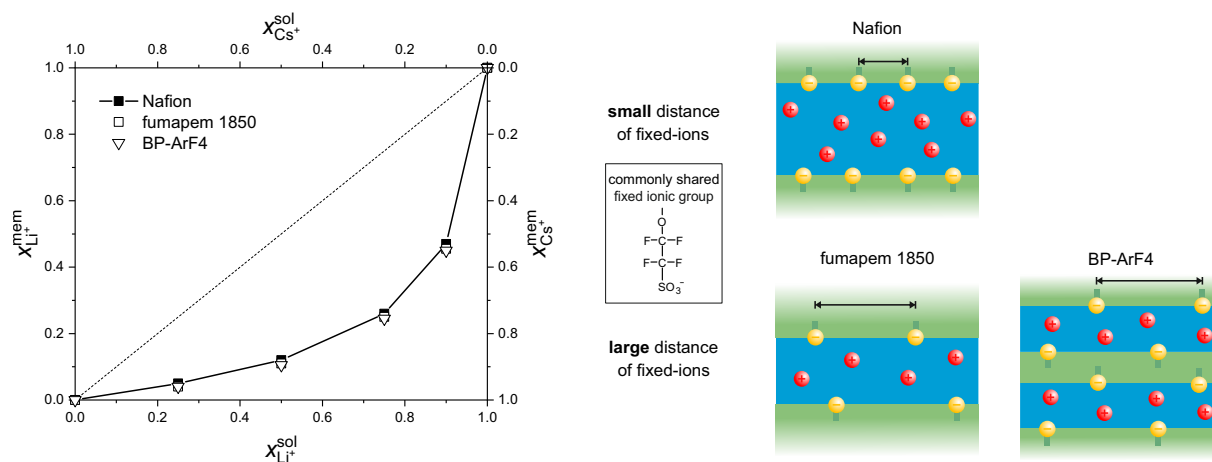


Figure 4.5: Li^+/Cs^+ partitioning between aqueous solutions containing LiCl and CsCl in different molar ratio (<0.1 M total) and membranes with functional groups of the same acid strength. Compared to Nafion, fumapem 1850 has lower IEC and BP-ArF4 has a hydrocarbon morphology. Consequently the latter two have a lower interfacial charge density, but still, they show virtually the same ion partitioning.

membrane is a long sidechain PFSA just like Nafion, but with less functional groups (the IEC is only 0.54 meq g^{-1} instead of 0.91 meq g^{-1} as it is for Nafion). The BP-ArF4 membrane with its hydrocarbon backbone shows a hydrophilic / hydrophobic phase separation typical for hydrocarbons (see experimental proof in chapter 4.3) but has at the same time a partly fluorinated side chain to which the sulfonic acid is attached. This way, the BP-ArF4 membrane bears functional groups with the same acidity as Nafion while exhibiting a hydrocarbon morphology. The IEC of BP-ArF4 is 1.4 meq g^{-1} and therefore higher than the one of Nafion, but in relation to their volume the concentrations of functional groups are almost the same: 1.96 meq cm^{-3} vs. 1.91 meq cm^{-3} .³ To

³ $\rho_{\text{Nafion}} = 2.1 \text{ g cm}^{-3}$; $\rho_{\text{BP-ArF4}} = 1.4 \text{ g cm}^{-3}$

summarize the relevant membrane specifications, the 3 membranes in figure 4.5 share the same acidity of their functional groups, but differ in the average distance of their functional groups on the aqueous / polymeric phase interface. In case of fumapem 1850, the deviation of this distance compared to Nafion is due to the lower IEC and in case of BP-ArF4 it is due to the hydrocarbon morphology (larger interface where the functional groups are distributed). Interestingly, according to the data in figure 4.5, the Li^+/Cs^+ partitioning is virtually the same for all 3 membranes. This underlines the proposition, that the acidity is really the key parameter controlling the ion partitioning. The subordinate effect of hydration will be discussed as a part of the following chapter 4.1.3.

4.1.3 Ion partitioning in Nafion: ion association

In the previous two chapters it is clearly demonstrated, that ion partitioning in CEMs depends on the acid strength of the membrane's functional group. The rational behind this phenomenon is suggested to be counter-ion association. A counter-ion association/dissociation equilibrium may approximately be described by two chemically distinct states: the fixed-ion/counter-ion pair and the hydrated counter-ion, which is mobile within the aqueous domain. The very early NMR work on Nafion of Komoroski and Mauritz already gave clear qualitative indication for such two states [47]. They observed chemical shifting and line broadening of the cation's NMR signal in membranes with reduced water content. In the present work, NMR relaxometry provides evidence for the existence of two states with different mobility, even quantitatively. In the case of a Nafion membrane in pure Li^+ form with $\lambda = 18$ a ^7Li spin-spin relaxation experiment (a Carr Purcell Meiboom Gill (CPMG) sequence) revealed two different species with different T_2 relaxation times (see figure 4.6). The shorter T_2 (3.3 ms) corresponds to a Li^+ ion with lower motion dynamics (see chapter 2.5.1), i.e. an associated species,

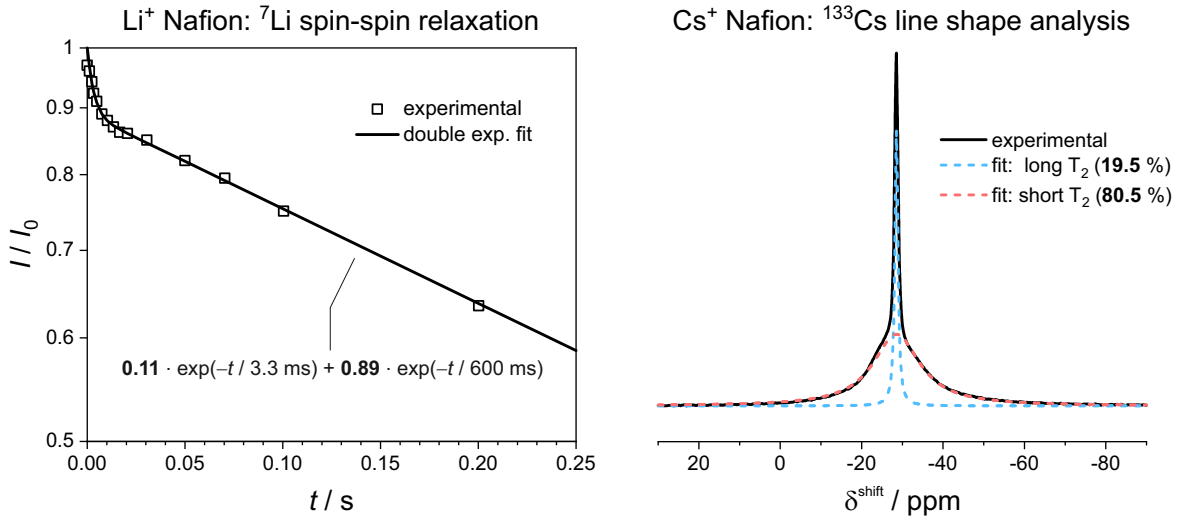
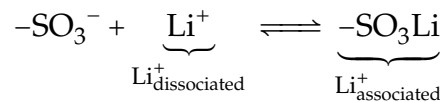


Figure 4.6: Experimental NMR data showing evidence of counter-ion association. Left: ⁷Li spin-spin relaxation measurement of a Nafion membrane in Li⁺ form at $\lambda = 18$. Right: ¹³³Cs spectrum of a Nafion membrane in Cs⁺ form at $\lambda = 11.8$ (expanded). Deconvolution of the signal yields two Lorentzians of different width.

while the longer T_2 (600 ms) is related to the mobile, dissociated species. Their distribution is also quantitatively accessible from the double exponential fit in figure 4.6: 11 % of the Li⁺ is associated and 89% dissociated. Thus, the association equilibrium



is defined by the association constant according to the mass action law:

$$K_{\text{Li}^+} = \frac{b_{\text{Li}^+_{\text{associated}}}^{\text{mem}}}{b_{\text{Li}^+_{\text{dissociated}}}^{\text{mem}} \cdot b_{-\text{SO}_3^-}} = 0.045 \text{ kg mol}^{-1} \quad (4.3)$$

Unfortunately a ¹³³Cs CPMG sequence cannot be used for the Cs⁺ membrane, as the relaxation times are too short, even though an over hydrated membrane was used. Typically, regular Nafion in Cs⁺ form just takes up only 7 water molecules per functional group, but when it is boiled in water (optionally under pressure) it may swell even further. This way, a Cs⁺ membrane with $\lambda = 11.8$ is used for the NMR analysis. As the spin-spin relaxometry is not available, a line shape analysis was carried out. The spectral line, whose full width at half maximum is reciprocal proportional to the T_2 (see equation (2.11)), can also give quantitative information about the population of

the different states, as long as the exchange between the species is in a range, that allows for a deconvolution of the line shape in two separate lines. Such a deconvolution was performed (see figure 4.6 right) and results in populations of 80.5 % for the "slow" (associated) Cs^+ and only 19.5 % for the "fast" (dissociated) Cs^+ . With the hydration level of $\lambda = 11.8$, the association constant K_{Cs^+} can be obtained:

$$K_{\text{Cs}^+} = 4.5 \text{ kg mol}^{-1} \quad (4.4)$$

These values (4.3) and (4.4) then allow calculation of the ion partitioning as a function of the hydration number λ without any adjustable parameter:

$$\begin{aligned} x_{\text{Li}^+}^{\text{mem}} &= x_{\text{Li}^+}^{\text{mem}}_{\text{associated}} + x_{\text{Li}^+}^{\text{mem}}_{\text{dissociated}} \\ &= \alpha \frac{M_w \lambda + 2(\alpha + \beta) - \sqrt{M_w \lambda (M_w \lambda + 4(\alpha + \beta))}}{2(\alpha + \beta)^2} + x_{\text{Li}^+}^{\text{sol}} \frac{\sqrt{M_w \lambda (M_w \lambda + 4(\alpha + \beta))} - M_w \lambda}{2(\alpha + \beta)} \end{aligned} \quad (4.5)$$

with $\alpha = x_{\text{Li}^+}^{\text{sol}} K_{\text{Li}^+}$, $\beta = x_{\text{Cs}^+}^{\text{sol}} K_{\text{Cs}^+}$ and $M_w = 0.018 \text{ kg mol}^{-1}$ being the molar mass of water. The calculated values match the experimental data extremely well, when the following recursive definition of λ is implemented:

$$\lambda = x_{\text{Li}^+}^{\text{mem}} \cdot 18 + x_{\text{Cs}^+}^{\text{mem}} \cdot 7 \quad (4.6)$$

where 18 is the typical hydration number of Li^+ form Nafion and 7 of Cs^+ form Nafion (non-expanded). The result is plotted along with partitioning curves for different values of λ in figure 4.7. Note, that the calculations are not a fit, but the underlying model is only based on experimentally obtained parameters. Therefore, it seems to be a striking observation, that the calculations almost perfectly match the experimental partitioning data (from chapter 4.1.2), when λ scales with the respective partitioning. As expected, the selectivity of ion uptake diminishes with increasing membrane hydration (swelling). This trend is even supported by the partitioning data of the Aquivion solution from chapter 4.1.1, which represents essentially extremely swollen Nafion. The fact that the matching is not perfect anymore reflects the (small) deviations of the association constants in the diluted case (dissolved Aquivion) from the measured values in membranes at lower water content.

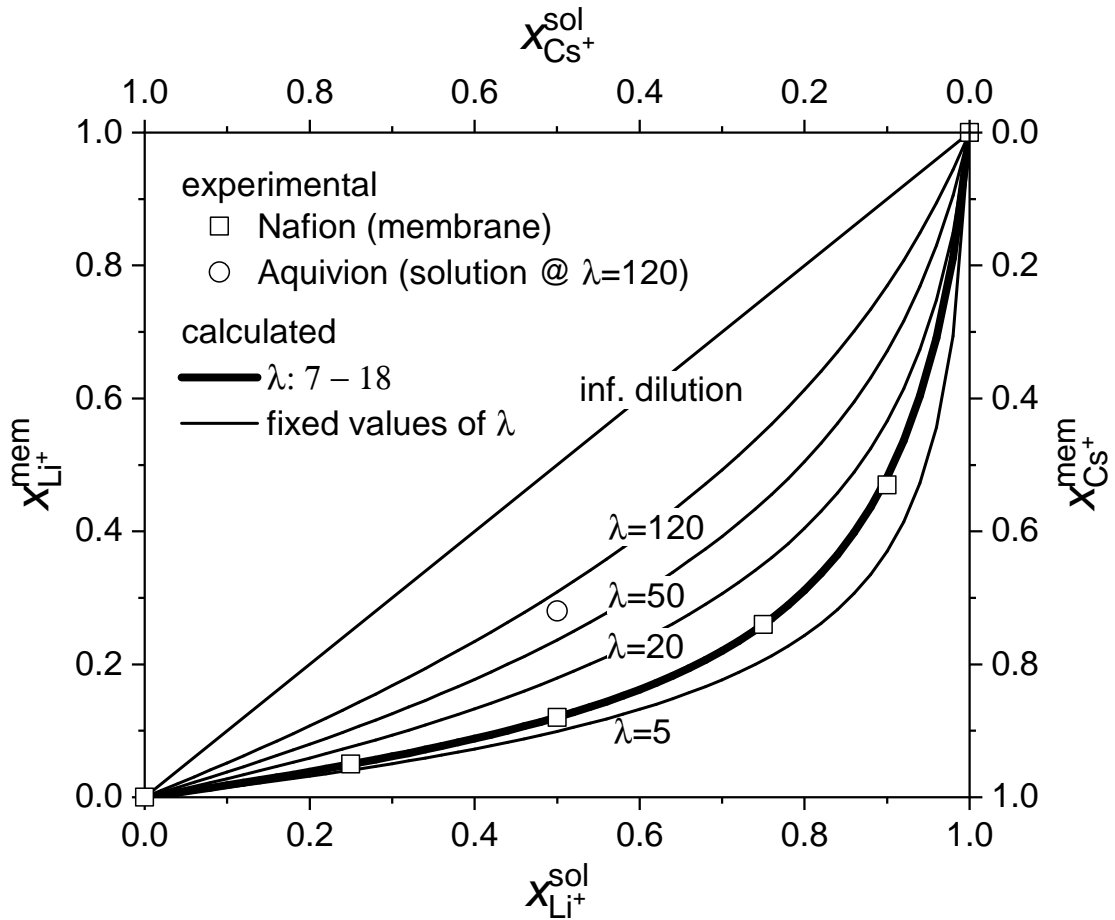


Figure 4.7: Experimental data together with the very well fitting calculated Li^+/Cs^+ partitioning in Nafion according equation (4.5) - and (4.6) for the bold line - using experimental values for K_{Li^+} and K_{Cs^+} . The diminishing of selective uptake of Cs^+ over Li^+ progressively with increasing membrane hydration is experimentally confirmed by partitioning of the Aquivion solution.

In literature [29], a suggested partitioning coefficient

$$S_{\text{Cs}^+}^{\text{Li}^+} = \frac{b_{\text{Cs}^+}^{\text{mem}} b_{\text{Li}^+}^{\text{sol}}}{b_{\text{Li}^+}^{\text{mem}} b_{\text{Cs}^+}^{\text{sol}}} \quad (4.7)$$

cannot reproduce the ion partitioning satisfactorily (see figure 4.8) It is only possible to cover the correct partitioning for either low or high $x_{\text{Li}^+}^{\text{sol}}$, but not over the whole range. Hence, the evidence of experimental data is more in favor of the above suggested two state model. In order to elaborate how this model accounts for the counter-ion partitioning, the rational behind equation (4.5) can be explained by the idea, that Li^+ and Cs^+ ions share the fixed ionic groups of the membrane as counterpart for association

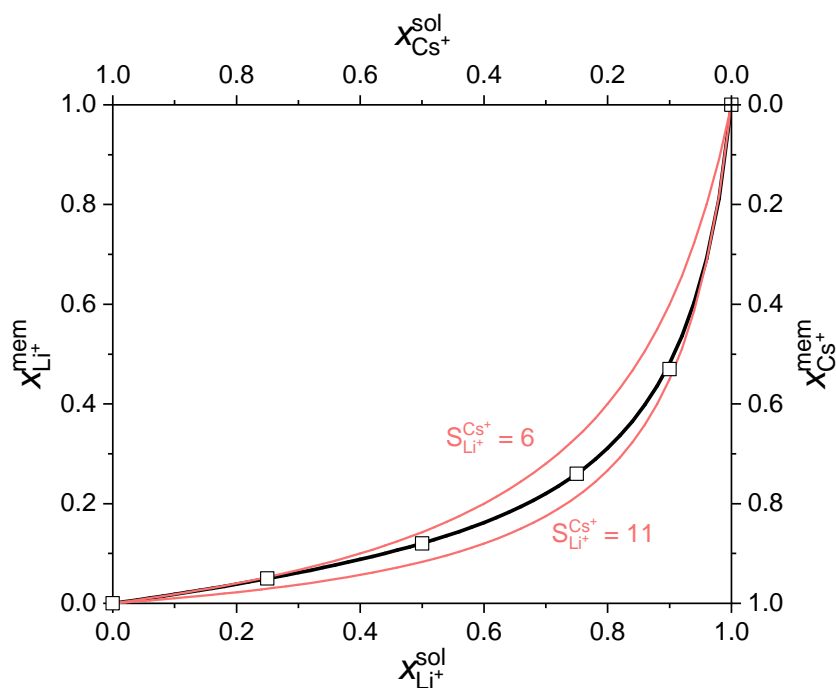


Figure 4.8: Ion partitioning fits with partitioning coefficients (red lines) and the calculation with equation (4.5) for comparison (black line).

according to the mass action law. The particular association constant is derived from membranes in the respective pure cation form and then assigned to the equilibrium situation with both cations. The concentration ratio of the mobile (dissociated) species in the aqueous phase is actually assumed to be identical to the corresponding ratio in solution, while for the bound species, the ones with the highest association constant (here Cs^+) are enriched within the membrane (see figure 4.9). Therefore, increasing hydration (λ), i.e. increasing dissociation of bound ions, is expected to lead to a more even distribution of counter-ions between solution and membrane. The partitioning for $x_{\text{Li}^+}^{\text{sol}} = x_{\text{Cs}^+}^{\text{sol}} = 0.5$ as a function of λ is shown in figure 4.9. As in this two state model, the mobile ion fraction in the membrane is the same as in the external solution, the transference numbers do also not differ, which is already anticipated from the partitioning and mobility measurements from chapter 4.1.1.

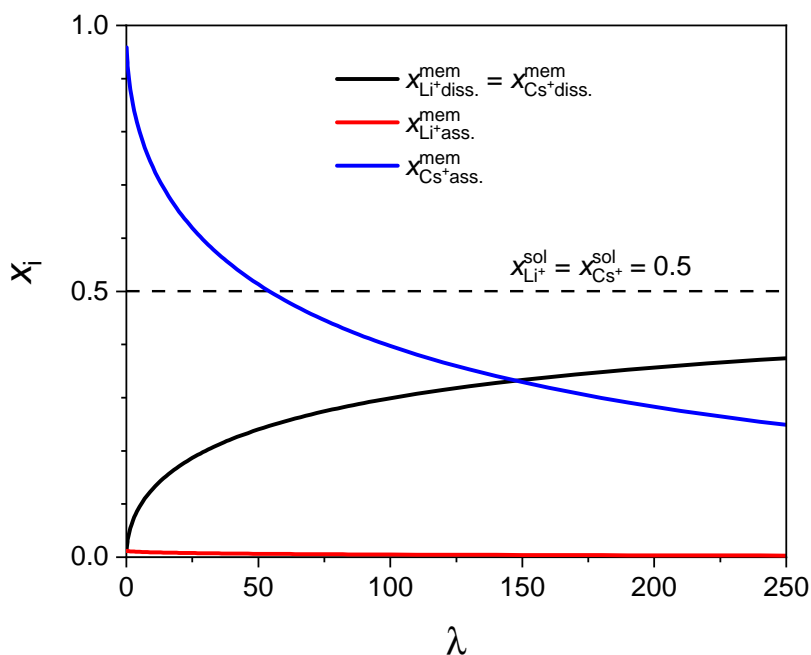


Figure 4.9: Fractions of Li^+ and Cs^+ associated and respectively dissociated from the fixed ionic group of Nafion equilibrated in dilute aqueous solution containing same amounts of Li^+ as Cs^+ .

4.1.4 Donnan exclusion: extended Donnan equation

So far, the partitioning of different cations (here Li^+ and Cs^+) between CEMs and solutions of low molality were considered. Under these conditions the concentration of co-ions within the membrane is negligible, and the electroneutrality condition demands the sum over all counter-ion concentrations in the membrane to equal the concentration of fixed ionic groups (IEC). For higher molarities, however, co-ions enter the membrane to a larger extent and with them an equivalent number of counter-ions as described by the Donnan equation (see chapter 3.1, equation (3.9)). In the following, the focus will be moved from the counter-ion counter-ion discrimination, called specificity or selectivity [48], to the counter-ion co-ion discrimination, called permselectivity [49], which is the most prominent property of IEMs. First, the validity of the Donnan equation for two 1,1 electrolytes (LiCl and CsCl) in the concentration range 1 M to 5 M is tested. In doing so, two severe types of deviation reflecting the different chemical character of Li^+ and Cs^+ can be observed (see figures 4.10 and 4.11). The

effects are accounted for by modifying the input parameters of the Donnan equation, i.e. the molality of all ions and the molality of electrochemically active fixed-ions. The actual co-ion (Cl^-) uptake was measured by potentiometric titration with a AgNO_3 solution and an Ag electrode after extracting all ions from the equilibrated membrane. In the case of Nafion being immersed in aqueous solutions of CsCl, the the co-ion uptake is tremendously higher than anticipated from the Donnan equation, which is shown in figure 4.10.

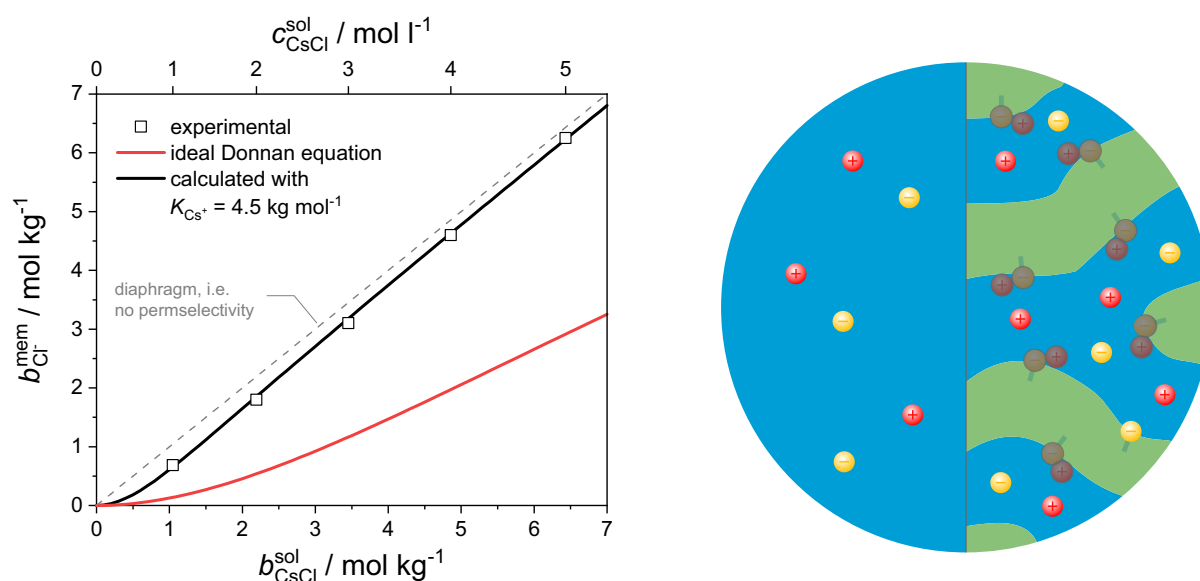


Figure 4.10: Left: Co-ion uptake of Nafion in a CsCl solution, which is higher than expected from the ideal Donnan equation. Implementing the concept of ion association by the mass action law, the measured data is described very well. Right: Schematic of the membrane in equilibrium with the CsCl solution. Association of counter-ions is neutralizing the fixed-ions (greyed out), allowing co-ions to enter the membrane.

This means that the breakdown of Donnan exclusion (see chapter 3.1, figure 3.1) occurs earlier than expected, and permselectivity drops. The false prediction of equation (3.9) has its reason in the fact that this ideal Donnan equation assumes the activity coefficients in the membrane's aqueous phase to be the same as in the external solution: $\gamma^{\text{mem}} = \gamma^{\text{sol}}$. In this way, it was possible to make predictions in the first place, since molalities could be used instead of activities. As a simple trick to improve the prediction tremendously without dealing too much with activities has turned out to remove the associated (immobilized) ions from thermodynamic equilibrium. Implementing

the Cs⁺ counter-ion association with the sulfonic acid group of Nafion, described by the mass action law ($K_{\text{Cs}^+} = 4.5 \text{ kg mol}^{-1}$), results in the following four equations which describe the equilibrium and distribution of ions when a CEM is in contact with a CsCl solution:

$$b_{\text{Cs}^+}^{\text{sol}} \cdot b_{\text{Cl}^-}^{\text{sol}} = b_{\text{Cs}^+_{\text{dissociated}}}^{\text{mem}} \cdot b_{\text{Cl}^-}^{\text{mem}} \quad (4.8a)$$

$$K_{\text{Cs}^+} = \frac{b_{\text{Cs}^+_{\text{associated}}}^{\text{mem}}}{b_{\text{Cs}^+_{\text{dissociated}}}^{\text{mem}} \cdot b_{-\text{SO}_3^-}} \quad (4.8b)$$

$$b_{\text{fixed}} + b_{\text{Cl}^-}^{\text{mem}} = b_{\text{Cs}^+_{\text{dissociated}}}^{\text{mem}} + b_{\text{Cs}^+_{\text{associated}}}^{\text{mem}} \quad (4.8c)$$

$$b_{\text{fixed}} = b_{-\text{SO}_3^-} + b_{\text{Cs}^+_{\text{associated}}}^{\text{mem}} \quad (4.8d)$$

where b_{fixed} is directly connected with the water content λ via equation (3.11). It must be added, that the number of water molecules per fixed ionic group of Nafion submerged in a CsCl solution is dropping from $\lambda = 7$ in a dilute solution almost linearly with the concentration to $\lambda = 5$ for a 5 M solution. The agreement of the co-ion Cl⁻ uptake as obtained from the equation set (4.8) with the experimental data is almost perfect (see figure 4.10), while the ideal Donnan equation significantly underestimates the uptake. In fact, the pronounced co-ion uptake is not significantly different from a diaphragm (e.g. porous membrane without fixed ionic groups), which is evident when assuming neutralization of almost all fixed-ions.

Interestingly, in the case of Nafion being immersed in aqueous solutions of LiCl the opposite trend is observed: the co-ion uptake is actually lower than anticipated by the Donnan equation (see figure 4.11). Inspired by the suggestions of Stokes from 1948 [35], that ions may bind solvent molecules in their solvation shell, which reduces the available amount of solvent and thereby increases the effective molality (activity), Glueckauf measured in 1955 the number of water molecules h per Li⁺ hydration shell in a cation exchange resin with sulfonic acid groups (since at that time Nafion had not yet been available) [50]. The value $h = 3.3$ he obtained in water activity measurements

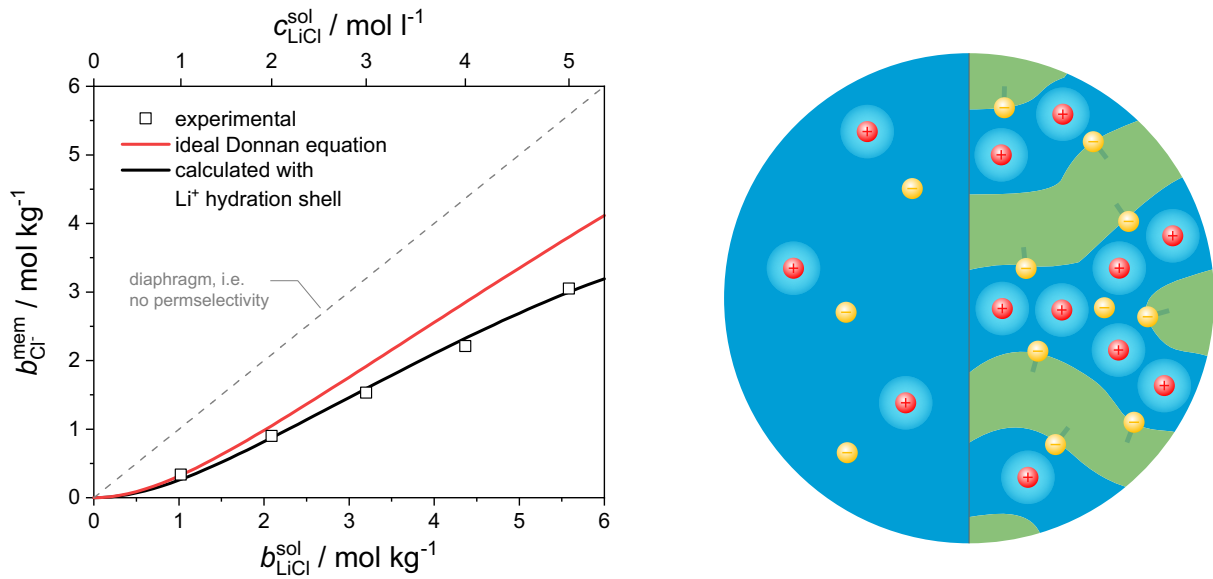


Figure 4.11: Left: Co-ion uptake of Nafion in a LiCl solution, which is lower than expected from the ideal Donnan equation. By implementing the concept of ion hydration shell, which reduces the amount of solvent, the measured data is described very well. Right: Schematic of the membrane in equilibrium with the LiCl solution. Hydration shell of counter-ions is increasing the effective concentrations by decreasing the amount of solvent (relatively more within the membrane than in the external solution) and thereby increasing co-ion retention.

is used in this work. It reduces the effective molalities b^* of both the fixed-ions in the membrane and of the external LiCl solution:

$$b_{\text{fixed}}^* = \frac{b_{\text{fixed}}}{1 - h \cdot b_{\text{Li}^+}^{\text{mem}} \cdot 0.018 \text{ kg mol}^{-1}} \quad (4.9a)$$

$$b_{\text{LiCl}}^* = \frac{b_{\text{LiCl}}^{\text{sol}}}{1 - h \cdot b_{\text{LiCl}}^{\text{sol}} \cdot 0.018 \text{ kg mol}^{-1}} \quad (4.9b)$$

Relatively, the effect on the external solution is less severe, because in general $b_{\text{Li}^+}^{\text{mem}} > b_{\text{LiCl}}^{\text{sol}}$. It is illustrated in figure 4.11 (left) by the small amount of water molecules available in the membrane where the subtracting and reassigning of molecules to the hydration shell reduces the remaining amount of solvent molecules severely. As it is described in chapter 3.1, figure 3.1, the molality of fixed ionic groups effects the co-ion exclusion. An increased effective molality of the fixed-ions, i.e. a reduced effective λ , is enhancing the exclusion of co-ions (Cl^-). As Li^+ ions are barely associating with the

fixed-ions, the implementation of the hydrated Li^+ as new species alone is able to describe the co-ion uptake behaviour. The calculations (including the evaluation of the ideal Donnan equation) were performed with a λ decreasing from 18 (dilute solution) to 12 (5 M LiCl).

4.1.5 Transference experiments

In an attempt to verify the deduced implications of the experimental findings on selective transport regarding the counter-ion counter-ion discrimination and the counter-ion co-ion discrimination, transference numbers are measured. Since the selectivity among counter-ions stems from the fact, that the excess of preferably absorbed counter-ions associates with the fixed-ions and thereby is immobilized, the transference number is not expected to be different from the solution (chapter 4.1.3). Averaged tracer diffusion coefficients confirm this anticipation (chapter 4.1.1). The transference numbers are measured in a Hittorf cell (see figure 4.12), where at the anode Cl_2 and at the cathode H_2 are evolving. The anode side with a 1:1 mixture of 1 M LiCl and 1 M CsCl is separated by a CEM from the cathode side with a initial 1:1 mixture of 0.1 M LiCl and 0.1 M CsCl. A constant current is applied and draws⁴ cations from the anode to the cathode side. The chemical composition of the solution at the cathode side is analyzed by ICP OES. Since there is already a base concentration it is to note, that the measured concentration increments Δc are prone to error. Nevertheless, obtained values show low variance and transference numbers are calculated according to:

$$t_{\text{Li}^+} = \frac{\Delta c_{\text{Li}^+}}{\Delta c_{\text{Li}^+} + \Delta c_{\text{Cs}^+}} \quad (4.10)$$

The membranes Nafion, sPSO2-360, and the sPEEK FKE-50 are investigated this way when they are used as separator in the cell. The results are given in table: As expected, the transference numbers do not deviate much from the ones in a dilute equally weighted LiCl/CsCl solution. They are close to the values for dissolved ionomers obtained by PFG NMR, too. All together the evidence is clearly in favor of the proposed ion association model.

⁴in addition to the concentration gradient

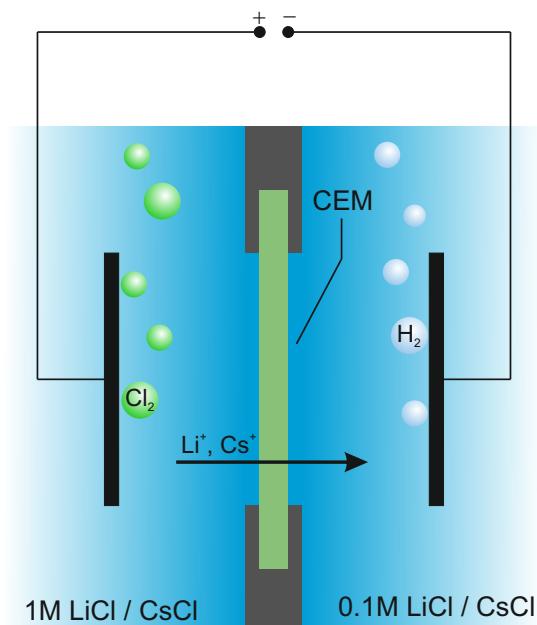


Figure 4.12: Schematic of the Hittorf experiment setup for measuring the Li^+ and Cs^+ transference number in solutions with an initial 1:1 ratio of LiCl and CsCl . At the anode side Cl^- ions are consumed and chlorine is produced in a 1 M solution, at the cathode side hydrogen is produced in a 0.1 M solution. The CEM as separator is either Nafion, sPSO2-360, or the sPEEK FKE-50. Alkali cations from the anode side need to pass the membrane in order to balance the charges. The Li^+/Cs^+ ratio at the cathode side is analyzed by ICP OES.

Ion association still matters, when it comes to the co-ion counter-ion discrimination, the permselectivity. In an attempt to generalize the findings that counter-ion association lowers the co-ion exclusion, i.e. the permselectivity, here an AEM was investigated for generalizing the statements made for CEMs. Therefore the fumasep FAA-3 membrane with trimethylammonium groups, which is known to bind Cl^- ions to some extent [51], is used in an electrolyzer cell (see figure 4.13). When applying a constant current I_c , Cl^- ions are consumed at the anode and Cl_2 evolves, while at the cathode Cu^{2+} is reduced to Cu by plating. Either protons from the anode side or chloride ions from the cathode side need to cross the membrane in order to balance the charges. The pH at the cathode side is measured in regular intervals to track the H^+ concentration. A

Table 4.3: Li⁺ and Cs⁺ transference numbers of different CEMs.

	t_{Li^+}	t_{Cs^+}
aq. solution [14]	0.33	0.67
sPEEK	0.31	0.69
sPSO2-360	0.36	0.64
Nafion	0.33	0.67

reference measurement at 0 A is performed and together with the total flowed charge the transference number is calculated:

$$t_{\text{H}^+} = \frac{\left(10^{\text{pH}_{\text{ic}}(t)} - 10^{\text{pH}_{\text{vA}}(t)}\right) \cdot V_{\text{cathode}}}{I_{\text{c}} \cdot t \cdot F^{-1}} \quad (4.11)$$

With an obtained value of $t_{\text{H}^+} = 0.74$, the transference number appears to be virtually identical to that of 1 M HCl [52]. In other words, local ionic transport of aqueous solutions entering the neutralized ionomer membrane does not change very much. In this way, anion exchange membranes in concentrated acids predominantly conduct protons, a phenomenon which has been recognized qualitatively before [53,54].

4.1.6 Concluding remarks

When a IEM is in contact with aqueous solutions of strong 1,1 electrolytes such as alkali metal halides, both phenomena ion partitioning among counter-ions and Donnan exclusion (co-ion retention) can be explained by three controlling parameters:

1. specific interactions between counter-ions and fixed ionic groups (association constant K_i)
2. total water uptake of the membrane (λ), and
3. the extension of all ions' hydration shell (h)

The counter-ion association and the hydration shell have severe impact on the activity of the ionic species, which is addressed by using effective molalities⁵.

⁵basically the same treatment as introducing an activity coefficient different from 1

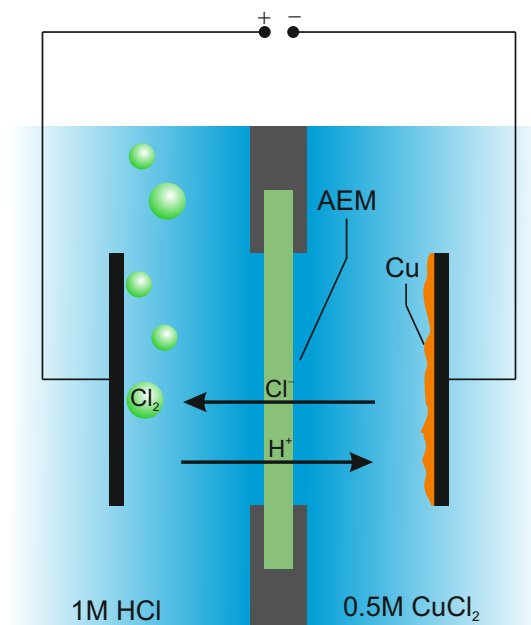


Figure 4.13: Schematic of the Hittorf experiment setup for measuring the H^+ and Cl^- transference number. At the anode side Cl^- ions are consumed and chlorine is produced in a 1 M HCl solution, at the cathode copper is deposited in 0.5 M CuCl_2 solution. The AEM as separator is the fumasep FAA-3 membrane.

I.e. the molecules from the hydration shell are reassigned from the solution to the ionic species, reducing the amount of solvent and increasing the ion's molality explaining the pronounced co-ion retention of the membrane. On the other hand, the associated (immobilized) ions are considered chemically inactive, reducing the effective molality. This can also be perceived as reduction of the concentration of fixed ionic groups by neutralization which leads to an increased co-ion uptake. Additionally, there is no selective counter-ion uptake when considering mobile ions in the membrane only. The degree of counter-ion association decreases with increasing water uptake and increases with increasing acidity of the fixed ionic group for polarizable cations with low electronegativity. It culminates in the extreme case of the super acidic Nafion and the polarizable Cs^+ where co-ion retention almost collapses. Note, that for a lot of applications, properties like gas separation (not covered in this work) still make IEMs preferable over simple diaphragms.

Some of those findings were already discovered in the past, but they were attributed mostly to electrostatics. Manning's counter-ion condensation is used for explaining the failure of the ideal Donnan equation and the increased co-ion uptake in CEMs [55]. A critical parameter here is the average separation length of fixed-ions and the Bjerrum length, which again depends on the dielectric constant. The literature in question uses for their calculations an arithmetic mean of the dielectric constants of water and the respective polymer. This is in conflict with the finding that the local dielectric constant of water in Nafion is close to the bulk value [56]. However, this work avoids the discussion by using also dissolved ionomers, where the separation length is doubtlessly beyond the Bjerrum length. Still, counter-ion association was observed with the relevant parameter being the specific interaction between counter-ion and fixed-ion. If electrostatics were responsible for the association, respectively condensation, there would not be a difference in the behavior between different counter-ions (e.g. the actual condensation of alkali cations on polyphosphates does not show a trend from low to high atomic number [57]). Finally, the fact, that ion partitioning is obviously well described by using mass action laws for the ion pairing process, is in favor of specific chemical interactions being the major driving force for the observed phenomena rather than electrostatics. In his seminal paper Manning clearly stated: "... thus a conventional mass-action formulation does not hold for counter-ion binding in polyelectrolyte solutions." [42].

For the counter-ion counter-ion selectivity, Pintauro et al. have modeled the effect fixed-ions have on the orientation of water and how this affects the solvation of the diverse counter-ions [44,45]. These purely electrostatic considerations alone qualitatively yield the right trends with respect to ion partitioning (these authors have also used Li^+ and Cs^+ as counter-ions), but such models miss the effects which the fixed-ion's acidity has on counter-ion localization. Furthermore, their model implies "increasing the membrane's pore-wall charge density will increase the cation cation absorption selectivity" [45]. This is contradicting the finding in this work, that Nafion and BP-ArF4 (with different "pore-wall charge density" but the same acidity of their fixed-ions) show virtually the same ion partitioning.

One of the unique findings in this work is that the selectivity of ion uptake does not depend on the membrane's ion exchange capacity (IEC) but very much on slight changes of the fixed ionic-group's chemical character. For ion uptake of ionomers with sulfonic fixed-ionic groups, the Cs^+/Li^+ preference markedly increases with increasing acidity of the sulfonic group. The Brønsted acidity is affected by the chemical influence of the polymer that the ionic group is attached to. The PFSA Nafion is a super-acid which shows not only the most pronounced Cs^+/Li^+ selectivity but also the lowest degree of dissociation for both ions. This seems counter-intuitive considering the lower negative charge density on the conjugated base ($-\text{SO}_3^-$), which is expected to reduce the electro-static attraction with cations. However, the reduced electric field strength around the fixed-ionic group also reduces the interaction with hydration water, therefore favoring ion association. This effect is part of the electro-static model developed by Eisenman [48,58] partially explaining the increasing cation association with increasing Brønsted acidity. The Brønsted acidity increase of Nafion not only goes along with a decreased negative charge density but also an increased electronegativity of the conjugated base ($-\text{SO}_3^-$) creating a driving force for electron transfer from the highly polarizable Cs^+ towards the fixed ionic group leading to some coordinate covalent bonding.

4.2 Electroselectivity

Electroselectivity (according to Helfferich, Bonhoeffer was the first to label it "Elektroselectivität" [29]) describes the phenomenon of the purely electrostatic preference of ions according to their higher or lower valence.

4.2.1 Setting

As a consequence of the diagonal relationship in the periodic table [59], lithium and magnesium deposits often exist side by side. With the increasing demand of lithium as a material in the energy and electronics industry, there comes a growing interest regarding lithium production and the separation processes of lithium and magnesium. Lake brines, as abundant lithium resources, are exploited largely to extract lithium. Selective electrodialysis is an emerging technology using electroselective membranes to recover and separate lithium from brines with high lithium and magnesium mass ratio [60].

Other applications with the necessity for electroselective membranes are sea water concentration for table salt production or reverse electrodialysis, where energy is retrieved from the difference in the salt concentration between seawater and river water. For both, cross transport of multivalent ions needs to be suppressed because it decreases the product's purity and depreciates the energy efficiency [61,62]. So-called monovalent selective CEMs are established for the mentioned applications. These are typically traditional CEMs, polymers with fixed anionic groups, with an AEM coating, respectively a thin layer of polycations (see figure 4.14). The purpose of the polycation layer is to repel multivalent cations over monovalent cations. Monovalent selective AEMs are designed analogously, i.e. a polyanion layer (CEM layer) is deposited on a AEM. The rationale behind the monovalent selectivity is recently often referred to be the electrostatic rejection of ions towards the same charged polyionic coating, which is stronger for multivalent ions than the coulombic repulsion imposed to monovalent ions [63–65]. This explanation somehow implies that the AEM layer is charged as a whole, but in fact, mobile counter-ions (here cations) balance the charge and preserve electroneutrality. Nevertheless, the electric potential is high in the AEM layer compared to the

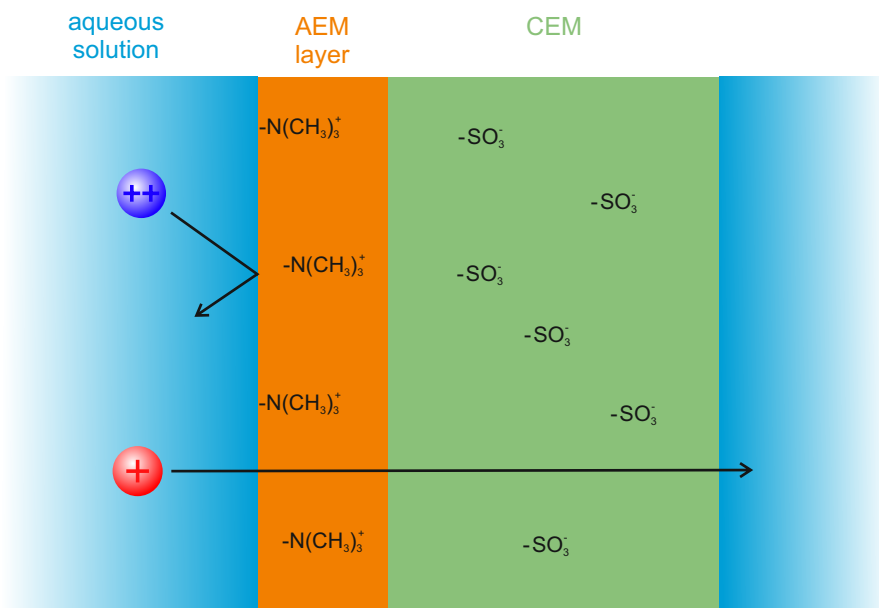


Figure 4.14: Schematic of a CEM with a AEM layer for selective monovalent cation transport.

adjacent solution according to equation (3.5) (Donnan potential, see chapter 3.1) and is responsible for the higher retention of multivalent cations compared to monovalent ones (electroselectivity). In this work, the focus is laid on explaining such effects on electroselectivity by extending Helfferich's considerations [29] regarding the Donnan equilibrium with respect to electroselective ion uptake.

4.2.2 Mono- vs. divalent co- and counter-ions

The separation of monovalent cations and multivalent cations is a current issue (see chapter 4.2.1), which is not only relevant for many industries but also challenging for academic explorations. In 1959, Helfferich already described the preferred uptake of divalent cations over monovalent cations in CEMs [29] backed by experimental data of cation exchange resins [66]. For a CEM adjacent to an external solution of monovalent co-ions (anions) and mono- and divalent counter-ions (cations) of the same charge equivalent:

$$(b^{\text{sol}} =) b_{-}^{\text{sol}} = b_{+}^{\text{sol}} + 2 \cdot b_{2+}^{\text{sol}} \quad (4.12a)$$

$$b_{+}^{\text{sol}} = 2 \cdot b_{2+}^{\text{sol}} \quad (4.12b)$$

He made following assumptions for the equilibrium situation:

- no swelling pressure
- activity coefficient ratio within the membrane is the same as in the solution (i.e. no difference of counter-ions regarding specific interactions)
- perfect co-ion exclusion (no electrolyte uptake)

Due to the latter assumption, the resulting equation for the fraction of counter-ions in the membrane x^{mem} (normalized to the equivalent charge) is only valid for very low concentrations of the external solution b^{sol} :

$$x_{2+}^{\text{mem}} = 1 - x_+^{\text{mem}} \quad (4.13a)$$

$$x_+^{\text{mem}} = \frac{1}{4} \cdot \left(\sqrt{\left(\frac{b^{\text{sol}}}{b_{\text{fixed}}}\right)^2 + 8 \cdot \frac{b^{\text{sol}}}{b_{\text{fixed}}}} - \frac{b^{\text{sol}}}{b_{\text{fixed}}} \right) \quad (4.13b)$$

At higher molalities, when additional electrolyte uptake is considered, the set of equations describing the ion partitioning obtained by the equilibrium of equation set (3.2) for two kinds of cations is the following:

$$b_{\text{fixed}} + b_-^{\text{mem}} = b_+^{\text{mem}} + 2 \cdot b_{2+}^{\text{mem}} \quad (4.14a)$$

$$b_+^{\text{sol}} \cdot b_{2+}^{\text{sol}} = b_+^{\text{mem}} \cdot b_-^{\text{mem}} \quad (4.14b)$$

$$(b_+^{\text{mem}})^2 = b_-^{\text{sol}} \cdot b_{2+}^{\text{sol}} \quad (4.14c)$$

These equations can be solved explicitly and the result is plotted in figure 4.15.

For an infinite dilute external solution with equivalent mono- and divalent cations, the counter-ions in the CEM are just divalent without any monovalent ion. The reason is simply the fact, that this minimizes the concentration gradient (chemical potential difference) of mobile cations between the membrane and the solution and the corresponding Donnan potential difference (see equation (3.5)). When the electrolyte concentration increases, not only additional monovalent cations enter the membrane, but also the divalent ion concentration decreases, before it rises again due to the electrolyte uptake (see figure 4.15).

As a further extension of the electroselectivity according to Helfferich, the considerations made can also be applied to valency-dependent co-ion uptake. In fact, the selective uptake of divalent over monovalent counter-ions is reversed when it comes

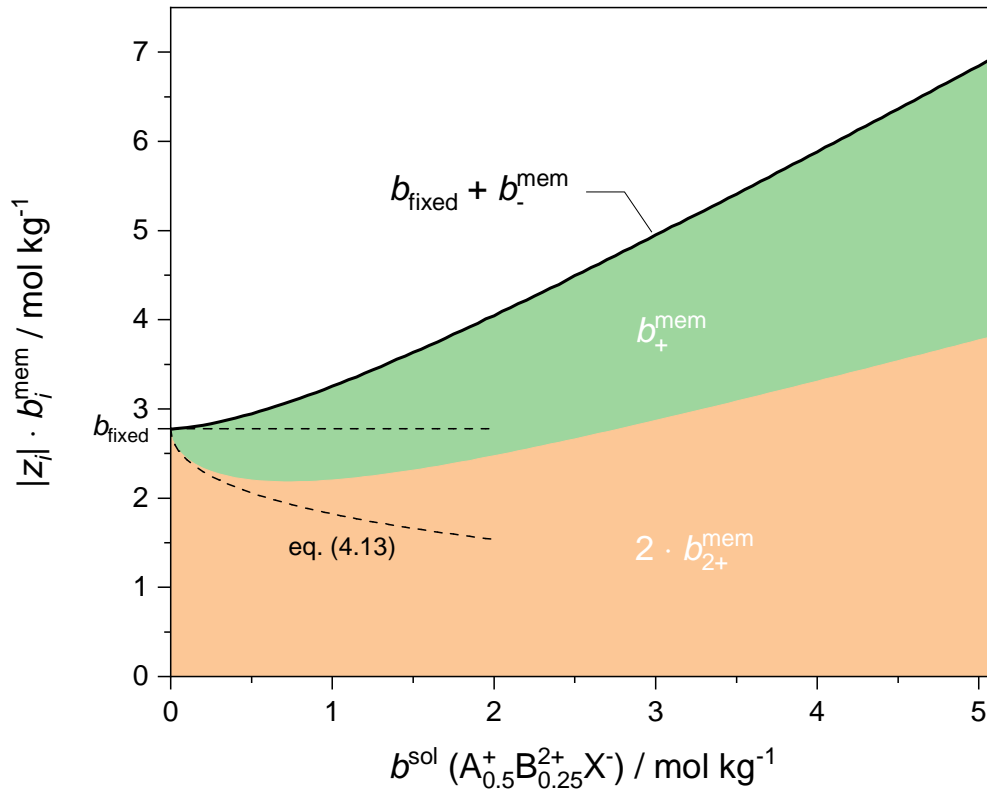


Figure 4.15: Calculated mono- and divalent counter-ion (cation) uptake in a CEM with $\lambda = 20$ ($b_{\text{fixed}} = 2.78 \text{ mol kg}^{-1}$) according to equations (4.14). The dashed line shows the calculation according Helfferich (equation (4.13)).

to co-ions. For the same reasons mentioned above (Donnan potential), the uptake of monovalent co-ions is preferred over divalent co-ions. For an AEM equilibrated with an external solution of monovalent counter-ions and mono- and divalent co-ions of the same charge equivalent (equations (4.12) from the CEM case still hold true, while anions and cations just switched their role as co- and counter-ion) the Donnan equilibrium is governed by the following set of equations:

$$b_{\text{fixed}} + b_+^{\text{mem}} + 2 \cdot b_{2+}^{\text{mem}} = b_-^{\text{mem}} \quad (4.15a)$$

$$b_-^{\text{sol}} \cdot b_+^{\text{sol}} = b_-^{\text{mem}} \cdot b_+^{\text{mem}} \quad (4.15b)$$

$$(b_-^{\text{sol}})^2 \cdot b_{2+}^{\text{sol}} = (b_-^{\text{mem}})^2 \cdot b_{2+}^{\text{mem}} \quad (4.15c)$$

The solution of (4.15) is plotted for $\lambda = 20$ in figure 4.16 as blue line. The electrostatic driving force $zF\phi$ for the co-ions is opposite to the driving force for the counter-ions, and this is higher for divalent compared to monovalent co-ions (cations for AEMs). Therefore, the membrane selectively takes up monovalent cations from dilute solutions. Of course, the fraction of mobile cations (co-ions) in the membrane is smaller compared to a CEM, and the decay of this selectivity with increasing salt concentration of the solution is less pronounced than for the discrimination of counter-ions with different charge. Note that the blue line (partitioning in AEM) and the red line (partitioning in CEM) in figure 4.16 are not symmetrical, i.e. the latter approaches faster the asymptote at 0.5.

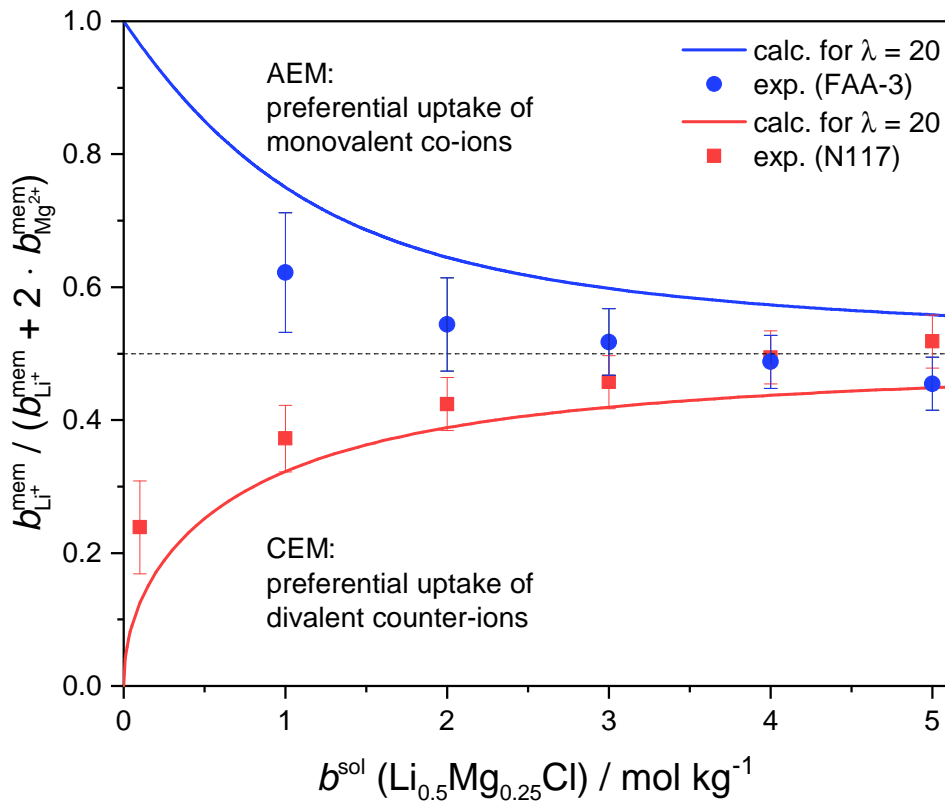


Figure 4.16: Fraction of monovalent cation uptake.

The validity of these equations (4.14) and (4.15) is qualitatively checked by equilibrating a CEM (Nafion N117) and an AEM (fumasep FAA-3) in solutions of $\text{LiCl} / \text{MgCl}_2$

mixtures with equivalent charge ratio (i.e. a molar ratio of 2:1). In particular for the preferred monovalent co-ion uptake, to my knowledge, there does not exist data in literature yet, even though the effect is already exploited by monovalent selective membranes. The nature of IEMs, in the sense of co-ion exclusion, allows only measuring significant amounts of cations in AEMs at elevated concentrations of the external equilibration solution, while for CEMs they can be measured when the external solution is dilute. However, for both membranes, the concentration dependent uptake of the ions is measured by ICPs OES. In figure 4.16 the measured fraction of monovalent ions within the counter-ions or respectively the co-ions is plotted together with the calculation from equations (4.14) and (4.15) for a water content fixed to $\lambda = 20$, which is an upper limit, as in reality the water content decreases with higher molality of the solution.

While the qualitative trends are confirmed, the agreement of measured data and the calculated estimation is rather poor. Especially, the difference in case of the AEM FAA-3 seems high. A possible explanation is the counter-ion condensation of Cl^- , which promotes diaphragm-like behaviour (see chapter 4.1). Additionally, there is even a reversal of the qualitative trend at higher molalities ($>4 \text{ mol kg}^{-1}$). This deviation stems from the fact that both specific interactions and the swelling pressure (with differences in the partial molar volume) are neglected. Such effects may mask the influence of electroselectivity, particularly at higher molalities.

4.2.3 Concluding remarks and outlook

Electroselectivity is an immediate consequence of the presence of fixed-ionic groups. High valency counter-ions and low valency co-ions are preferred in ion uptake due to the Donnan potential. Still, the implications for the separation of ions with different valence state are actually not straightforward. Other works suggest that the fractions of ions with different valence state in the membrane are also functions of current density and boundary conditions [65]. E.g. a CEM preferentially contains and conducts divalent cations rather than monovalent cations in dilute solutions only for very low current density. With increasing current density, divalent cations progressively deplete in a near-surface layer of the contacting solution at the anode side. This depletion process is not only the consequence of the preferred transport of divalent cations by the ionic current, it is also due to a less efficient transport of divalent cations⁶ from the bulk of the solution into the near surface layer. Therefore, an increasing fraction of monovalent cations incorporate and conduct in the membrane [67,68].

This monovalent cation transport in CEMs may be even enhanced by coating the anode-side of the CEM with a very thin layer of an AEM (see figure 4.14). As shown above theoretically and experimentally, AEMs preferably take up monovalent over multivalent co-ions, which are counter-ions for a CEM. The considerations of Helfferich regarding electroselective ion uptake in IEMs (exclusively for counter-ions) are extended for higher concentrations beyond Donnan exclusion and the discrimination among co-ions of different valency is newly implemented, explaining the experimentally observed trends satisfactorily. Nevertheless it is to be mentioned that this work refers to systems in equilibrium and the situation in dynamic systems may differ while trends are covered correctly.

⁶the rather extended and robust hydration shells of higher valency ions generally reduce their diffusion coefficient in water

4.3 Impact of morphology

So far, morphological effects have been deliberately excluded by considering relatively small ions in well-swollen IEMs. For larger ions or other dissolved species within ionomers with narrow aqueous ionic domains, however, steric effects on ion mobility may emerge [69–71]. After a short presentation of the state of the art regarding exploitation of ion sieving in RFBs in chapter 4.3.1, such effects are studied in chapter 4.3.2 on the basis of the model system Nafion - tetrakis(hydroxymethyl)phosphonium, where the diffusion coefficients of a small and a large species in the same sample are measured at different water contents. Following, in chapter 4.3.3 ionic mobility of H^+ and VO^{2+} in IEMs is investigated by conductivity measurements in dependence of the hydration level of the membrane. Aqueous domain widths of IEMs in VRFBs are experimentally determined by SAXS measurements in section 4.3.4 and implications on the VRFB efficiency are discussed and underpinned by experimental data.

4.3.1 Setting

Effects regarding steric restrictions on a species' mobility are known occurring for molecular transport through the open defined structures of zeolites [72]. For technical zeolites, also the term *molecular sieve* is used referring to the observations that molecular diffusion coefficients are high provided the molecule is smaller than the morphological bottleneck along the diffusion pathway. Such sieving effects were also demonstrated for the mobility of ionic species [73], and zeolite membranes have been used in VRFB applications for rejecting large electrochemically active vanadium species [74]. The fact, that also nano-filtration membranes perform reasonably well in VRFBs [75] and polymeric nano-porous membrane coatings improve performance for this application [76,77] qualitatively demonstrates ion sieving also for this type of porous polymers. As for such uncharged polymeric materials, the structure (morphology) of most IEMs is ill-defined, and hence, reported transport/morphology relationships are, to date, at best qualitative [78].

4.3.2 Sieving effect in an IEM

The IEM with the most distinct morphology is prototypical Nafion. The available information about its locally flat morphology, where the aqueous domain width scales linearly with the water content, allows one to reveal quantitative relations between this morphological feature and the mobility of ionic species in Nafion. A suitable counter-ion for such investigations is an ion of distinct dimension: e.g. the tetrakis-(hydroxymethyl)phosphonium cation (see figure 4.17). The cation's diffusion coeffi-

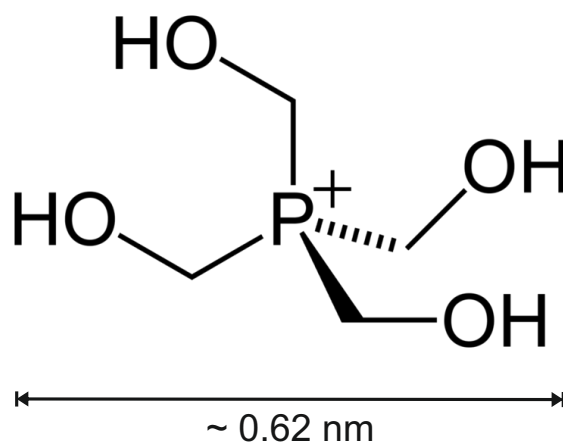


Figure 4.17: Chemical structure tetrakis(hydroxymethyl)phosphonium.

cient in dilute chloride solution is experimentally determined by PFG NMR (where both can be used, the ^1H or ^{31}P signal) to $D = 7.9 \times 10^{-10} \text{ m}^2 \text{ s}^{-1}$. The hydrodynamic diameter of the phosphonium ion is calculated with equation (2.1) to be 0.62 nm, which coincides with the geometrical extension of this cation. This means that the ion does not have a pronounced hydration shell and its radius in an IEM is not affected by the level of hydration.

The CEM Nafion with tetrakis(hydroxymethyl)phosphonium counter-ions now serves as model system, where the diffusion coefficients of a small (water molecules) and a large species (phosphonium ions) in the same sample are measured at different water contents. In figure 4.18 an exemplary PFG NMR echo attenuation is shown, from which both diffusion coefficients can be obtained. The diffusion coefficients of the phosphonium cation are crosschecked by ^{31}P NMR. Since diffusion coefficients strongly depend

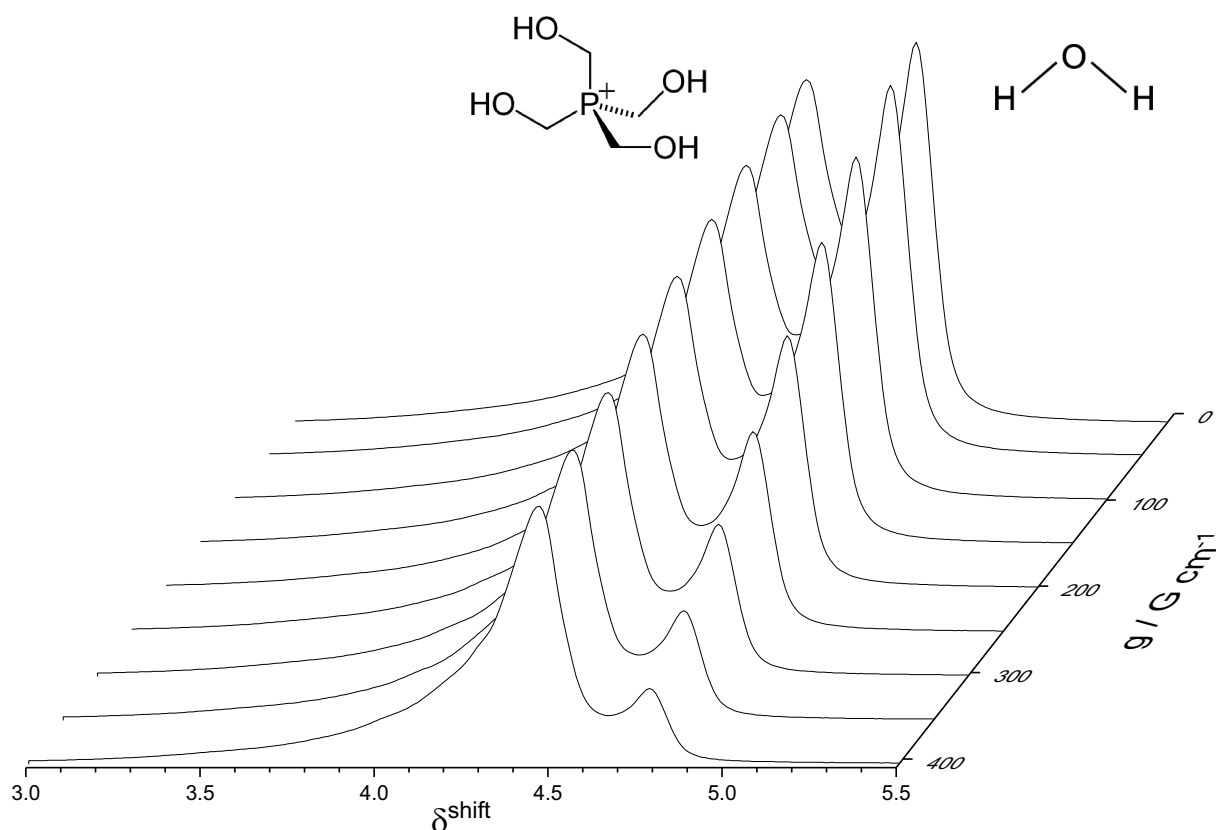


Figure 4.18: Echo attenuation of a ^1H PFG NMR experiment on Nafion in tetrakis(hydroxymethyl)phosphonium form at $\lambda = 5.3$. The peak from water protons ($\delta^{\text{shift}} = 4.8$) is attenuating faster with increasing field strength than the signal stemming from the protons of the phosphonium ion.

on the water content (especially at low values), and experimental data of water contents are usually flawed with large errors, only measurements on identical samples yield high accuracy when comparing small and large species. The measured diffusion coefficients of water $D_{1\text{H}}$ and the large phosphonium cation $D_{31\text{P}}$ in Nafion are shown in figure 4.19 as a function of the water volume fraction Φ_{aq} including data for a dilute aqueous solution ($\Phi_{\text{aq}} = 1$). The diffusion coefficient of neutral water represents the mobility of hydronium ions (H_3O^+) which is known to be close to the water diffusion coefficient [79]. The choice of a neutral species also avoids mixed ion effects, which are small in liquids but still may introduce further complications. At high water content, the diffusion coefficients of both species are similarly affected by the reduction of the water content, i.e. the narrowing of the aqueous domain, while they diverge for lower

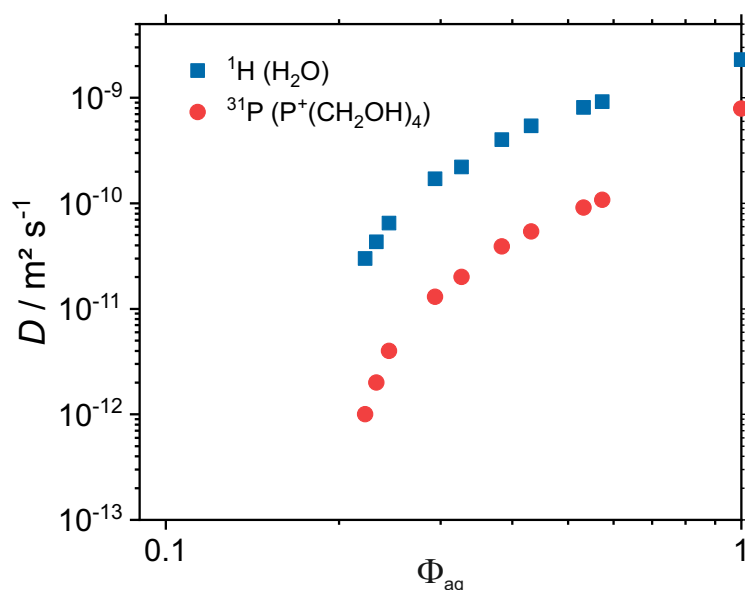


Figure 4.19: Diffusion coefficients of water and tetrakis(hydroxymethyl)phosphonium in Nafion as a function of water volume fraction Φ_{aq} . Also the values in a dilute aqueous tetrakis-(hydroxymethyl)phosphonium chloride solution are given ($\Phi_{\text{aq}} = 1$).

water contents. The aqueous domain width can be calculated based on the fact that it scales linearly with the water content (also for other cations than H^+ [39]) while the polymeric phase width is constant at 2.8 nm. In figure 4.20, the ratio of the diffusion coefficients of water and tetrakis(hydroxymethyl)phosphonium is plotted as a function of the width of the aqueous ionic domain d_{aq} . Coming from high water content (i.e. large d_{aq}), the uniform decrease of both diffusion coefficients (water and phosphonium) with decreasing water content is expressed with the initial constant diffusion coefficient ratio. The mobility reduction is mostly a long-range percolation effect as a consequence of increased tortuosity affecting both species similarly. The sharper decrease in diffusion coefficient recorded for phosphonium compared to water diffusion at low water content indicates a blocking effect on a local scale. This is clearly visible in the ratio diverging when approaching $d_{\text{aq}} = 0.62$ nm, which is the geometric extension of tetrakis(hydroxymethyl)phosphonium. At the corresponding water content ($\lambda \approx 3$) the diffusion of phosphonium cations comes to a standstill while water (hydronium) still shows reasonable diffusion.

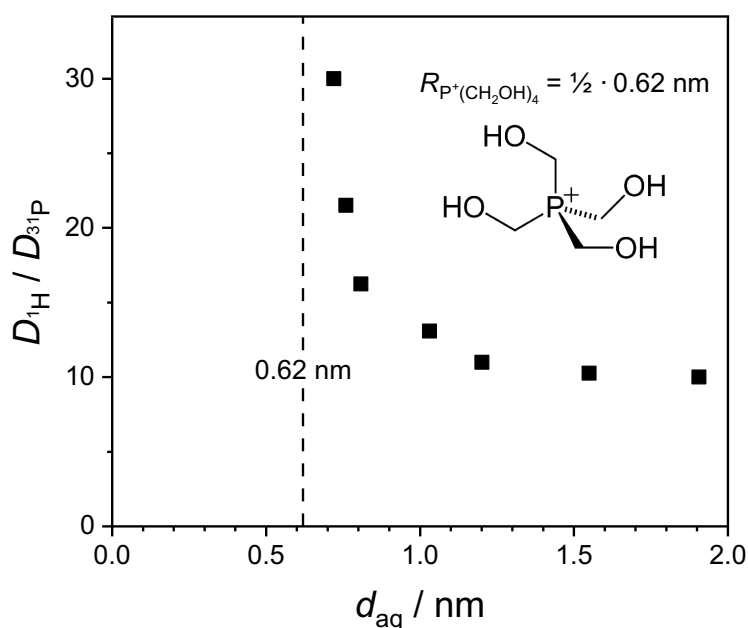


Figure 4.20: Ratio of the diffusion coefficients of water and tetrakis(hydroxymethyl)-phosphonium in Nafion as a function of the width of the aqueous ionic domain d_{aq} . The dashed line marks the diameter of the phosphonium cation.

As it is shown in the following chapters, this size discrimination (sieving) is even more pronounced for ions with a larger size difference and ionomers with better defined morphology.

4.3.3 Ionic transport of VRFB electrolyte in IEMs (VO^{2+} vs. H^+)

Redox flow batteries are among the technologies that provide the potentially lowest cost of stationary electrical energy storage per unit installed capacity [80], because of their potentially long lifetime. As described in chapter 1.1, ion conducting membranes in such batteries have to efficiently separate the electrochemically active ionic species while conducting other ionic species for mediating the electrochemical reactions at a sufficiently high rate. The feasibility of the diverse types of redox-flow batteries therefore highly depends on the availability of separator membranes with high ionic conductivity and appropriate selectivity profile. The latter mainly controls the battery's lifetime, which is still critical for most types of redox-flow batteries [81]. An important exception to this behavior is observed in the vanadium redox flow battery (VRFB).

The reason for this is that both electrolytes of VRFBs contain vanadium ions as redox active species (V^{2+} , V^{3+} in the anolyte and VO^{2+} and VO_2^+ in the catholyte). Hence, any vanadium transport through the membrane reduces the CE, but it does not lead to irreversible mutual chemical contamination of anolyte and catholyte.

Both electrolytes of VRFBs contain their redox active vanadium species dissolved in a 4 M H_2SO_4 solution. As long as predominantly protons and not vanadium species mediate through the CEM separating the electrolytes, the CE is high. Typically, the transport selectivity of vanadium species versus protons, is investigated with vanadyl sulfate ($VOSO_4$) dissolved in sulfuric acid as representative of the VRFB electrolyte.

Interestingly, the vanadium uptake of a Nafion membrane equilibrated with a dilute solution of a model electrolyte (0.05 M $VOSO_4$, 0.05 M H_2SO_4) is hardly detectable. Under these conditions, Donnan exclusion is very effective, and the membrane exchanges only cations (counter-ions) with the solutions. The fact that Nafion remains in its pure proton-form therefore suggests that the VO^{2+} concentration in the electrolyte is very small. Indeed, aqueous solutions of $VOSO_4$ behave as very weak electrolytes [82, 83], and VO^{2+} is mostly present as neutral $VOSO_4$. At higher concentrations as common in VRFBs (e.g. 1.6 M $VOSO_4$ and 4 M H_2SO_4), vanadium species will still enter the membrane.

A common ex-situ method for measuring vanadium crossover is by analytically determining vanadium arriving at a e.g. 1 M $MgSO_4$ / 2 M H_2SO_4 electrolyte separated from a vanadium containing feed electrolyte through the membrane in the absence of any osmotic pressure difference across the membrane [84]. This method yields the ambipolar diffusion coefficient for e.g. VO^{2+}/Mg^{2+} interdiffusion only, and the membrane's water content cannot be controlled during the experiment. Unfortunately, vanadium diffusion coefficients are not accessible by NMR techniques (like phosphonium diffusion in Nafion, see section 4.3.2), but conductivity data bear information about diffusion, since tracer-diffusion and ionic mobility are controlled by the same elementary processes.

Conductivity is easily measured at controlled hydration level, and membranes can be converted into the pure VO^{2+} form (standing for all vanadium containing species).

Although VO^{2+} strongly associates with SO_4^{2-} in aqueous solution, it does not associate with sulfonic acid groups of CEMs. Hence, the total conductivity of CEMs in their VO^{2+} form provides direct information about the molar conductivity Λ_m of dissociated vanadyl species. Figure 4.21 (left) shows $\Lambda_{m;\text{VO}^{2+}}$ as well as the molar conductivity of protons $\Lambda_{m;\text{H}^+}$ for the two types of membrane in their pure VO^{2+} and H^+ forms as a function of water volume fraction Φ_{aq} .

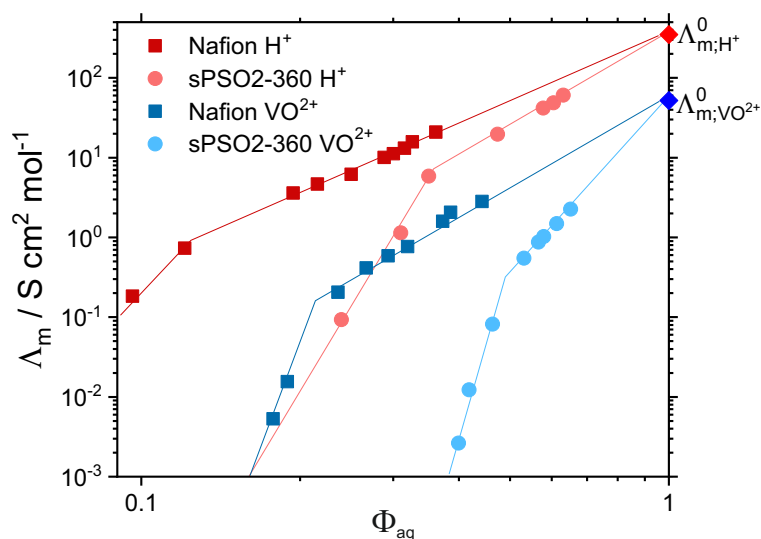


Figure 4.21: H^+ and VO^{2+} molar conductivity Λ_m in Nafion and sPSO2-360 as a function of water volume fraction Φ_{aq} .

The values obtained from extrapolation at $\Phi_{\text{aq}} = 1$ coincide with the molar conductivity of both species in aqueous solution [85]. The data also clearly show that the mobility of both ions is significantly reduced in the less phase-separated hydrocarbon membrane sPSO2-360 ($IEC = 2.78 \text{ meq g}^{-1}$) compared to Nafion ($IEC = 0.91 \text{ meq g}^{-1}$) with well-developed hydrophobic/hydrophilic separation. When plotting the data against λ , the data almost equal at high water contents, but they not only decrease faster for the less phase-separated ionomer once the water content falls below a certain limit (see figure 4.22), the onset of fast decrease is also at higher water contents for the larger species ($\text{VO}_{\text{aq}}^{2+}$) compared to the smaller hydrated proton.

In other words, the ratio $\sigma_{\text{H}^+}/\sigma_{\text{VO}^{2+}}$ (selectivity) starts increasing below this hydration level (Figure 4.22 right), and this behavior can be exploited for suppressing transport of vanadium species while keeping proton conductivity relatively high. For a given

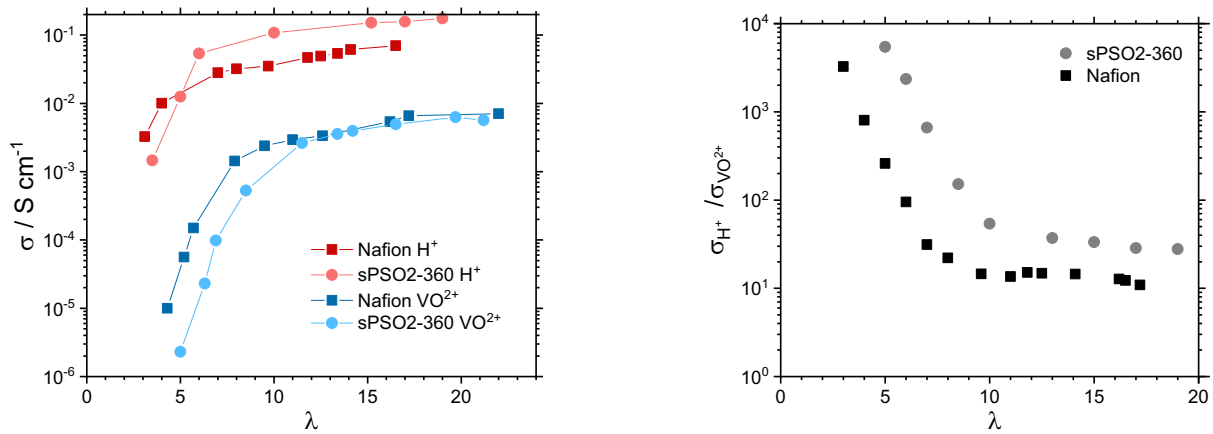


Figure 4.22: Left: H^+ and VO^{2+} conductivity σ in Nafion and sPSO2-360 as a function of hydration number λ . Right: Ratio of H^+ and VO^{2+} conductivities as a function of hydration number λ . Note that the ratio is not calculated from identical samples, but from interpolated data at comparable λ instead.

degree of phase separation, the controlling parameter is the level of hydration, i.e. for less phase separated ionomers higher selectivity is achieved even at higher water content.

Since the hydration level for a given polymer structure strongly depends on IEC, IEC variations is a means to optimizing selectivity. It should also be noted that the onset of the increase in selectivity occurs at a width of the aqueous domain close to the hydrodynamic radius of $\text{VO}_{\text{aq}}^{2+}$. This value of 0.7 nm is consistently obtained from its molar conductivity [85] and from density functional theory calculations, and it is similar for all other vanadium species present in VRFB electrolytes [86–88].

Consequently membranes with a width of the aqueous domain below 0.7 nm at equilibrium with the relevant electrolyte solution should be interesting for VRFBs due to their selectivity for small protons over $\text{VO}_{\text{aq}}^{2+}$.

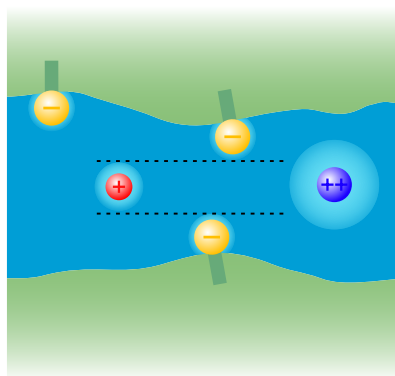


Figure 4.23: Schematic illustration of a morphological bottleneck at the onset of selectivity increase.

4.3.4 Aqueous domain width of membranes in VRFB environment

In the preceding two chapters, the sieving effect in IEMs was visualized by artificially reducing the aqueous domain width by drying the samples. In real applications, the membrane is permanently in contact with electrolyte and equilibrated with its environment to a certain width. For anticipating a membrane's performance in a VRFB, it is necessary to know the aqueous domain width of the membrane in equilibrium with the respective electrolyte. Therefore, SAXS is deployed to measure the correlation length in membrane samples equilibrated in 1.6 M VO_2^+ / 4 M H_2SO_4 , representing the vanadium species containing electrolyte in VRFBs. A PFSA (Nafion) and a hydrocarbon membrane (BP-ArF4) are chosen to be compared as their chemical structure only differs in their backbone (as explained in chapter 4.1.2). Nafion in different ion forms is known to have a large, a pronounced phase separation. On the other hand for BP-ArF4 a typical hydrocarbon morphology (poor hydrophilic / hydrophobic phase separation) is expected, created by the polymer structure of rigid biphenyl backbone (see figure 2.4). In fact, the ionomer peaks of the BP-ArF4 membrane are systematically at higher q values than for Nafion (shown in figure 4.24).

Together with measurements of the water or electrolyte content w_{aq} the aqueous domain width can be calculated with equation (3.16). The measured data is summarized in table 4.4.

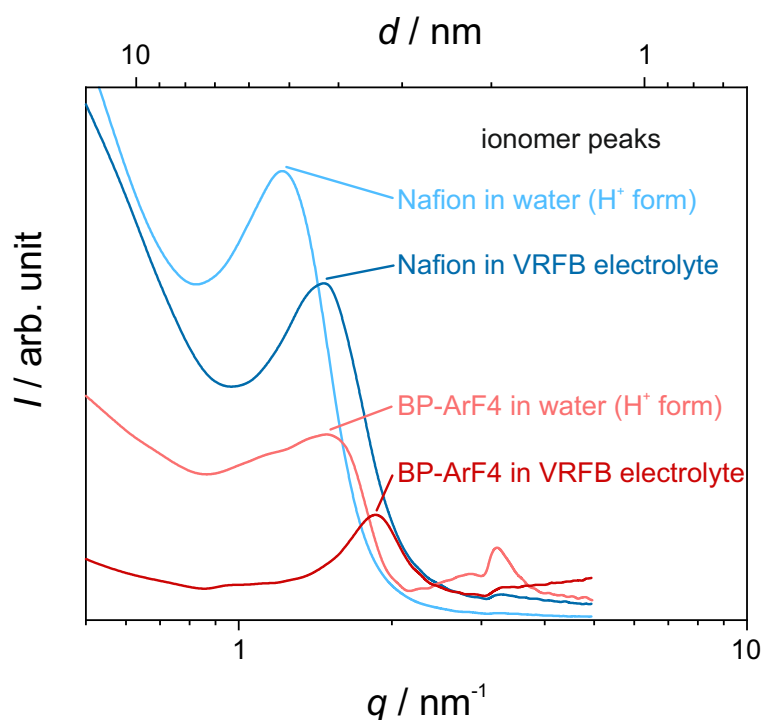


Figure 4.24: SAXS patterns of Nafion and BP-ArF4 in H^+ form in water and in VRFB electrolyte (1.6 M $VOSO_4$ / 4 M H_2SO_4).

Due to the lower water activity in the VRFB electrolyte compared to pure water, the water uptake of both membranes is lower and the aqueous domains narrower. Still, in case of Nafion the aqueous domain width is rather large (1.20 nm) even when equilibrated in 1.6 M $VOSO_4$ / 4 M H_2SO_4 . The aqueous domain width of BP-ArF4 is with its 0.63 nm actually below the hydrodynamic diameter of VO_{aq}^{2+} . The narrow aqueous ionic domains should efficiently block the transport of vanadium species, while still being wide enough for high proton conductivity (provided they are well connected).

Another polymer also has shown vanadyl rejecting properties: the polybenzimidazole PBI-O [89]. The structure is given in figure 4.25.

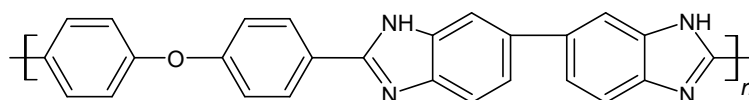


Figure 4.25: Chemical structure of the polybenzimidazole PBI-O.

Table 4.4: Position of ionomer peak in q -space and calculated values for the average width of aqueous ionic domain d_{aq} of membranes in contact with different solutions. Polymer density ρ_{polymer} and mass fraction of aqueous phase w_{aq} is used to calculate d_{aq} .

sample	density	H^+ form in water			in 1.6 M VO_2SO_4 / 4 M H_2SO_4		
	$\rho_{\text{polymer}}/\text{g cm}^{-3}$	q/nm^{-1}	$w_{\text{aq}}/\%$	d_{aq}/nm	q/nm^{-1}	$w_{\text{aq}}/\%$	d_{aq}/nm
Nafion	2.1	1.24	25	2.10	1.49	21	1.20
BP-ArF4	1.4	1.56	28	1.41	1.90	19	0.63

PBI-O is actually not a true ionomer, i.e. it is a neutral polymer, albeit with a high density of weak basic sites ($\text{IEC} \approx 5 \text{ meq g}^{-1}$). In the presence of highly acidic VRFB electrolytes, basic nitrogen sites get protonated, hence the polymer is positively charged keeping anions (here HSO_4^- and SO_4^{2-}) adsorbed. The position of the ionomer peak of a PBI-O sample (figure 4.26) equilibrated in 1.6 M VO_2SO_4 / 4 M H_2SO_4 yields an aqueous domain width of $d_{\text{aq}} = 0.36 \text{ nm}$.

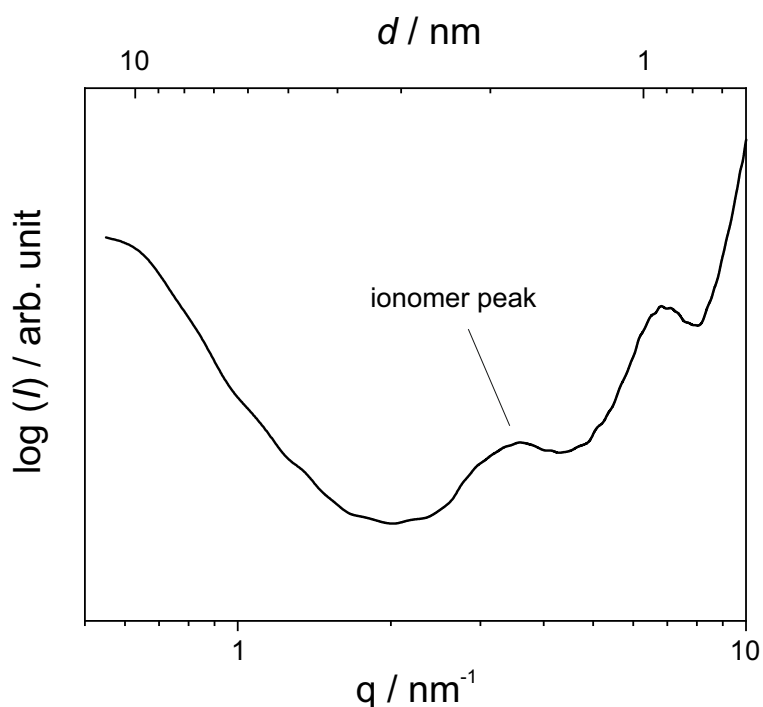


Figure 4.26: SAXS pattern of PBI-O in VRFB electrolyte.

4.3.5 Review of VRFB performances of several membranes

The two important properties of membranes for VRFBs are a high conductivity and an appropriate selectivity profile. The former brings a high voltage efficiency VE and the latter avoids self-discharge, i.e. yields in a high Coulomb efficiency CE. As for several different current values the charge and discharge currents are held constant and the same, the efficiency can be plotted as function of the current density J , which is the charging (or discharging) current divided by the area of the membrane in contact with the solutions. In figure 4.27 both the CE and VE of the membranes Nafion and BP-ArF4 as function of the current density J are compared.

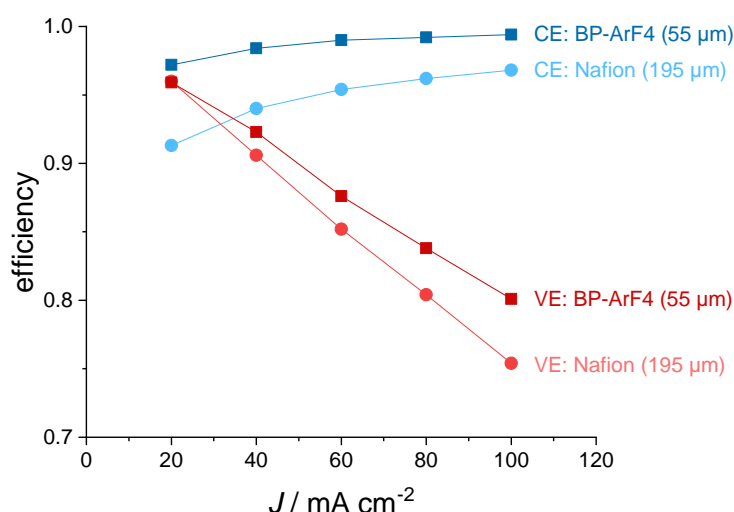


Figure 4.27: Coulomb efficiency (CE) and voltage efficiency (VE) of a VRFB with Nafion and BP-ArF4 as a function of current density J .

Both polymers have a similar volumetric IEC, but the BP-ArF4 membrane is cast thinner (55 μm) as the commercial Nafion membrane (195 μm in the soaked condition). In consequence the area resistance of the BP-ArF4 is lower, i.e. the VE is higher. What strikes one now is that, at the same time, the CE is higher, too. Hence, despite the smaller thickness the crossover of vanadium species is lower for the BP-ArF4 membrane than for the almost 4 times thicker Nafion membrane. In fact, this was already anticipated in the previous chapter, as the aqueous domain width of BP-ArF4 under

VRFB conditions is below 0.7 nm (the approximate hydrodynamic diameter of vanadium species).

Furthermore, sPSO2-360, PBI-O, and Nafion of different thickness were tested in a VRFB. Interestingly, the CE approaches always 100 % for high current densities. Apparently, there is no significant electric field driven transport of ionic vanadium species, i.e. most of the vanadium crossover is occurring through diffusion of neutral vanadium containing species (e.g. VO_2SO_4) entering the membrane as part of excess electrolyte. From the dissociation constant of VO_2SO_4 [85] it is known that the degree of dissociation of a 1.6 M VO_2SO_4 is lower than 5 % and the addition of sulfuric acid is expected to further decrease this number. The observation that Coulomb efficiencies of VRFBs approach 100 % for high current density even highlights that other vanadium species with different oxidation states are similarly forming neutral ion pairs.

The crossover of neutral vanadium containing species can be expressed by a current independent diffusional flux J_D . This constant value is specific for each membrane and can be obtained from the current dependence of the Coulomb efficiency:

$$CE(J) = \frac{J}{J + J_D} \quad (4.16)$$

For membranes of various thickness d , J_D turns out to linearly decrease with increasing membrane thickness d as expected for a pure diffusional flux (respective data is plotted in figure 4.28). This results in the specific diffusional flux j_D as material property:

$$j_D = J_D \cdot d \quad (4.17)$$

VRFBs therefore constitute a special case of a flow battery whose energy efficiency is controlled by the crossover of neutral vanadium species at low current density and by ohmic losses at high current density. Hence, the two intrinsic materials properties describing the membrane behavior in this application are the specific diffusional flux j_D and the specific conductivity σ . While j_D determines the Coulomb efficiency CE, σ determines the voltage efficiency VE according to:

$$VE(J) = 1 - 2 \cdot \frac{J}{OCV \cdot \frac{\sigma}{d}} \quad (4.18)$$

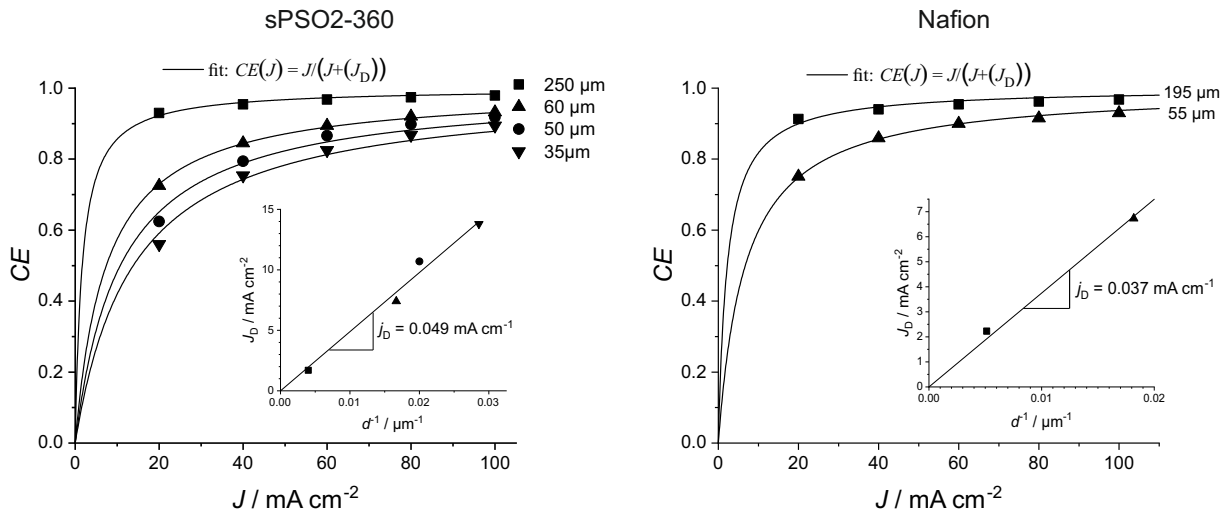


Figure 4.28: Current dependent Coulomb efficiency $CE(J)$ of a VRFB with sPSO2-360 (left) and Nafion (right) membranes of various thickness including fits according to equation (4.16). The insets show J_D as a function of d^{-1} with a slope corresponding to the specific vanadium crossover current density j_D .

where OCV is the open-circuit voltage of the battery. This equation (4.18) is idealized, because the ohmic loss stems from the membrane alone (other resistances of the setup are not included). The overall energy efficiency is calculated as $EE = CE \cdot VE$.

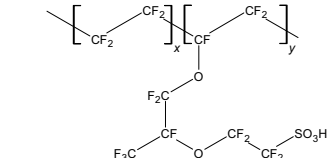
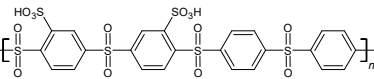
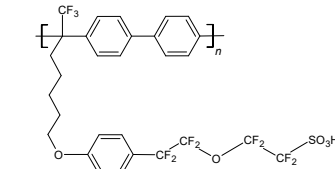
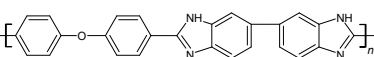
The four different membrane materials, which are measured, are each standing for a certain class of ionomers. Their properties and importance for VRFBs is discussed in the following. Therefore, vanadium crossover j_D and membrane specific conductivity σ were determined in operando with the non membrane contributions of the ohmic resistance subtracted. As a semi-quantitative measure of suitability for VRFBs the figure of merit fom as ratio of conductivity and vanadium crossover is introduced:

$$fom = \frac{\sigma}{j_D} \quad (4.19)$$

The evaluated data is summarized in table 4.5 and the resulting theoretical energy efficiencies for two different membrane thicknesses are plotted in figure 4.29.

Surprisingly, the polybenzimidazole membrane PBI-O has the highest fom (3621), i.e. the best balance of conductivity and vanadium crossover. As PBI-O is actually not a true ionomer, the conductivity then mainly stems from a significant amount (43%) of absorbed excess sulfuric acid with contributions from protons (H_3O^+) and sulfate

Table 4.5: Molecular structure and width of aqueous domain d_{aq} under VRFB conditions of different membrane materials. Specific vanadium crossover current density j_{D} and membrane specific conductivity σ are calculated from VRFB test data. The figure of merit $fom = \frac{\sigma}{j_{\text{D}}}$ is also given.

polymer	$d_{\text{aq}} /$ nm	$j_{\text{D}} /$ $\mu\text{A cm}^{-1}$	$\sigma /$ mS cm^{-1}	$fom /$ V^{-1}
 Nafion	1.2	37	25	655
 sPSO2-360	-	49	62	1258
 BP-ArF4	0.63	5.3	15	2755
 PBI-O	0.36	0.58	2.1	3621

anions. One of the reasons why this conductivity ($\approx 2.1 \text{ mS cm}^{-1}$) remains well below the conductivity of typical ionomer membranes is that the electrolyte is highly dispersed within the polymer corresponding to very narrow electrolyte domains. The clear advantage of this morphology is very low specific vanadium crossover ($j_{\text{D}} = 0.58 \mu\text{A cm}^{-1}$) and presumably low electroosmotic water drag (not measured).

Complementary behavior is observed for a true ionomer with high IEC, sPSO2-360. The high concentration of counter-ions, which are mainly protons in VRFB environment, and high swelling give this membrane the highest conductivity, which is the main reason for its high fom . Compared to PBI-O, its aqueous phase is less dispersed, but compared to Nafion, the hydrophilic/hydrophobic separation of sPSO2-360 is less developed [90] explaining the higher fom of this high IEC hydrocarbon membrane (1258) compared to Nafion (655). Because of its hydrophobic backbone and soft side chain architecture Nafion has the best developed phase separation, and even at low

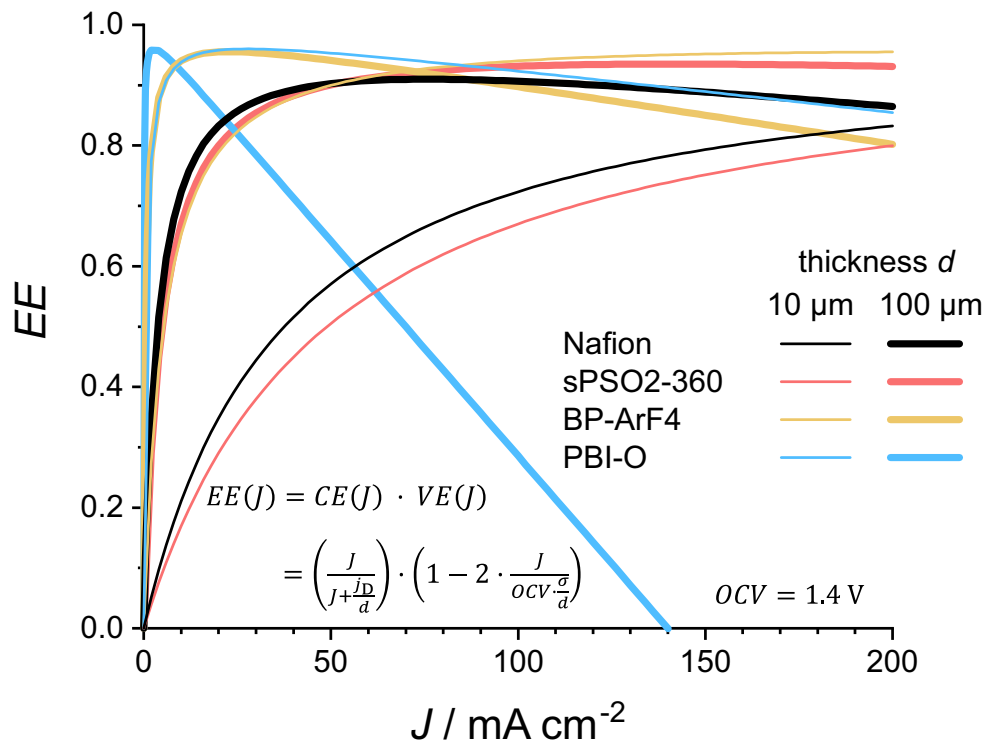


Figure 4.29: Theoretical energy efficiencies of VRFBs with different membranes based on material properties of table 4.5. Since VRFB data were experimentally obtained using membranes of different thickness, energy efficiency values are calculated for two membrane thicknesses d (10 μm and 100 μm) (only losses originating from the membranes included).

electrolyte content (21 %) its aqueous domains are wide enough (1.2 nm) to allow for significant vanadium crossover current $j_D = 37 \mu\text{A cm}^{-1}$.

The first rationally designed ionomer membrane is BP-ArF4. Its relatively rigid hydrocarbon backbone and flexible perfluorinated side chains lead to the development of narrow and well-defined aqueous domains with an average width just below the extension of hydrated vanadium species (0.7 nm). The *fom* of BPArF4 (3621) is actually higher than this of sPSO2-360, but both transport coefficients σ and j_D are about an order of magnitude lower than for sPSO2-360. Therefore, VRFB performance of a BP-ArF4 membrane is similar to the performance of a ten times thicker sPSO2-360 membrane in the covered range of current densities (see calculated energy efficiencies in figure 4.29), and the higher *fom* of BP-ArF4 is reflected in a progressively superior performance for the thin BP-ArF4 membrane for higher current density ($J > 200 \text{ mS cm}^{-2}$). However, j_D and σ do not decrease in the same way when the thickness of the aqueous

domain is reduced. This is clearly evidenced by the very high *fom* of PBI-O and the trends for absolute conductivity and selectivity as a function of hydration (see chapter 4.3.2 and 4.3.3). One may therefore decide for a very thin membrane with highly dispersed electrolyte, but there are surely practical limits to this approach. The highest energy efficiency is expected for a thin 10 μm membrane of PBI-O, indeed (figure 4.29), but only for low current density. For current densities higher than about 100 mA cm^{-1} , the higher conductivity of BP-ArF4 makes this ionomer the preferred membrane material.

As explained above, the choice of a suitable membrane material depends on operating conditions (especially current density) and on how thin membranes can be fabricated. However, there is also room for optimizing membrane materials: an obvious flaw of PBI-O is that no protons are present as counter-ions contributing to conductivity, and for sPSO2-360 swelling is too high for efficiently preventing vanadium crossover. With respective mitigation strategies there is reasonable hope to see membranes with such enhanced functionality soon.

Chapter 5

Summary

In this thesis, selective transport of ionic species (ions and their associates) through membranes in contact with aqueous media is investigated. Experimental results on ion partitioning and mobility are discussed, and the effects of

- valency of ions
- specific interactions between counter-ions and fixed ionic groups (ion association)
- domain width of the aqueous phase

on these properties are separated and quantified.

Cation / anion selectivity is shown to be the consequence of Donnan-exclusion, i.e. co-ion rejection, and the preferred uptake of counter-ions to be of statistical (entropic) reasons. For the same reasons uptake of high valency counter-ions is preferred. For high concentrations of the external solution, i.e. for the case of significant co-ion uptake, the commonly used equations for describing ion partitioning in dilute solution are extended in the present work. This allows for a quantitative prediction of preferred uptake of low valency co-ions, which is experimentally confirmed for the first time.

Effects of specific interactions between counter-ions and the fixed ionic group on selective transport are demonstrated by varying both the kind of fixed ionic groups and counter-ions. The more acidic the fixed ionic group is, the more pronounced is the interaction with soft, polarizable ions like Cs^+ . The observed ion association not only

reduces Donnan-exclusion (because of fixed-charge neutralization), but also leads to preferential uptake of this type of counter-ion compared to others. Consequently, ion immobilization reduces the total conductivity but leaves ionic transference numbers virtually unchanged. NMR relaxation experiments reveal quantitative data on the degree of ion association and the corresponding association constants for different types of ion. These association constants are used to quantitatively calculate ion partitioning in Nafion using simple mass actions laws.

Especially under high ionic strength / low water activity conditions, the most important selectivity mechanism for transport through IEMs is shown to be ion sieving. PFG NMR data disclose that with decreasing hydration level, i.e. with decreasing width of the aqueous ionic domains, the diffusion of ionic species is progressively restricted through steric effects. These effects depend on size of the hydrated species, i.e. the transport of large species may even come to a standstill while smaller species are still reasonably mobile.

With respect to technical applications, vanadium redox flow batteries constitute a special case. It is shown that vanadium crossover is mostly a diffusional process rather than driven by ionic current. The combination of coulombic efficiency data with SAXS measurements on the aqueous domain width unveil a critical width of 0.7 nm (extension of most hydrated vanadium species). As long as this width is not exceeded it ensures low vanadium crossover. High IEC cation exchange membranes with hydrophobic / hydrophilic phase separation on a small scale and low swelling are shown not only to meet such requirement but also to provide high proton conductivity. For high current density applications high conductivity is favorable, while at low current density, the barrier properties of poorly phase separated membranes are demonstrated to be decisive for the performance (energy efficiency).

Bibliography

- [1] Jingyi Luo, Cuiming Wu, Tongwen Xu, and Yonghui Wu. Diffusion dialysis-concept, principle and applications. *Journal of Membrane Science*, 366(1):1–16, 2011.
- [2] Declan A. Doyle, João Morais Cabral, Richard A. Pfuetzner, Anling Kuo, Jacqueline M. Gulbis, Steven L. Cohen, Brian T. Chait, and Roderick MacKinnon. The Structure of the Potassium Channel: Molecular Basis of K⁺ Conduction and Selectivity. *Science*, 280(5360):69–77, 1998.
- [3] Bertil Hille, Clay M. Armstrong, and Roderick MacKinnon. Ion channels: From idea to reality. *Nature Medicine*, 5(10):1105–1109, 1999.
- [4] Giuseppe Zaccai. How Soft Is a Protein? A Protein Dynamics Force Constant Measured by Neutron Scattering. *Science*, 288(5471):1604, 2000.
- [5] Martin Karplus and Gregory A. Petsko. Molecular dynamics simulations in biology. *Nature*, 347(6294):631–639, 1990.
- [6] Yee Ling Lam, Weizhong Zeng, David Bryant Sauer, and Youxing Jiang. The conserved potassium channel filter can have distinct ion binding profiles: structural analysis of rubidium, cesium, and barium binding in NaK2K. *The Journal of general physiology*, 144(2):181–192, 2014.
- [7] T. E. Andreoli, M. Tieffenberg, and D. C. Tosteson. The effect of valinomycin on the ionic permeability of thin lipid membranes. *The Journal of general physiology*, 50(11):2527–2545, 1967.

- [8] G. Eisenman and R. Horn. Ionic selectivity revisited - the role of kinetic and equilibrium process in ion permeation through channels. *Journal of Membrane Biology*, 76(3):197–225, 1983.
- [9] Sally Krasne. *Ion Selectivity in Membrane Permeation*, pages 217–241. Springer US, Boston, MA, 1978.
- [10] R. Margalit and G. Eisenman. Ionic permeation of lipid bilayer-membranes mediated by a neutral, non-cyclic Li⁺ selective carrier having imide and ether ligands. 1. selectivity among mono-valent cations. *Journal of Membrane Biology*, 61(3):209–219, 1981.
- [11] D. Ammann, W. E. Morf, P. Anker, P. C. Meier, E. Pretsch, and W. Simon. *Neutral Carrier Based Ion-Selective Electrodes*, volume 5, pages 3–92. Elsevier, 1983.
- [12] Evan L. Anderson and Philippe Bühlmann. Electrochemical impedance spectroscopy of ion-selective membranes: Artifacts in two-, three-, and four-electrode measurements. *Analytical Chemistry*, 88(19):9738–9745, 2016.
- [13] Derek W. Smith. Ionic hydration enthalpies. *Journal of Chemical Education*, 54(9):540, 1977.
- [14] William M Haynes. *CRC handbook of chemistry and physics*. CRC press, 2014.
- [15] Jack R. Tessman, A. H. Kahn, and William Shockley. Electronic Polarizabilities of Ions in Crystals. *Physical Review*, 92(4):890–895, 1953.
- [16] K. D. Kreuer. On the development of proton conducting polymer membranes for hydrogen and methanol fuel cells. *Journal of Membrane Science*, 185(1):29–39, 2001.
- [17] M. Schuster, K. D. Kreuer, H. T. Andersen, and J. Maier. Sulfonated poly(phenylene sulfone) polymers as hydrolytically and thermooxidatively stable proton conducting ionomers. *Macromolecules*, 40(3):598–607, 2007.
- [18] Michael Schuster, Carla C. de Araujo, Vladimir Atanasov, Henrik T. Andersen, Klaus-Dieter Kreuer, and Joachim Maier. Highly Sulfonated Poly(phenylene sulfone): Preparation and Stability Issues. *Macromolecules*, 42(8):3129–3137, 2009.

- [19] E. O. Stejskal and J. E. Tanner. Spin Diffusion Measurements: Spin Echoes in the Presence of a Time-Dependent Field Gradient. *The journal of chemical physics*, 42(1):288–292, 1965.
- [20] William S Price. Pulsed-field gradient nuclear magnetic resonance as a tool for studying translational diffusion: Part 1. Basic theory. *Concepts in Magnetic Resonance: An Educational Journal*, 9(5):299–336, 1997.
- [21] John E Tanner. Use of the stimulated echo in NMR diffusion studies. *The Journal of Chemical Physics*, 52(5):2523–2526, 1970.
- [22] J. Kärger. Zur Bestimmung der Diffusion in einem Zweibereichsystem mit Hilfe von gepulsten Feldgradienten. *Annalen der Physik*, 479(1-2):1–4, 1969.
- [23] Jan-Patrick Melchior, Günter Majer, and Klaus-Dieter Kreuer. Why do proton conducting polybenzimidazole phosphoric acid membranes perform well in high-temperature PEM fuel cells? *Physical Chemistry Chemical Physics*, 19(1):601–612, 2017.
- [24] Benjamin Chu and Benjamin S Hsiao. Small-angle X-ray scattering of polymers. *Chemical reviews*, 101(6):1727–1762, 2001.
- [25] William Henry Bragg and William Lawrence Bragg. The reflection of X-rays by crystals. *Proceedings of the Royal Society of London. Series A, Containing Papers of a Mathematical and Physical Character*, 88(605):428–438, 1913.
- [26] G Porod, O Glatter, and O Kratky. Small angle X-ray scattering. *by O. Glatter and O. Kratky, Academic Press, London, page 17, 1982.*
- [27] F. G. Donnan. Theorie der Membrangleichgewichte und Membranpotentiale bei Vorhandensein von nicht dialysierenden Elektrolyten. Ein Beitrag zur physikalisch-chemischen Physiologie. *Zeitschrift für Elektrochemie und angewandte physikalische Chemie*, 17(14):572–581, 1911.
- [28] F. G. Donnan and E. A. Guggenheim. Die genaue Thermodynamik der Membrangleichgewichte. *Zeitschrift für Physikalische Chemie*, 162A(1):346–360, 1932.

- [29] F. Helfferich. *Ionenaustauscher: Bd 1: Grundlagen: Struktur, Herstellung, Theorie*. Verlag Chemie GmbH, Weinheim/Bergstr., 1959.
- [30] Torsten Teorell. An Attempt to Formulate a Quantitative Theory of Membrane Permeability. *Proceedings of the Society for Experimental Biology and Medicine*, 33(2):282–285, 1935.
- [31] Kurt H. Meyer and J. F. Sievers. La perméabilité des membranes I. Théorie de la perméabilité ionique. *Helvetica Chimica Acta*, 19(1):649–664, 1936.
- [32] P. Debye and E. Hückel. The theory of the electrolyte II - The border law for electrical conductivity. *Physikalische Zeitschrift*, 24:305–325, 1923.
- [33] Cecil W. Davies. "397. The extent of dissociation of salts in water. Part VIII. An equation for the mean ionic activity coefficient of an electrolyte in water, and a revision of the dissociation constants of some sulphates". *J. Chem. Soc.*, pages 2093–2098, 1938.
- [34] Raymond M. Fuoss. Ionic Association. III. The Equilibrium between Ion Pairs and Free Ions. *Journal of the American Chemical Society*, 80(19):5059–5061, 1958.
- [35] R. H. Stokes and R. A. Robinson. Ionic Hydration and Activity in Electrolyte Solutions. *Journal of the American Chemical Society*, 70(5):1870–1878, 1948.
- [36] T. D. Gierke, G. E. Munn, and F. C. Wilson. The morphology in nafion perfluorinated membrane products, as determined by wide- and small-angle x-ray studies. *Journal of Polymer Science: Polymer Physics Edition*, 19(11):1687–1704, 1981.
- [37] L. Rubatat, G. Gebel, and O. Diat. Fibrillar Structure of Nafion: Matching Fourier and Real Space Studies of Corresponding Films and Solutions. *Macromolecules*, 37(20):7772–7783, 2004.
- [38] Klaus Schmidt-Rohr and Qiang Chen. Parallel cylindrical water nanochannels in nafion fuel-cell membranes. *Nature Materials*, 7(1):75–83, 2008.

- [39] Klaus-Dieter Kreuer and Giuseppe Portale. A critical revision of the nanomorphology of proton conducting ionomers and polyelectrolytes for fuel cell applications. *Advanced Functional Materials*, 23(43):5390–5397, 2013.
- [40] Frances I. Allen, Luis R. Comolli, Ahmet Kusoglu, Miguel A. Modestino, Andrew M. Minor, and Adam Z. Weber. Morphology of Hydrated As-Cast Nafion Revealed through Cryo Electron Tomography. *ACS Macro Letters*, 4(1):1–5, 2015.
- [41] Andreas Münchinger and Klaus-Dieter Kreuer. Selective ion transport through hydrated cation and anion exchange membranes I. The effect of specific interactions. *Journal of Membrane Science*, 592:117372, 2019.
- [42] Gerald S. Manning. Counterion binding in polyelectrolyte theory. *Accounts of Chemical Research*, 12(12):443–449, 1979.
- [43] Soumyadipta Sengupta and Alexey V. Lyulin. Molecular modeling of structure and dynamics of nafion protonation states. *The journal of physical chemistry. B*, 123(31):6882–6891, 2019.
- [44] J. R. Bontha and P. N. Pintauro. Water orientation and ion solvation effects during multicomponent salt partitioning in a Nafion cation-exchange membrane. *Chemical Engineering Science*, 49(23):3835–3851, 1994.
- [45] Yahan Yang and Peter N. Pintauro. Multicomponent space-charge transport model for ion-exchange membranes. *AIChE Journal*, 46(6):1177–1190, 2000.
- [46] T. Okada, N. Arimura, H. Satou, M. Yuasa, and T. Kikuchi. Membrane transport characteristics of binary cation systems with Li⁺ and alkali metal cations in perfluorosulfonated ionomer. *Electrochimica Acta*, 50(16-17):3569–3575, 2005.
- [47] R. A. Komoroski and K. A. Mauritz. A Sodium-23 Nuclear Magnetic Resonance Study of Ionic Mobility and Contact Ion Pairing in a Perfluorosulfonate Ionomer. *Journal of the American Chemical Society*, 100(24):7487–7489, 1978.
- [48] George Eisenman. Cation Selective Glass Electrodes and their Mode of Operation. *Biophysical Journal*, 2(2 Pt 2):259–323, 1962.

- [49] G. Karreman and G. Eisenman. Electrical Potentials and Ionic Fluxes in Ion Exchangers: 1. n Type Non-Ideal Systems with Zero Current. *Bulletin of Mathematical Biophysics*, 24(4):413–427, 1962.
- [50] E. Glueckauf and G. P. Kitt. A Theoretical Treatment of Cation Exchangers. 3. The Hydration of Cations in Polystyrene Sulphonates. *Proceedings of the Royal Society of London Series a-Mathematical and Physical Sciences*, 228(1174):322–341, 1955.
- [51] M. G. Marino, J. P. Melchior, A. Wohlfarth, and K. D. Kreuer. Hydroxide, halide and water transport in a model anion exchange membrane. *Journal of Membrane Science*, 464:61–71, 2014.
- [52] Thomas Dippel and Klaus-Dieter Kreuer. Proton transport mechanism in concentrated aqueous solutions and solid hydrates of acids. *Solid State Ionics*, 46(1):3–9, 1991.
- [53] Thierry Cohen, Philippe Dagard, Jean Molenat, Bernard Brun, and Claude Gavach. Proton leakage through perfluorinated anion exchange membranes. *Journal of Electroanalytical Chemistry and Interfacial Electrochemistry*, 210(2):329–336, 1986.
- [54] Isabelle Tugas, Gerald Pourcelly, and Claude Gavach. Electrotransport of protons and chloride ions in anion exchange membranes for the recovery of acids. Part I. Equilibrium properties. *Journal of Membrane Science*, 85(2):183–194, 1993.
- [55] J. Kamcev, D. R. Paul, and B. D. Freeman. Ion Activity Coefficients in Ion Exchange Polymers: Applicability of Manning’s Counterion Condensation Theory. *Macromolecules*, 48(21):8011–8024, 2015.
- [56] S J Paddison, G Bender, KD Kreuer, N Nicoloso, and TA Zawodzinski. The microwave region of the dielectric spectrum of hydrated Nafion® and other sulfonated membranes. *Journal of New Materials for Electrochemical Systems*, 3(4):291–300, 2000.

- [57] U. Schindewolf and K.-F. Bonhoeffer. Über Ionenaktivitätsbestimmungen mit Hilfe von Ionenaustauschermembranen mit einer Anwendung auf den Dissoziationsgrad von Polyphosphaten. *Zeitschrift für Elektrochemie, Berichte der Bunsengesellschaft für physikalische Chemie*, 57(3):216–221, 1953.
- [58] G. Eisenman, R. Latorre, and C. Miller. Multi-ion conduction and selectivity in the high-conductance Ca^{++} -activated K^+ channel from skeletal muscle. *Biophysical Journal*, 50(6):1025–1034, 1986.
- [59] Nils Wiberg, Arnold F. Holleman, Nils Wiberg, Egon Wiberg, and Gerd Fischer. *Lehrbuch der Anorganischen Chemie*. De Gruyter, Berlin, Boston, 2008.
- [60] Xiao-Yao Nie, Shu-Ying Sun, Ze Sun, Xingfu Song, and Jian-Guo Yu. Ion-fractionation of lithium ions from magnesium ions by electro dialysis using monovalent selective ion-exchange membranes. *Desalination*, 403:128–135, 2017.
- [61] Enver Güler, Willem van Baak, Michel Saakes, and Kitty Nijmeijer. Monovalent-ion-selective membranes for reverse electro dialysis. *Journal of Membrane Science*, 455:254–270, 2014.
- [62] Abreham Tesfaye Besha, Misgina Tilahun Tsehaye, David Aili, Wenjuan Zhang, and Ramato Ashu Tufa. Design of Monovalent Ion Selective Membranes for Reducing the Impacts of Multivalent Ions in Reverse Electro dialysis. *Membranes*, 10(1), 2019.
- [63] Guido Saracco. Transport properties of monovalent-ion-permselective membranes. *Chemical Engineering Science*, 52(17):3019–3031, 1997.
- [64] L. Firdaous, J. -P Malériat, J. -P Schlumpf, and F. Quéméneur. Transfer of Monovalent and Divalent Cations in Salt Solutions by Electro dialysis. *Separation Science and Technology*, 42(5):931–948, 2007.
- [65] Tao Luo, Said Abdu, and Matthias Wessling. Selectivity of Ion Exchange Membranes: A Review. *Journal of Membrane Science*, 555:429–454, 2018.

- [66] H. C. S. Rao and M. M. David. EQUILIBRIUM IN THE SYSTEM $\text{Cu}^{++}\text{-Na}^{+}\text{-DOWEX-50}$. *Aiche Journal*, 3(2):187–190, 1957.
- [67] V. I. Zabolotsky, J. A. Manzanares, V. V. Nikonenko, K. A. Lebedev, and E. G. Lovtsov. Space charge effect on competitive ion transport through ion-exchange membranes. *Desalination*, 147(1):387–392, 2002.
- [68] Younggy Kim, W. Shane Walker, and Desmond F. Lawler. Competitive separation of di- vs. mono-valent cations in electrodialysis: Effects of the boundary layer properties. *Water Research*, 46(7):2042–2056, 2012.
- [69] Tongshuai Wang, Junyoung Han, Kihyun Kim, Andreas Münchinger, Yuechen Gao, Alain Farchi, Yoong-Kee Choe, Klaus-Dieter Kreuer, Chulsung Bae, and Sangil Kim. Suppressing vanadium crossover using sulfonated aromatic ion exchange membranes for high performance flow batteries. *Materials Advances*, 2020.
- [70] Klaus-Dieter Kreuer and Andreas Münchinger. Fast and Selective Ionic Transport: From Ion-Conducting Channels to Ion Exchange Membranes for Flow Batteries. *Annual Review of Materials Research*, 51(1):21–46, 2021.
- [71] Andreas Münchinger, Tongshuai Wang, Torben Saatkamp, Titvinidze Giorgi, Alain Farchi, Sangil Kim, and Klaus-Dieter Kreuer. Selective ion transport through hydrated cation and anion exchange membranes II. The effect of morphology. *Journal of Membrane Science*, in preparation.
- [72] Douglas M. Ruthven. *Diffusion in Molecular Sieves: A Review of Recent Developments*, volume 40 of *ACS Symposium Series*, book section 27, pages 320–334. American Chemical Society, 1977.
- [73] K. D. Kreuer, W. Weppner, and A. Rabenau. Proton conduction in zeolites. *Materials Research Bulletin*, 17(4):501–509, 1982.
- [74] Zhi Xu, Ioannis Michos, Xuerui Wang, Ruidong Yang, Xuehong Gu, and Junhang Dong. A zeolite ion exchange membrane for redox flow batteries. *Chemical Communications*, 50(19):2416–2419, 2014.

- [75] Hongzhang Zhang, Huamin Zhang, Xianfeng Li, Zhensheng Mai, and Jianlu Zhang. Nanofiltration (NF) membranes: the next generation separators for all vanadium redox flow batteries (VRBs)? *Energy Environmental Science*, 4(5):1676–1679, 2011.
- [76] Pengfei Wang, Mao Wang, Feng Liu, Siyuan Ding, Xue Wang, Guanghua Du, Jie Liu, Pavel Apel, Patrick Kluth, Christina Trautmann, and Yugang Wang. Ultra-fast ion sieving using nanoporous polymeric membranes. *Nature Communications*, 9(569), 2018.
- [77] Qing Dai, Zhiqiang Liu, Ling Huang, Chao Wang, Yuyue Zhao, Qiang Fu, Anmin Zheng, Huamin Zhang, and Xianfeng Li. Thin-film composite membrane breaking the trade-off between conductivity and selectivity for a flow battery. *Nature Communications*, 11(13), 2020.
- [78] Soowhan Kim, Jingling Yan, Birgit Schwenzer, Jianlu Zhang, Liyu Li, Jun Liu, Zhenguo Yang, and Michael A. Hickner. Cycling performance and efficiency of sulfonated poly(sulfone) membranes in vanadium redox flow batteries. *Electrochemistry Communications*, 12(11):1650–1653, 2010.
- [79] Klaus-Dieter Kreuer, Stephen J. Paddison, Eckhard Spohr, and Michael Schuster. Transport in Proton Conductors for Fuel-Cell Applications: Simulations, Elementary Reactions, and Phenomenology. *Chemical Reviews*, 104(10):4637–4678, 2004.
- [80] O. Schmidt, A. Hawkes, A. Gambhir, and I. Staffell. The future cost of electrical energy storage based on experience rates. *Nature Energy*, 2(8):17110, 2017.
- [81] Jens Noack, Nataliya Roznyatovskaya, Tatjana Herr, and Peter Fischer. The Chemistry of Redox-Flow Batteries. *Angew. Chem. Int. Ed.*, 54(34):9776–9809, 2015.
- [82] Shu-Di Zhang, Pei-Hua Ma, Yu-Chun Zhai, and Wei-Min Chen. Determination of vanadyl sulfate ion-pair dissociation constant at 298.15 K by Fuoss method. *Rare Metals*, 34(12):873–876, 2015.
- [83] Xiang-Rong Li, Ye Qin, Wei-Guo Xu, Jian-Guo Liu, Jia-Zhen Yang, Qian Xu, and Chuan-Wei Yan. Thermodynamic Investigation of Electrolytes of the Vanadium

- Redox Flow Battery (V): Conductivity and Ionic Dissociation of Vanadyl Sulfate in Aqueous Solution in the 278.15–318.15 K Temperature Range. *Journal of Solution Chemistry*, 45(12):1879–1889, 2016.
- [84] Chenxi Sun, Jian Chen, Huamin Zhang, Xi Han, and Qingtao Luo. Investigations on transfer of water and vanadium ions across Nafion membrane in an operating vanadium redox flow battery. *Journal of Power Sources*, 195(3):890–897, 2010.
- [85] G. Kohler and H. Wendt. Die Bestimmung von Gleichgewichtskonstanten aus kinetischen Messungen. *Berichte Der Bunsen-Gesellschaft Fur Physikalische Chemie*, 70(6):674–681, 1966.
- [86] Fatemeh Sepehr and Stephen J. Paddison. The solvation structure and thermodynamics of aqueous vanadium cations. *Chemical Physics Letters*, 585:53–58, 2013.
- [87] Kevin R. Hinkle, Cynthia J. Jameson, and Sohail Murad. Transport of Vanadium and Oxovanadium Ions Across Zeolite Membranes: A Molecular Dynamics Study. *The Journal of Physical Chemistry C*, 118(41):23803–23810, 2014.
- [88] Zaichun Liu, Ruilian Li, Jizhong Chen, Xiongwei Wu, Kai Zhang, Jun Mo, Xinhai Yuan, Hongmei Jiang, Rudolf Holze, and Yuping Wu. Theoretical Investigation into Suitable Pore Sizes of Membranes for Vanadium Redox Flow Batteries. *ChemElectroChem*, 4(9):2184–2189, 2017.
- [89] Fabio J. Oldenburg, Elisabeth Nilsson, Thomas J. Schmidt, and Lorenz Gubler. Tackling Capacity Fading in Vanadium Redox Flow Batteries with Amphoteric Polybenzimidazole/Nafion Bilayer Membranes. *ChemSusChem*, 12(12):2620–2627, 2019.
- [90] C. C. de Araujo, K. D. Kreuer, M. Schuster, G. Portale, H. Mendil-Jakani, G. Gebel, and J. Maier. Poly(p-phenylene sulfone)s with high ion exchange capacity: ionomers with unique microstructural and transport features. *Physical Chemistry Chemical Physics*, 11(17):3305–3312, 2009.

Appendix A

Experimental details

NMR measurements

PFG NMR measurements were carried out on a Bruker Avance III 400 MHz (9.4 T) spectrometer. It is equipped with a Bruker Diff60 diffusion probe head providing gradients up to 2960 G cm^{-1} in z direction. For each investigated nucleus (^1H , ^7Li , ^{31}P , and ^{133}Cs) a special radiofrequency coil from Bruker was inserted. A stimulated echo pulse sequence with a diffusion time of 20 ms and a sine shaped gradient pulse with effective length of 1 ms was used.

In the case of ionomer solutions, the samples were simply filled into 5 mm NMR glass tubes (Deutero D400) and sealed by melting the open end. Membranes were investigated by being punched into discs of 4 mm diameter and stacked to a total height of around 2 cm in a 5 mm NMR glass tube (inner diameter 4 mm). The tubes are sealed with Teflon plugs minimizing the free volume.

Elemental analysis

Membranes equilibrated in chloride solutions were weighed, dried in a vacuum oven at $T = 120^\circ\text{C}$, weighed again and submerged in 1 M NaNO_3 solution (24 h) for extracting all Cl^- ions. The solution was then titrated with 0.01 M AgNO_3 using an Ag selective electrode (Ag-Titrode, Metrohm AG) attached to the 877 Titrino plus (Metrohm AG).

For the determination of Li^+ , Cs^+ , and Mg^{2+} ions, the equilibrated membranes were soaked in 1 M KCl after being weighed as described above. After dilution and addition of HCl (1 %) the exact amount of the extracted ions was determined by inductively coupled plasma atomic emission spectroscopy (Spectro Ciros CCS, SPECTRO Analytical Instruments GmbH). Dissolved ionomers only needed to be diluted and acidified before being measured by ICP-OES.

Transference experiments

Two compartments filled with electrolyte each with a volume of 330 ml were separated by a membrane with an area of 6 cm^2 . Constant current (100 mA cm^{-2}) was applied for 90 min and the composition of both electrolytes was analyzed every 30 min (3 times), and transference numbers were calculated from the compositional changes. For the Li^+/Cs^+ transference experiment, a 1 M mixture of LiCl and CsCl of the ratio 1:1 was used at the anode side with graphite as an electrode material. The cathode compartment with a nickel cathode was filled with 0.1 M solution of the same LiCl/CsCl ratio (1:1). A CEM were used as a separator. Electrolyte compositions were measured by elemental analysis (ICP-OES) of small samples (0.5 mL each). The compositional changes were linear with time indicating that the chosen current was below the limiting current of the device. The concentration change of the electrolyte in both compartments was of the order of 0.1 M at the end of the experiment.

For the H^+/Cl^- transference experiment of an anion exchange membrane (fumasep FAA-3), the anode side with a graphite electrode contained a 1 M HCl solution and the other compartment a copper cathode in a 0.5 M CuCl_2 solution ($pH = 3.3$). The

proton concentration on the cathode side was determined by measuring the pH value directly within the electrolyte during brief (about 1 min) interrupts (at a current of 0.6 A (100 mA cm^{-2})), the pH dropped linearly to a value of 1.0 after 90 min. The background flux of protons (coupled diffusion with Cl^- and Cu^{2+}) was determined in the same way under OCV (open circuit potential) condition and found to be about 24 % of the total proton flux. The ratio of the potential driven proton flux and the applied current then is the proton transference number t_{H^+} .

SAXS

The SAXS measurements were carried out using using a rotating anode (Bruker FR591-Nonius) operating at 3 kW with a source of Cu-K α radiation ($\lambda = 1.5418 \text{ \AA}$). The x-ray optics consists of a set of two horizontal and vertical 16 cm long Ni-filtered total reflection mirrors (Kirkpatrick-Baez mirrors) positioned at 180 cm from the x-ray source. The beam line is equipped with a set of 4 beam defining slits (close to mirror optics) and a set of 4 anti-scattering slits in front of the sample position (Xenocs motorized non-scattering slits). Scattering patterns were recorded using a two-dimensional $14 \text{ cm} \times 14 \text{ cm}$ area (Bruker VANTEC-2000) mikrogap detector. The sample detector distance was placed at 1 m and 3.5 m to explore q values from about 0.01 \AA^{-1} up to 0.4 \AA^{-1} . The sample-detector distance was calibrated using silver behenate as the standard.

After equilibration in pure water or in a 1.6 M VO_2SO_4 / 4 M H_2SO_4 aqueous solution respectively, between two and four membrane samples (discs of 4 mm diameter with total thickness around 300 μm) were placed in a brass cell between 5 μm thick Mylar sheets serving as windows. The mass difference of the membranes in the dry proton and the soaked state was attributed to electrolyte uptake. For calculating the volume fraction of vanadium electrolyte in the membrane, its density was taken to be identical to that of the 1.6 M VO_2SO_4 / 4 M H_2SO_4 aqueous solution (1.4 g cm^{-3}).

VRFB tests

The VRFB single cell tests were recorded by Tongshuai Wang at the University of Illinois in the department of chemical engineering led by Prof. Sangil Kim.

Two graphite felts (MTI, 30 mm × 30 mm × 4 mm) were used as electrodes. The testing membrane had an active area of 9 cm². The total vanadium concentration was 1.6 M (V²⁺, V³⁺ as anolyte and respectively VO²⁺, VO₂⁺ as catholyte) dissolved in 4 M sulfuric acid. The electrolytes were circulated by peristaltic pumps with a flow rate of 60 mL min⁻¹. The cell operation was controlled by a Landt battery testing system (CT2001A-5V1.8A, 8 Channels) with cut-off voltages of 1.65 V (charge process) and 0.8 V (discharge process).